# THERMODYNAMIC AND STRUCTURAL ASPECTS OF

# EQUILIBRIUM AND MECHANICALLY MILLED

# YBa2Cu3O6+δ POWDER

Thesis by

David Soong-hua Lee

In Partial Fulfillment of the Requirements

for the Degree of Doctor of Philosophy

California Institute of Technology

Pasadena, California

1993

(submitted November 19th, 1992)

*to my parents*

# ACKNOWLEDGEMENTS

*What you are saying is what a man of the world said to Abbé LeBlanc.*
*The Abbé had said:*
    *"The Marquise de Pompadour picks me up in her hand and carries me to the very doorstep of the*
    *Academy, and then takes her hand away and I fall down and break both my legs."*
*The man of the world replied:*
    *"Well, Abbé, you must get up and batter the door in with your head."*
*The Abbé answered:*
    *"That's what I tried to do, and do you know what I got? A bump on the forehead."*
<div align="right">Le Neveu de Rameau, D. Diderot</div>

    I would first like to thank my advisor, Bill Johnson, who is unique among all professors I have met in his ability to run a large and productive research effort without ever losing sight of the human side of the advisor-student relationship. He cares about his students as people and not only lends us an ear in times of need, but has even shown us his own humanity. He is happily more than my thesis advisor: he is a friend. I thank him for this, and for his guidance and encouragement over the years. I also thank him for teaching me how to win at blackjack by counting cards.

    Carol Garland and Concetto Geremiah (r.i.p.) are two of the kindest people I have ever met. Carol knows that I am far more grateful to her for all the help and advice over the past six years than a few brief lines in an "Acknowledgements" section could ever convey. Her expertise in all things related to electron microscopy and sample preparation are unequalled. But just as important to me have been her kindness and patience and willingness to talk and listen to a person who is frustrated or angry or happy or bored. Concetto, you are missed to this day.

    Thanks to my officemate Dr. Hao Ouyang, with whom I have had a continuous "cultural exchange" for the past four years: he would take Doug and I to the newest inexpensive Chinese food hangout in Monterey Park and we would give him lessons in

American slang. Dr. Doug Pearson, our other officemate for most of the time, is my closest friend and fishing buddy.

The term "fishing buddy" has a special connotation and I would like to acknowledge my other fishing buddies: Hal Ginder, Andy Mutz, Tom Perry and Thad Vreeland. The hours spent flyfishing with them have played almost as important a role in the successful completion of this dissertation as time spent in lab. Time spent on the water with them was certainly a non-negligible percentage of the past four summers. We are all "haunted by waters." Hal, one of the few people in the category "honest fisherman," loves to be out on the water fishing. Tom, who can actually think like a trout (some would say that is the *best* he can do), is simply the finest fisherman I have ever met. If Thad could rearrange the way things are, all trout would probably be gulpers on Hebgen Lake. And Andy may not be the best fisherman, but he *is* undoubtedly the worst whitewater canoer. My fondest memories of the graduate school years will be the weeks spent flyfishing Montana trout streams with one or more of them while staying at the home of our gracious hosts, Thad and Mary Vreeland. I know that in the years to come, we will have many more chances to exaggerate the size and number of fish we caught and have Mary fry a few of them up in one of her spectacular meals.

I will also remember fondly the times spent in the High Sierras with Andy and/or others, carrying heavy backpacks (with 20 lbs. of beer) deep into the backcountry to catch Golden Trout. Actually, many of the trips with Andy were not particularly pleasant – I guess these have to be called "learning experiences" rather than "fond memories." Watching Andy try and fail to cross the Kern River at the height of Spring runoff (the water was 40° F.) in only his underwear and a 60 lb. pack on his back – that is a fond memory.

In six years I have had the time to make many close friendships outside of the lab. The encouragement, understanding and support given to me has been tremendous. I want to thank Marcia Hudson, Jennifer & Racquel Buffalo, Linda Dosza, Illiana Salazar, Joe &

Mary Kay Holzer, Joey Jr., Channing Ahn, Lee Burrows, Ingrid Choong, Teresa Englehard, Mike Pottinger and Tab & Keri Stephens for their friendship and everything they have done. I would also thank friends and coworkers that were or are now in the Materials Science/Applied Physics departments: Pam Albertson, Phil-shil Askenazy, Zezhong Fu, Egon Hellstern, Jorge Kittl, Chuck Krill, Simon Nieh, Necia Parr, Konrad Samwer and the rest of the Keck Materials group.

I also want to acknowledge my friends and mentors from back home in Williamsville, New York. If it weren't for their wisdom, encouragement, understanding and foresight, I could never have come to this point. Mrs. Kordinak, Mr. & Mrs. Richman, and Mr. & Mrs. Snyder - thank you. With each year that goes by, I realize more just how important those early years were and how special the people and circumstances of my childhood were. David, Eddie and Renée, thank you for everything.

> *You must know that there is nothing higher and stronger and more wholesome and good for life in the future than some good memory, especially a memory of childhood, of home. People talk to you a great deal about your education, but some good, sacred memory, preserved from childhood, is perhaps the best education.*
> <u>The Brothers Karamazov</u>, F. Dostoyevsky

Thank you Aunt Jane and Uncle Frede for the support you have given both to me and my mother.

Mom, Dad and Kelvin — *thank you most of all.*
Before, during and after everything else, I love you.

# ABSTRACT

The equilibrium relationships between partial pressure of oxygen, temperature, lattice parameters and oxygen content in the $YBa_2Cu_3O_{6+\delta}$ superconductor were examined by differential scanning calorimetry, high-temperature x-ray diffraction, thermogravimetric analysis and measurement of pressure versus concentration isotherms. Oxygen pressures ranged from 1 mbar to 1013 mbar and temperatures ranged from 400°C to 750°C. Lattice parameters as a function of temperature and partial pressure of oxygen were measured. P(c) isotherms and TGA were used to measure oxygen content as a function of temperature. A phase line separating the low temperature orthorhombic phase and the high temperature tetragonal phase was determined. No evidence of a miscibility gap between the two phases was found in the range of temperatures and oxygen pressures explored. From the data, the excess enthalpy and entropy through the orthorhombic to tetragonal phase transition was calculated. It was found that the excess entropy is less than the entropy of mixing for an ideal solution. DSC was used to measure enthalpies for the transition and to calculate activation energies for the process. The enthalpy for the evolution of oxygen from the solid was found to be 5.2 kJ/mol in Argon, 2.0 kJ/mol in 16% oxygen and 1.7 kJ/mol in pure oxygen. Activation energies for the transition were 1.2 eV/atom in Argon, 1.8 eV/atom in 16% oxygen, and 2.9 eV/atom in 100% oxygen. DSC using a sealed sample pan (to maintain a constant concentration of oxygen in the solid during heating) was done and no signal arising from the order–disorder transition was seen.

High temperature x-ray diffraction and differential scanning calorimetry were used to study the effect of high energy mechanical deformation on the structural and thermal characteristics of $YBa_2Cu_3O_{6+\delta}$ powder. A Warren-Auerbach analysis was done on the x-ray peaks to determine the grain size of the material as a function of milling time. A

Phillips 430 transmission electron microscope equipped with an EDX detector was used to determine chemical composition and grain size of the ball-milled material.

Broadening of Bragg peaks due to the reduction of grain size makes the distinction between orthorhombic and tetragonal phases of $YBa_2Cu_3O_{6+\delta}$ difficult after only one hour of ball milling. The equilibrium orthorhombic to tetragonal phase transition may occur within the first hour of ball-milling. Longer milling times (>5hrs) produce a cationic disorder on the yttrium and barium sites. A metastable cubic $(Y_{1/3}Ba_{2/3})CuO_{2+\delta}$ structure with a= 3.86Å is formed. Further mechanical deformation does not induce the formation of an amorphous phase; rather, an eventual decomposition into the constituent oxides $Y_2O_3$ and $BaCuO_2$ is observed. Annealing of the metastable cubic $(Y_{1/3}Ba_{2/3})CuO_{2+\delta}$ phase in relatively low pressures of oxygen (≥100mbar) and at moderate temperatures (~400–600°C) produces an as yet unidentified cubic phase which is unstable in air and has a lattice constant of a= 5.47Å.

# TABLE OF CONTENTS

# LIST OF FIGURES

José Arcadio Buendía, without understanding, stretched out his hand toward the cake, but the giant moved it away. "Five reales more to touch it," he said. José Arcadio Buendía paid them and put his hand on the ice and held it there for several minutes as his heart filled with fear and jubilation at the contact with mystery. Without knowing what to say, he paid ten reales more so that his sons could have that prodigious experience. Little José Arcadio refused to touch it. Aureliano, on the other hand, took a step forward and put his hand on it, withdrawing it immediately. "It's boiling," he exclaimed, startled. But his father paid no attention to him. Intoxicated by the evidence of the miracle, he forgot at that moment about the frustration of his delirious undertakings... He paid another five reales and with his hand on the cake, as if giving testimony on the holy scriptures, he exclaimed:
  "This is the great invention of our time."

               *One Hundred Years of Solitude*, Gabriel García Márquez

# I. Introduction to High Temperature Superconductivity

High temperature superconductors were almost literally an overnight sensation. The violent manner with which the members of the scientific community dropped whatever projects they had been working on and turned their attention to this new class of materials is without precedent in the history of science. Many fascinating accounts of the early days of the field and its subsequent maturation into a more stable and accepted area of research have been written.[1] The field has calmed down quite a bit since its "Woodstock-like" inception at the March meeting of the American Physical Society in New York City in 1987 (to quote the New York Times), but it remains unique in many ways: there is the obvious fact that no other materials superconduct at such high temperatures.[2] Also unique is the diversity of research backgrounds all brought together to work on one problem. After the initial confusion over terminology was resolved, the researchers could each attack the problem from their own angle. This undoubtedly quickened the pace of discovery and understanding. In just five years, a tremendous amount of information has been catalogued. Yet even with the unbelievable global effort put forth, the burning questions still remain: what is the mechanism for Cooper pairing in

these materials and how high can the transition temperature be raised? Work continues on these questions.

As researchers in the field raced to find clues to take them to the next level of comprehension, they inevitably left gaps in the information database of the materials. Widespread technological application requires first a basic understanding of the nature of the material; and any material with the ability to superconduct well above the boiling point of nitrogen will undoubtedly have some applications. An interesting story along these lines was told by the group at IBM in Almaden, California. They were racing to be the first to duplicate the results of Wu et al.[3] at Alabama (this was the group that first discovered superconductivity above 77K). In their haste they inadvertently left a sample in a furnace that had been shut off. The other samples were pulled from the hot oven and tossed around in the air to cool more quickly. These samples showed no signs of superconductivity even though they had followed the ratios used in the Alabama group's recipe. The next morning, the orphaned sample was discovered in the cool oven and taken out for measurement. Voilà, a 92K superconductor.

The key was the slow cooling down period. In the group's rush to be the first to be the second, that important fact was missed (in one more day, the Almaden group had isolated and solved the crystal structure of the $YBa_2Cu_3O_{6+\delta}$ phase. A flight was booked to hand deliver a manuscript to the offices of Physical Review Letters. They were beaten by three hours by a group from Bell Labs. While at the offices of the journal, the group from IBM Yorktown Heights hand delivered their manuscript).

As the sample cooled down in the furnace, it absorbed oxygen. It is this absorption of oxygen in the compound, and its profound effect on both the structural and thermodynamic quantities of $YBa_2Cu_3O_{6+\delta}$ that is the subject of the first part of this thesis.

The second part of this thesis deals with the effect of mechanical milling on the structure and thermodynamic properties of this fascinating material.

## I.A.1.    The Crystal Structure of $YBa_2Cu_3O_{6+\delta}$

An interesting aspect of the $YBa_2Cu_3O_{6+\delta}$ superconductor is the extreme ease with which oxygen incorporates reversibly into the material when in equilibrium with a partial pressure of oxygen gas.[4] In the temperature range of 450°C to 750°C, $YBa_2Cu_3O_{6+\delta}$ may very well be the most sensitive oxygen sensor yet discovered.[5] In its oxygen deficient state, with $\delta \approx 0$, the crystal structure of $YBa_2Cu_3O_{6+\delta}$ is tetragonal (P4/mmm), with lattice constants a=3.8570(1)Å and c=11.6762(3)Å, as measured by neutron diffraction experiments by Jorgensen et al., 1987.[6] When fully oxygenated, $\delta \approx 1$ and the structure is orthorhombic (Pmmm) with lattice constants a=3.8198(1)Å, b=3.88498(1)Å and c=11.8194(3)Å.[7]

These structures are shown in figures 1.1a and 1.1b and can best be described as tripled perovskites: the perovskite unit cell has the formula $ABX_3$ and is a cubic unit cell which contains an A atom at the center of the cube, B atoms at the corners and X atoms at the center of the cell edges, where X is most commonly an oxygen or flourine atom. In the $YBa_2Cu_3O_{6+\delta}$ superconductor, the center perovskite cell has yttrium as its body-centered atom (the A atom) and the upper and lower perovskites have barium as their body-centered atoms. The cells are then stacked along the c-axis with the oxygen atoms corresponding to the X's in the perovskite formula and copper atoms to the B's. Finally, the oxygen atoms situated along the a-axis cell edge are removed. In the tetragonal phase, the oxygen atoms situated along the b-axis cell edge are also removed. Note that there are five distinct oxygen sites [O(1) through O(5)] in the orthorhombic unit cell.

The ordered oxygen vacancies that are found in these structures result in a reduction in the coordination numbers of the copper atoms from the ideal six-fold octahedral coordination. In the orthorhombic cell of $YBa_2Cu_3O_7$, there are two four-foldcoordinated copper atoms (Cu(1) sites) and two five-fold coordinated copper atoms (Cu(2) sites). This compound can best be thought of as being comprised of chains and

O-1
O-2
Cu-1

Cu-2
Y

O-3

Ba

O-4

O-5
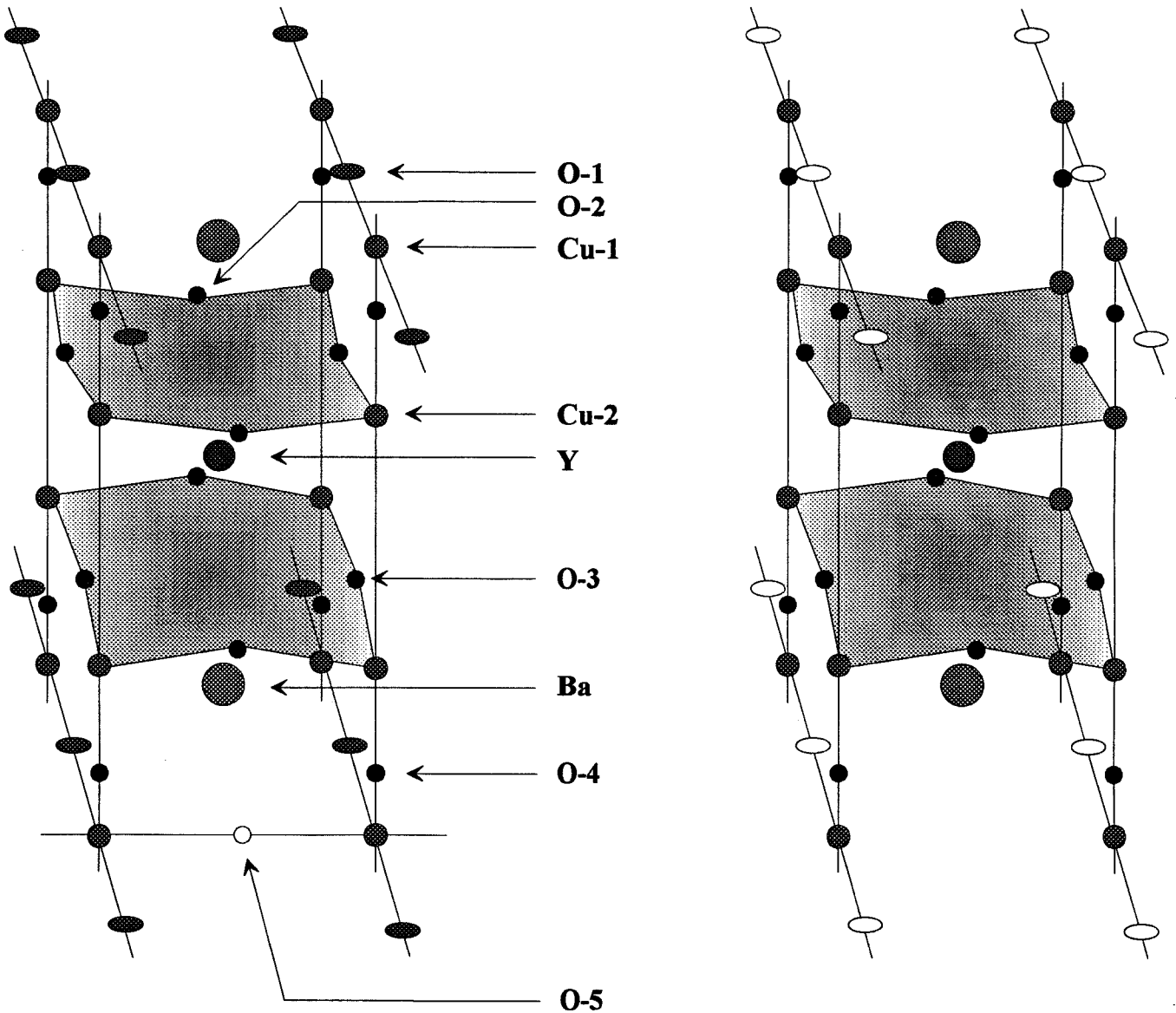
Figure 1.1– (a) The orthorhombic phase, in which the O(1) sites are filled with oxygen atoms. This corresponds to a formula unit of $YBa_2Cu_3O_7$. (b) The tetragonal phase, in which the O(1) sites are not filled. This corresponds to a formula unit of $YBa_2Cu_3O_6$. Note that the O(5) sites referred to in the text are between Cu(1) sites.

layers. The Cu(1) atoms form linear chains of corner shared planes oriented along the b-axis and the Cu(2) atoms form two-dimensional layers of corner-shared square pyramids. The O(1) atom in the chain also serves as the apical oxygen atom for the square pyramidal Cu(2). This is shown in figure 1.2.

In the tetragonal cell of $YBa_2Cu_3O_6$, removal of the O(1) atoms results in a change in coordination number for the Cu(1). The five-fold coordination of the Cu(2) atoms is maintained. However, since the Cu(1)-O(1) distance decreases and the Cu(2)-O(1) distance increases, the Cu(2) atoms are made more square-planar. A more detailed discussion of the various relationships between bond lengths and oxygen content is discussed by Murphy et al.[8]

**Cu-O Planes**

**Cu-O Chains**
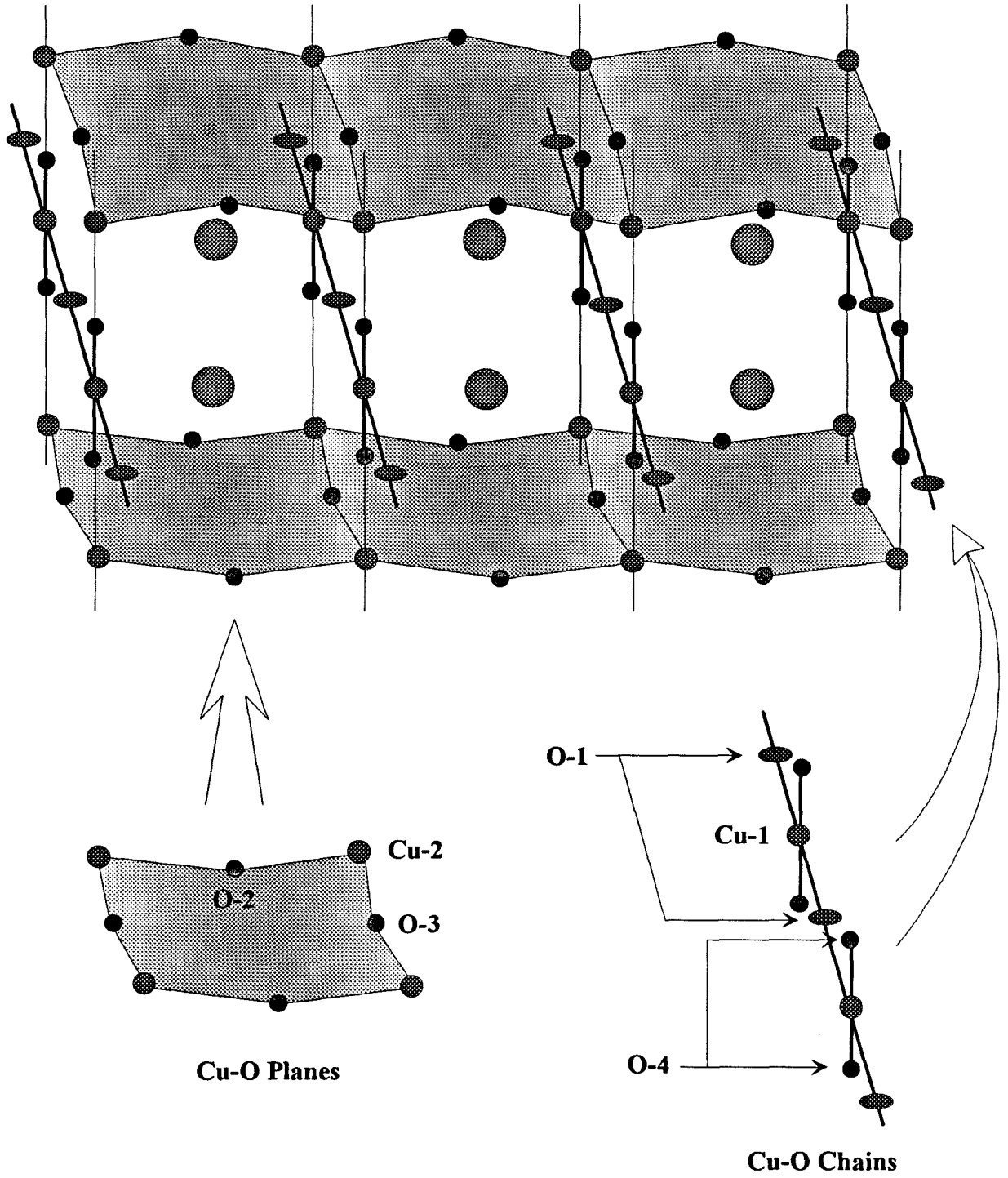
Figure 1.2– The arrangement of Cu and O atoms in their planes and chains.

### I.A.2.    Correlation Between Crystal Structure and Physical Properties

The phase transition from orthorhombic to tetragonal symmetry (from an oxygen content of approximately seven atoms per unit cell to approximately six) is of concern because of its effect on the superconducting properties of the material.

In its fully oxygenated state, just above the superconducting transition temperature, $T_C$, $YBa_2Cu_3O_7$ has a metallic normal state resistivity in the $CuO_2$ planes of $\rho_{ab} \approx 100\text{-}200\mu\Omega\cdot cm$,[9] and a resistivity perpendicular to the $CuO_2$ planes of $\rho_\perp \approx 500\mu\Omega\cdot cm$;[10] in its fully reduced state, $YBa_2Cu_3O_6$ does not superconduct at all and displays normal state resistivity similar to that of a semiconductor.[11] Moreover, as the oxygen content of the material changes continuously from $O_6$ to $O_7$, the superconducting transition temperature changes.

Initially, it was unclear as to whether or not the transition temperature changed continuously or in a stepwise manner as a function of oxygen content. Figure 1.3, adopted from Greene and Bagwell,[12] shows how $T_C$ varies with oxygen content. The trend is clear: the transition temperature increases as one heads toward larger values of $\delta$. The width of the plateau centered around $\delta \approx 0.5$ depends on the annealing treatment given to the sample and is very sensitive to sample inhomogeneities.[13] For example, in the figure, the plateau seems much more pronounced for those samples whose oxygen content was controlled by a low-temperature gettering technique than for those whose oxygen content was controlled by quenching from high temperatures. The explanation is that the gettering technique allows more time for oxygen to settle into its preferred configuration. Typically the gettering experiments hold their temperatures for tens of hours whereas thequench times are on the order of tenths of seconds. The AC susceptibility data shown

# $T_c$ versus Oxygen Concentration
## in $YBa_2Cu_3O_{6+\delta}$
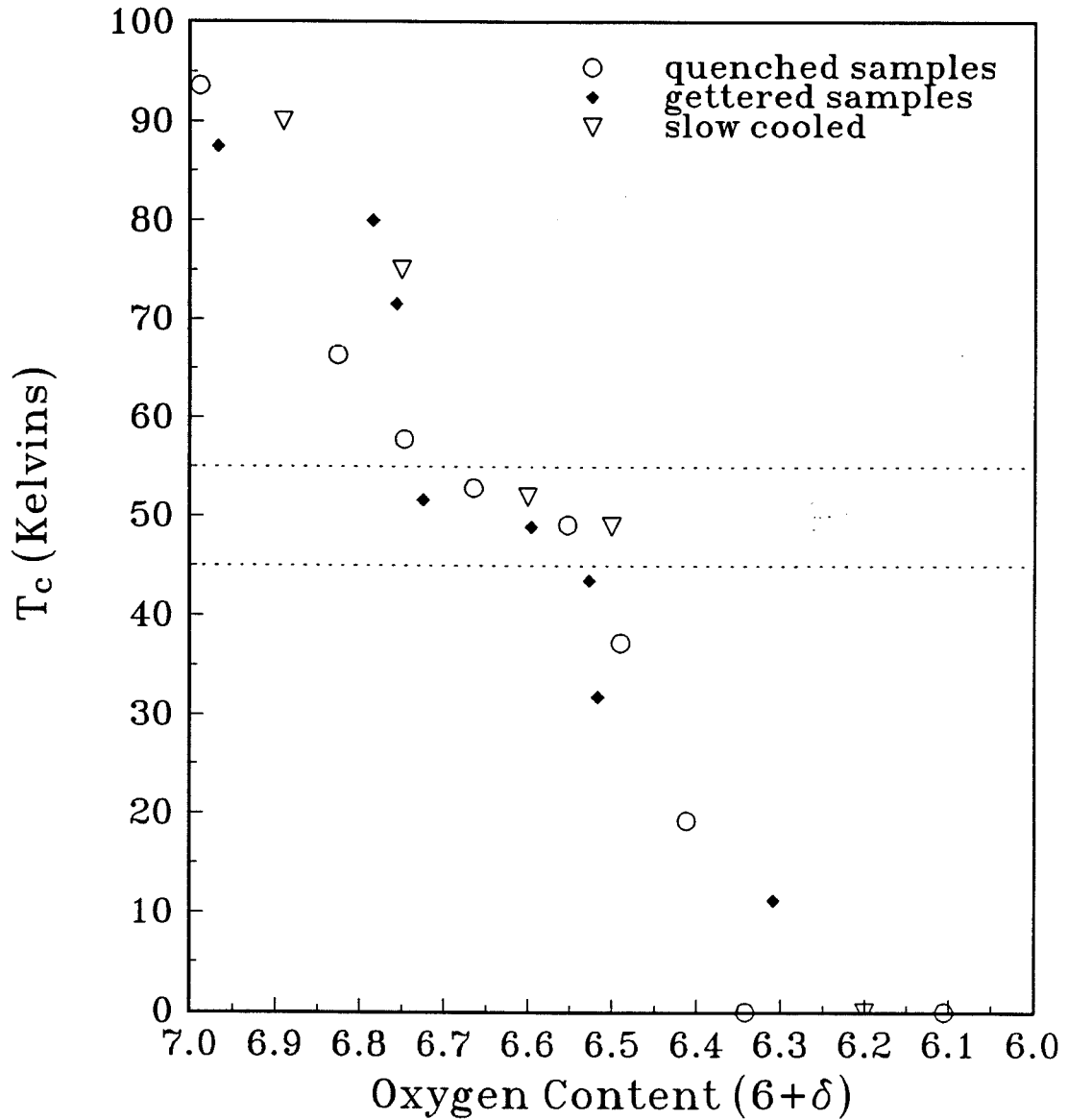


Figure 1.3– Superconducting transition temperature versus oxygen concentration in $YBa_2Cu_3O_{6+\delta}$. Note the plateau centered around $O_{6.6}$ (adopted from Greene and Bagwell).

in figure 1.4 illustrates the differences in the fraction of superconducting material that result from the two different techniques. In the figure, the susceptibility of the sample that was annealed at 300°C in Argon for a long period of time produces a 55K superconductor with an oxygen content of about $\delta \approx 0.5$ (although a small percentage still undergoes a 90K transition) whereas the sample quenched from high temperature still shows a superconducting transition at around 90K in addition to a secondary transition at around 55K. A sample with a clean superconducting transition at 90K is shown for reference. Models of the ordering could not at first successfully reproduce this 55K superconductor, but once additional, longer range interactions were included, this phase could be predicted by computer models.[14,15]

There is a precise correlation between the Cu(1)–O(4) bond length and $T_C$. The O(4) bridging oxygen is located between the Cu(1) and Cu(2) sites and lies in the BaO plane in $YBa_2Cu_3O_{6+\delta}$. Below a bond length of 1.82Å, the compound does not superconduct. At $T_C = 90K$, the bond length is 1.92Å. As oxygen is removed from the compound, the O(4) atom moves toward the $CuO_2$ planes, and there is an accompanying depression in $T_C$. This correlation, shown in figure 1.5, holds independent of whether the oxygen content of the pure $YBa_2Cu_3O_{6+\delta}$ compound is reduced or the material is doped with Co or Al, both of which substitute for Cu in the compound. The inset in figure 1.5 shows schematically the structural changes that occur as superconductivity is destroyed by doping the CuO chains through either oxygen removal or Cu replacement. It is believed that charge transfer between the Cu(1)–O chains and the CuO planes is reduced because of the greater distance between them and the greater Ba–O(4) distance. It is likely that as the Ba cation moves closer to the $CuO_2$ planes, there is an increased charge transfer between these elements, resulting in the removal of holes from the conducting CuO planes. XANES measurements have confirmed that removal of O(1)

# AC Susceptibility of YBa$_2$Cu$_3$O$_{6+\delta}$
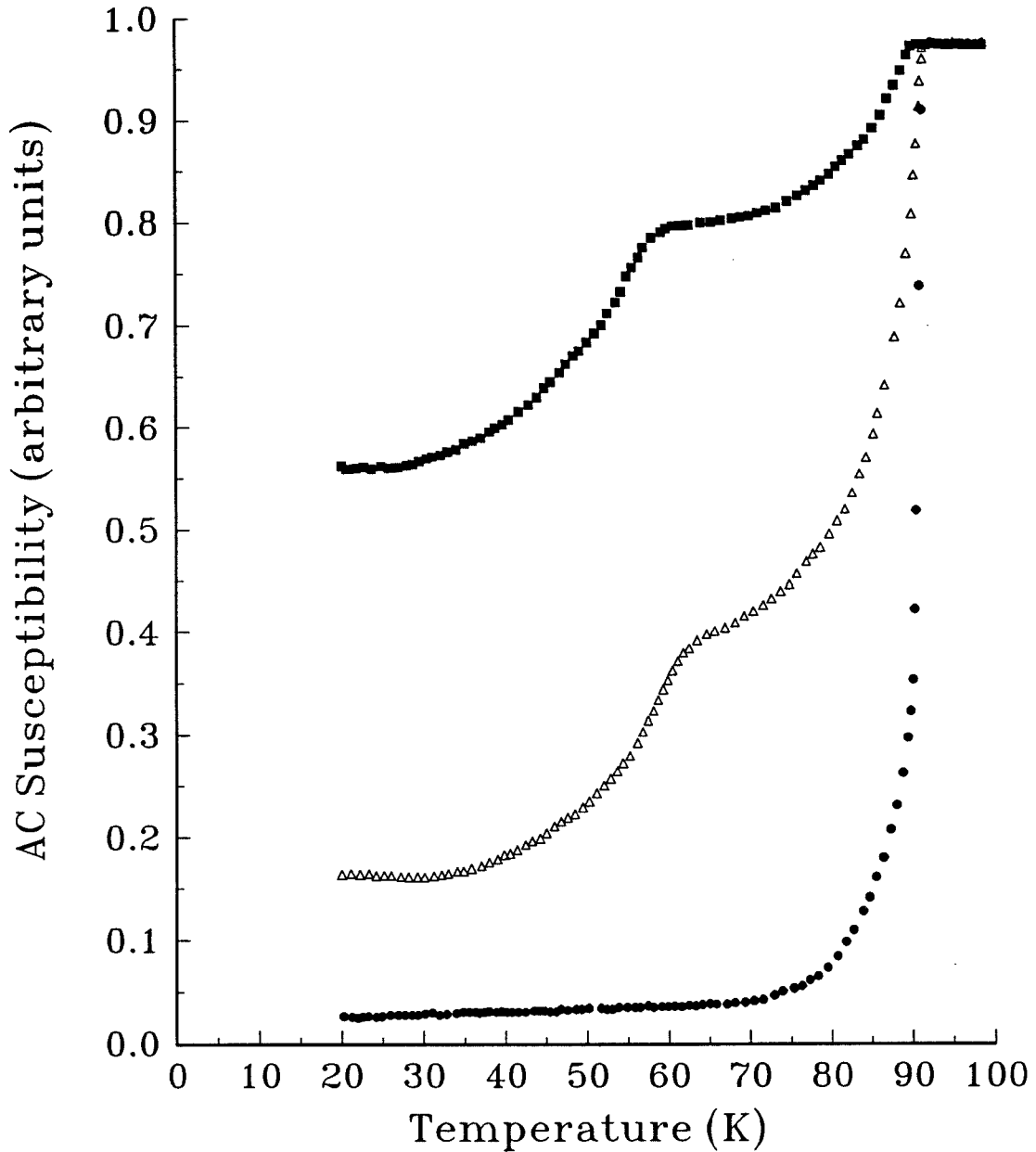


Figure 1.4– AC susceptibility for different samples of YBa$_2$Cu$_3$O$_{6+\delta}$. The top sample was annealed in Argon at 300°C for 4 days. It shows that the material is predominantly a 55K superconductor. The middle sample was quenched from 600°C in oxygen. It shows both 55K and 90K transitions. The final signal is a clean 90K superconductor.

# Universal Bond Length Correlation
## in $YBa_2Cu_3O_{6+\delta}$
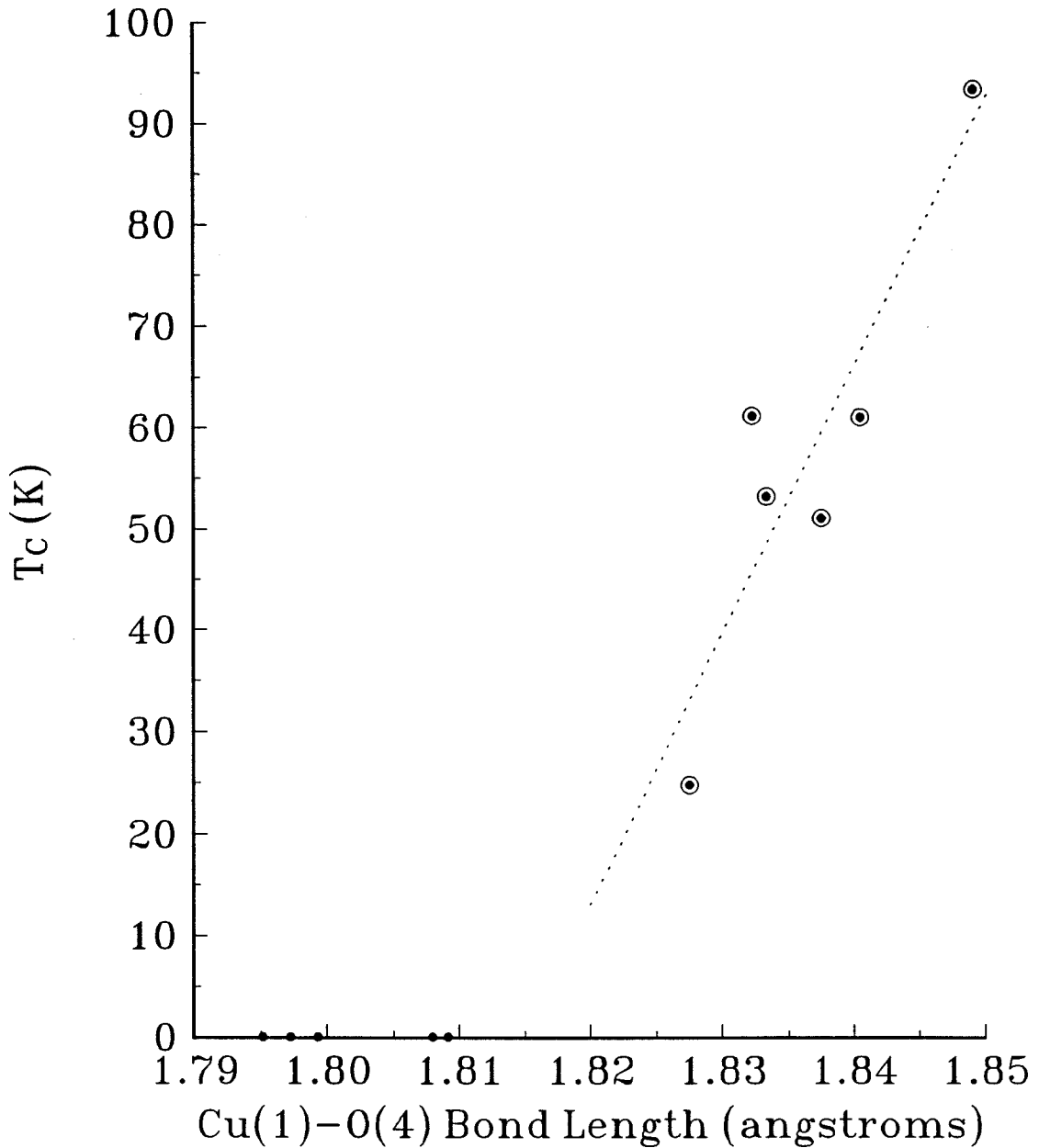


Figure 1.5– The universal correlation between Cu(1)-O(4) bond length and superconducting transition temperature (adopted from Greene and Bagwell).

oxygens also transfers electrons to the CuO planes and correspondingly removes holes from the plane.[16,17]

In addition to the change in transition temperature that is observed, there is a significant change in the behavior of the normal state resistivity. This is shown in figure 1.6. Explanations for the normal state behavior of this class of superconductors, which seems to change continuously from metallic to semiconducting to insulating as oxygen content decreases from a value of about $O_7$ to a value of about $O_6$ (per unit cell), has been and is still a hotly debated topic.

# Resistivity of YBa$_2$Cu$_3$O$_{6+\delta}$
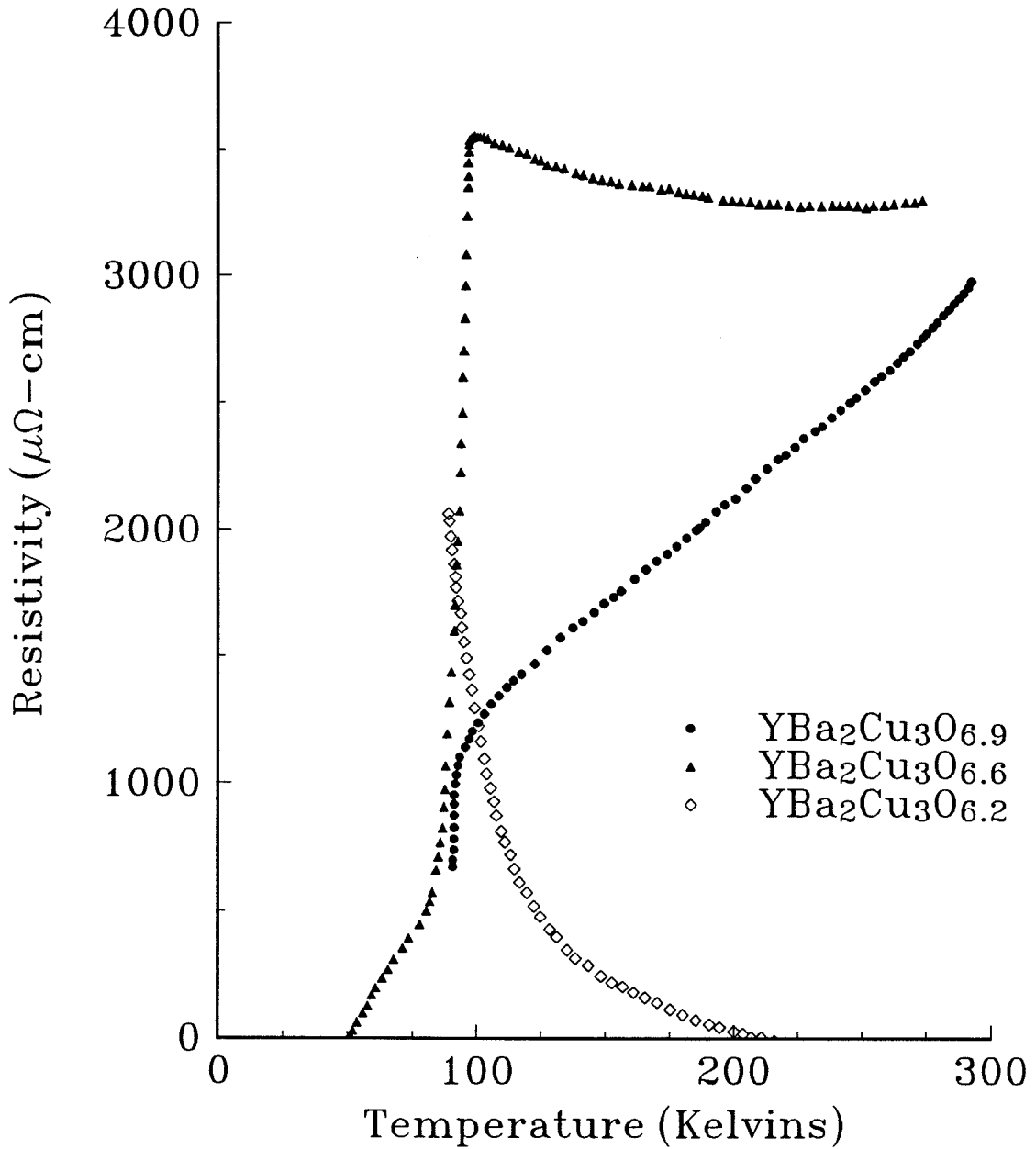


Figure 1.6– The resistivity of samples of YBa$_2$Cu$_3$O$_{6+\delta}$ with varying oxygen content.

### I.B.1 Background and Impetus for the Mechanical Milling of $YBa_2Cu_3O_{6+\delta}$

Over the past few years, virtually every conceivable method has been used to synthesize $YBa_2Cu_3O_{6+\delta}$ in powder, single crystal, thick film and thin film form. Standard solid state reaction sintering, melt-growth processes, spray pyrolysis, thermal coevaporation, magnetron and RF sputtering, chemical vapor deposition and even molecular beam epitaxy have all been used with varying degrees of success. The production of $YBa_2Cu_3O_{6+\delta}$ powder is still primarily accomplished through solid state reaction (what has come to be known as the "heat, beat and treat" approach). However, this process require extremely fine mixing to ensure that the resulting powder is homogeneous. A difficulty arises because the constituent oxide powders with which one begins are typically large particles (one micron or more) and massive yttrium and barium atoms must move huge distances (atomically speaking) during the sintering process to form $YBa_2Cu_3O_{6+\delta}$. Temperatures in excess of 900°C are often required to get such huge atoms to move the required distances in reasonable amounts of time.[18] One way to reduce the problem is to begin with finer particles; the oxides are quite brittle and mechanical alloying of the oxides reduces the starting particle size. It is possible to take the process one step further and increase the energy transmitted to the particles during milling with the hope of forming the $YBa_2Cu_3O_{6+\delta}$ compound directly, with only a relatively low temperature oxygen anneal afterward to take the material through its orthorhombic-tetragonal phase transition and thus optimize its superconducting properties. This was recently demonstrated by Lavallée et al.[19]

Wier et al.[20] were among the first to use mechanical energy to assist the chemical formation of $YBa_2Cu_3O_{6+\delta}$ powder. Unlike Lavallée et al., who used ball-milling, they

subjected the powder to shock-wave compaction and found that the resulting material exhibited an increase in flux pinning energy. That is, the material was able to carry a higher critical current density when superconducting than powders made from standard sintering techniques. One explanation offered for the observed enhancement of the criticial current, $J_C$, in the consolidated solid was the creation of stronger pinning sites associated with a configurational disordering on the cationic sites. The same defect has also been proposed as an explanation for the observed enhancement in $J_C$ for bulk powder samples that have been irradiated.[21,22] Thus, the milling process, which is capable of introducing disorder on an atomic scale, may improve the pinning properties of powder high temperature superconductors.

One might imagine mechanical milling of the $YBa_2Cu_3O_{6+\delta}$ powder to produce a fine-grained powder with enhanced current carrying capabilities (due to defects, which would act as pinning centers for the flux lattice). This powder could then be textured by recrystallizing it with large seed crystals in an extrusion type process to fabricate wires with superior critical current carrying capacity relative to unmilled powder.

There was one additional reason to study the effect of mechanical milling on, specifically, the $YBa_2Cu_3O_{6+\delta}$ powder. Researchers in the field of thin film high temperature superconductors found that many of their $YBa_2Cu_3O_{6+\delta}$ films had less than ideal characteristics. They discovered that even when they grew their films within the stability field proposed by Bormann et al.,[23] they would still find the superconducting transition temperature of their films to be reduced – so much so that often the $T_C$ of the film was below the magical bottom limit of 77K (which corresponds to the boiling point of liquid nitrogen). This was not acceptable and an informal crusade was begun to systematically solve the problem of the "expanded c-axis."

Matsojevic et al.[24] hypothesized that if the cations in the structure were somehow disordered on their sites, this might cause an expansion of the c-axis. High resolution studies on thin films in the TEM were highly suspect because of the necessity of

mechanical grinding of some sort during the preparation process and anyhow did not show

the displacement of cations on their sites. X-ray rocking curve studies were attempted

here,[25] but failed to show any systematic correlation between c-axis expansion and cation

disordering.[26] These experiments were hindered by the relatively poor quality of (even the

best of) the films, which were often highly textured, but not epitaxial.

In light of the difficulty of studying the c-axis expansion in thin films, it was

decided to attempt to reproduce the expansion in powders. The simplest way to introduce

disorder was by mechanical milling.

## I.B.2    The Technique of Mechanical Milling or Ball-Milling

Mechanical milling, or equivalently, ball-milling, is a technique that has been used

to make highly nonequilibrium alloys or alloys of materials (usually elemental metal

powders) that are normally difficult or impossible to form by conventional methods. An

example would be an alloy between two metals with a large difference in their melting

points. Even though two such metals may form a solution in the liquid state, the metal

with the lower melting point tends to separate out in the course of cooling and

solidification.

Technically, the term for the process of using a ball mill to produce alloys of

elemental powders is "mechanical alloying" and not "mechanical milling"; mechanical

milling refers to the process of using a ball mill on a premade alloy, as in the case of ball-

milling of $YBa_2Cu_3O_{6+\delta}$ powder. Nonetheless, the important aspect is the subjection of

powders to high energy mechanical deformation using a vibratory ball mill. Such

processing has found its greatest application in the production of precursor powders for

aluminum, nickel and iron based superalloys, but has also been used as a method to

produce alloys for protective coatings and other nonstructural applications.[27] Specifically,

the process has been used to produce amorphous,[28] nanocrystalline,[29] quasicrystalline,[30] stable intermetallic[31] and superconducting intermetallic[32] compounds. Usually, the final state of the system is one of higher configurational disorder than the initial state.

In the process, powdered components are forcibly intermixed by repeated crushing together in a rapidly shaking vial filled with steel balls (hence "ball-milling"). The technique is characterized by collisions between tool and powder which result in powder fragmentation and coalescence. Although the details of the milling process are poorly understood, it is clear that there are two predominant geometries for these collisions: the powder may be trapped between two balls or it may be trapped between a ball and the wall of the vial. It is generally accepted that the process involves a continual and repeated coalescence and fragmentation of the powders.[33] An illustration of the process is shown in figure 1.7.

Milling experiments are generally characterized by two experimental variables: milling time and ball-to-powder ratio. Milling time is simply the length of time a powder mixture has been subjected to mechanical milling. Ball-to-powder ratio is the mass of the balls used to the mass of loose powder placed in the vial at the start of the experiment. The actual experiment is not so cleanly defined because during the initial phase of milling, powder coats both the walls of the vial and the balls. The amount of powder lost to coating can be significant, especially with very pure elemental metal powders which have no surface passivation.[34] Because of this, the ending ball-to-powder ratio is almost always greater than what it was at the start of milling.

**COALESCENCE EVENTS**          **FRAGMENTATION EVENTS**
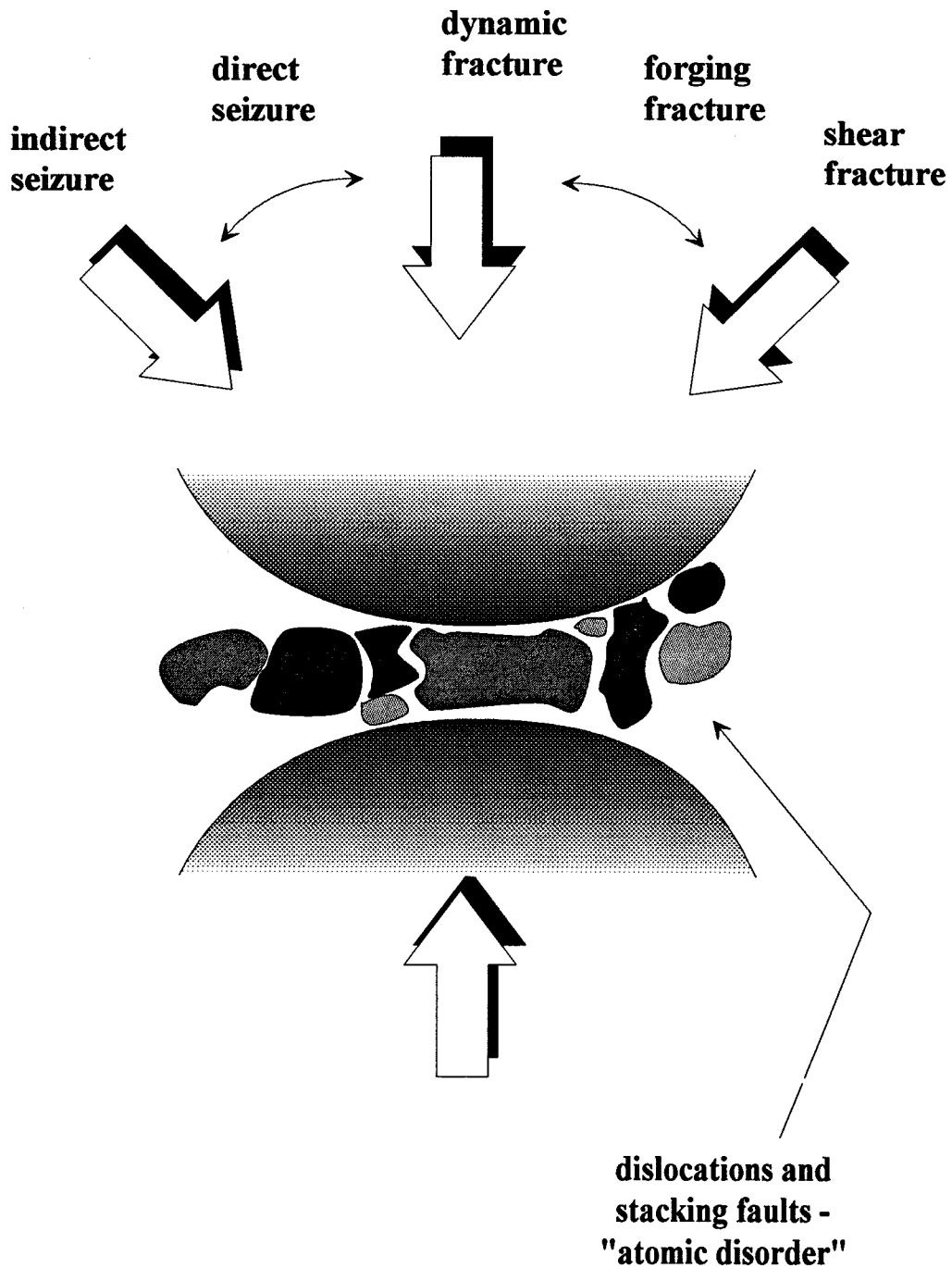


Figure 1.7– An illustration of the major effects of mechanical milling on powder samples.[35]

# REFERENCES FOR CHAPTER 1

[1] for example,

B. Schechter, The Path of No Resistance (Simon and Schuster : New York), 1990.

[2] although recently, C60 doped with Rb was found to be superconducting at above 30K!

[3] M. K. Wu, J. R. Ashburn, C. J. Torng, P. H. Hor, R. L. Meng, L. Gao, Z. J. Huang, Y. Q. Wang and C. W. Chu, Phys. Rev. Lett. **58** 1987, p. 908.

[4] As is pointed out by J.C. Phillips in his book, Physics of High-Tc Superconductors, The Lanthanum containing compound, $La_2CuO_{4-\delta}$ was originally developed as a potential oxygen sensor.

[5] ibid.

[6] Jorgensen, Beno, Hinks, Soderholm, Volin, Hitterman, Grace, Schuller, Segre, Zhang, and Kleefisch, Phys Rev B **36**, (1987) p.3608.

[7] ibid, p. 3608.

[8] Murphy et al., *Chemistry of High Temperature Superconductors,* eds. D. Nelson, M. Stanley Whittingham and T. George, (ACS, Washington D. C., 1988), ch. 18, p. 181.

[9] D. M. Ginzberg, *Physics of High Temperature Superconductors* (World Scientific, Singapore, 1989), p. 213.

[10] ibid, p. 213.

[11] op. cit., Tarascon et al., *Chemistry of High Temperature Superconductors,* ch. 20, p. 198.

[12] op. cit., Greene and Bagwell, *Physics of High Temperature Superconductors.*

[13] ibid.

[14] Aukrust, Novotny, Rikvold and Landau, Phys. Rev. B **41** (1990), p. 8772.

[15]Berera and deFontaine, Phys. Rev. B **39** (1989), p. 6727.

[16]op. cit., Greene and Bagwell, *Physics of High Temperature Superconductors*.

[17]J. M. Tranquada, S. M. Heald, A. R. Moodenbaugh and Y. Xu, Phys. Rev. B **38** (1988), p. 8893.

[18]see section II.A.1 for a discussion of sample preparation via solid state reaction sintering.

[19]F. Lavallée, M. Simoneau, G. L. Espérance and R. Schulz, Phys. Rev. B **44** (1991), p. 12003.

[20]S. S. T. Wier, W. J. Nellis, M. J. Kramer, C. L. Seaman, E. A. Early and M. B. Maple, Appl. Phys. Lett. **56** (1990), p. 2042.

[21]J. D. Jorgensen, B. W. Veal, W. K. Kwok, G. W. Crabtree, A. Umezawa, L. J. Nowicki and A. P. Paulikas, Phys. Rev. B **36** (1987), p. 5731.

[22]J. W. Lee, H. S. Lessure, D. E. Laughlin, M. E. McHenry, S. G. Sankar, J. O. Willis, J. R. Cost and M. P. Maley, Appl. Phys. Lett. **57** (1990), p. 2150.

[23]R. Bormann and J. Nolting, Appl. Phys. Lett. **54** 1989), p. 2148.

[24]V Matijasevic, P. Rosenthal, K. Shinohara, A. Marshall, R. Hammond and M. Beasley, J. Mat. Res. **6** (1991), p. 682.

[25]by Lee, Kittl and Nieh.

[26]The study showed that there was in fact some cationic disordering. However, there was no correlation seen.

[27]D. R. Maurice and T. H. Courtney, Met. Trans. A **21A** (1990), p. 289.

[28]C. C. Kock, O. B. Cavin, C. G. McKamey and J. O. Scarbrough, Appl. Phys. Lett. **43** (1983), p. 1017.

[29]E. Hellstern, H. Fecht, Z. Fu and W. Johnson, J. Appl. Phys. **65** (1989), p. 305.

[30]J. Eckert, L. Schultz and K. Urban, Appl. Phys. Lett. **55** (1989), p. 117.

[31]J. Eckert, L. Schultz, E. Hellstern and K. Urban, J. Appl. Phys. **64** (1988), p. 3224.

[32]E. Hellstern, L. Schultz, R. Bormann and D. Lee, Appl. Phys. Lett. **53** (1988), p. 1399.

[33]Maurice and Courtney, Met. Trans. A **21A** (1990), p. 289.

[34]private communication, Yoshio Abe.

[35]adapted from:

     Maurice and Courtney, Met. Trans.A **21A** (1990), p. 290.

## II.    Characterization of Equilibrium Oxygen Content in YBa₂Cu₃O₆₊δ as a Function of Oxygen Chemical Potential

*Overview-*

The equilibrium relationships between partial pressure of oxygen, temperature, lattice parameters and oxygen content in the $YBa_2Cu_3O_{6+\delta}$ superconductor were examined by differential scanning calorimetry (DSC), high-temperature x-ray diffraction (Hi-T XRD), thermogravimetric analysis (TGA) and measurement of pressure versus concentration isotherms (P(c) isotherms).  Oxygen pressures ranged from 1 mbar to 1013 mbar and temperatures ranged from 400°C to 750°C.  Lattice parameters as a function of temperature and partial pressure of oxygen were measured.  Pressure-concentration isotherms and TGA were used to measure oxygen content as a function of temperature.  A phase line separating the low temperature orthorhombic phase and the high temperature tetragonal phase was determined.  No evidence of a miscibility gap between the two phases was found in the range of temperatures and oxygen pressures explored.  From the data, the excess enthalpy and entropy through the orthorhombic to tetragonal phase transition was calculated.  It was found that the excess entropy is less than the entropy of mixing for an ideal solution.  DSC was used to measure enthalpies for the transition and to calculate activation energies for the process.  The enthalpy for the evolution of oxygen from the solid was found to be 5.2 kJ/mol in Argon, 2.0 kJ/mol in 16% oxygen and 1.7 kJ/mol in pure oxygen.  Activation energies for the transition were 1.2 eV/atom in Argon, 1.8 eV/atom in 16% oxygen, and 2.9 eV/atom in 100% oxygen.  DSC using a sealed sample pan (to maintain a constant concentration of oxygen in the solid during heating) was done and no signal arising from the order–disorder transition was seen.  However, in order to prevent the mechanical failure of the pan due to internal pressure buildup, very small quantities of sample were required.  It is believed that the amount of sample used was so small that the signal fell below the sensitivity of the DSC.  Computer models for

the transition in the literature were examined and good predictions of the orthorhombic-tetragonal phase line were obtained. The models, though, proved inadequate in their calculations of the various thermodynamic functions. A two-dimensional anisotropic Ising model, modified to include a linear concentration dependence for the heat of solution, was found to provide the most realistic predictions for the pressure-concentration isotherms when compared to our and other published experimental data.

## II.A.   Thermodynamics of the Orthorhombic-Tetragonal Transition

### II.A.1.   Experimental Details of the Pressure versus Concentration Isotherms

Pressure versus concentration isotherms (P(c) isotherms) were measured for the orthorhombic to tetragonal phase transition (O-T transition) using a volumetric analysis setup as shown in figure 2.1.  Samples were placed in a furnace at a specific temperature and allowed to equilibrate with a known partial pressure of oxygen.  From the data, the chemical potential, the partial molar enthalpy and entropy of oxygen in $YBa_2Cu_3O_{6+\delta}$ were determined as a function of $\delta$.

The system consists of a quartz tube in which the sample sits, a furnace, a vacuum pump and a pressure gauge.  A powder sample was used instead of a sintered disk in order to enhance the exchange rate of oxygen between gas and the solid.  The sample temperature was measured independently from the furnace regulation system by a shielded Chromel-Alumel thermocouple adjacent to the sample tube in the furnace.

The powder samples were prepared by mixing 99.99% pure $Y_2O_3$, $BaCO_3$ and CuO in a Y:Ba:Cu cation ratio of 1:2:3  in an agate mortar and pestle.  The mixture was then pressed into pellets and laid on Platinum foil to be fired in flowing oxygen at 960°C for approximately 16 hours.  After this initial step, which served to both calcine the $BaCO_3$ and sinter the "123," the pellets were ground and pressed into pellets a second time.  This second firing was done at 960°C in flowing oxygen for approximately 4-6 hours then oven-quenched to 500°C  where they were held for several hours before being brought slowly to room temperature.  The resultant material was single phase to the detectability limit of the x-ray diffraction patterns.  Chemical analysis on the powders was done on a Phillips EM430 transmission electron microscope equipped with an energy-dispersive x-ray detector (EDX).  EDX gave a Y:Ba:Cu ratio of 1:2:3 to within statistical

**Extra Volume Can**

**Wallace & Tiernan Pressure Gauge**

**Valve 3**

**Valve 1**

**Valve 2**

**To Oxygen Gas Source**

**To Vacuum Pump**

**Quartz Sample Tube**

**Furnace**
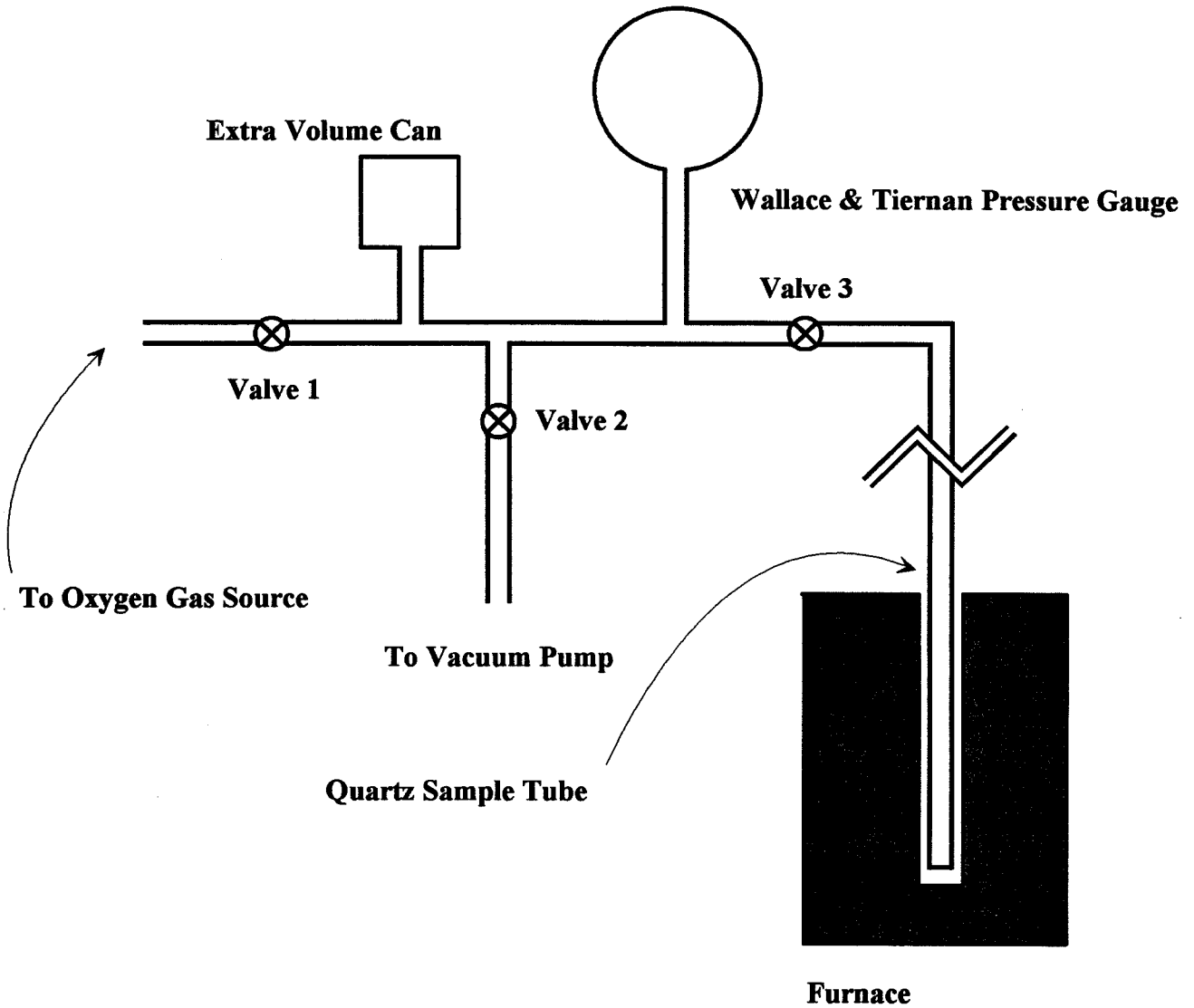
Figure 2.1– The volumetric analysis setup used to measure pressure-concentration isotherms.

accuracy (approximately 3-5%). Powders for the DSC scans were made by grinding the pellets in an agate mortar and pestle. Samples for the TEM were prepared by grinding pellets in a solution of Methylene Dichloride. Samples were stored in a dry oxygen dessicator with $P_2O_5$ dessicant until they were used.

Powders were also purchased from Aesar Corporation and Kalie-Chemie Corporation for comparison. There were no significant differences in any of the experimental results.

The samples used in the P(c) isotherm measurements were characterized by x-ray diffraction to be single phase with room temperature lattice constants of a=3.820(3)Å, b=3.889(3)Å and c=11.670(3)Å. The diffraction pattern of the starting material is shown in figure 2.2 with indexing of the major polycrystalline peaks. The superconducting transition temperature of the sample powders was $T_{onset}$= 92K with a superconducting transition width (10%-90%) of less than 3K. These characteristics remained unchanged after the experiments were completed.

After placing the sample in the furnace, it is annealed in vacuum for several hours at 750°C to bring its oxygen content to a minimum (thermogravimetric analysis on such a sample later showed this minimum to be δ~0.10±0.03. The sample is then brought to the temperature of interest under vacuum. Valves 2 and 3 are closed and a known amount of high purity oxygen is let in through valve 1 into the extra volume can. The pressure from this amount of oxygen is read from the gauge. Valve 2 is then opened and the known amount of oxygen is allowed to equilibrate with the sample. The pressure is again read after equilibrium has been reached, which was defined as no change in pressure over the period of one hour.

The pressure gauge has a pressure dependent volume correction which resulted in a total available volume:

$$V_{total} = (111.33 + 0.2543p) \text{ cm}^3,$$
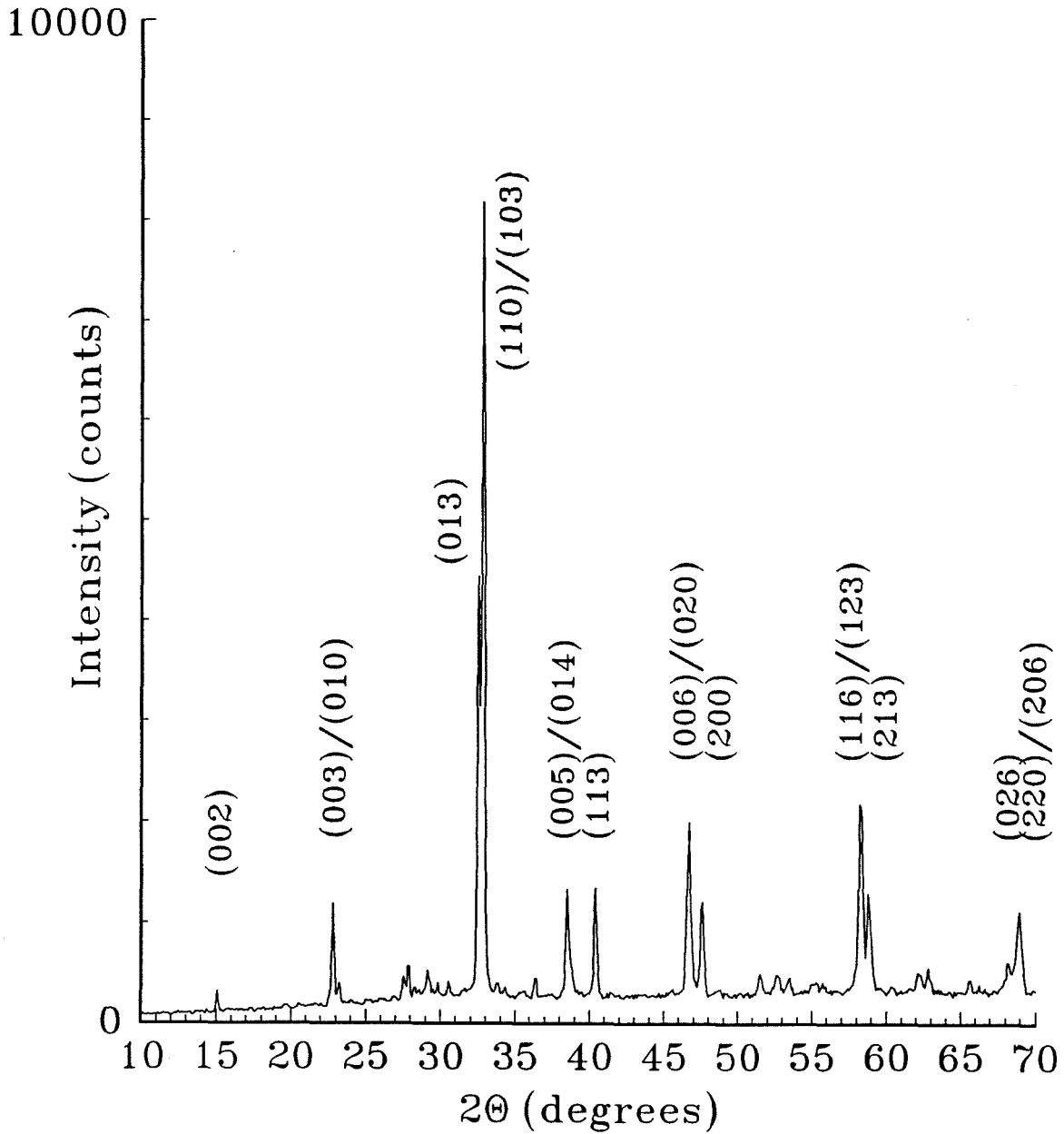
Figure 2.2– An x-ray diffraction pattern of the starting $YBa_2Cu_3O_{6+\delta}$ powder with the major powder peaks indexed.

where p is the pressure measured in psi. The volume past the second valve is:

$$V_2 = 21.574 \text{ cm}^3.$$

The volume at furnace temperature is:

$$V_F = 0.614 V_2 = 13.246 \text{ cm}^3.$$

The volume at room temperature is therefore:

$$V_r = (98.084 + 0.2543p) \text{ cm}^3.$$

The pressure-concentration isotherms taken with this setup are shown in figure 2.3a.

Another measuring algorithm was used to cross check this data. In the second method, absorption runs were performed on samples that had been fully reduced by annealing in vacuum at 750°C. After annealing to insure minimum oxygen content, a fixed amount of oxygen was introduced into the sample and gas can chambers and the temperature was stepwise reduced from 750°C at 50°C intervals. After equilibration at each temperature, the temperature was reduced to the next temperature. This experiment led to a series of data points shown by the dashed line on figure 2.3a. The fact that this measuring algorithm reproduced exactly the results from the first method of measurement allows one to conclude that the system was in equilibrium throughout the course of the experiment. Therefore, any kinetic effects that might be associated with the uptake or desorption of oxygen in the compound at shorter time scales were not present. Moreover, Shi et al.[1] have done extensive studies of the time-temperature-transformation diagram in the system and have shown that above 400°C., the oxygen atoms are extremely mobile. Within twenty minutes, they reach equilibrium values for the oxygen content. Their data and our own studies with *in situ* high temperature x-ray diffraction (which will be shown later) and the correspondence of the data from two distinct measuring algorithms show that the measured points for the P(c) isotherms are equilibrium data. Their data is shown in figure 2.3b.

The oxygen content at a given pressure and temperature could be evaluated by ideal gas law calculations because sample mass, sample chamber volume, gas can volume, pressure difference due to oxygen absorption/desorption and effective gas temperature were all known quantities. The effective gas temperatures were measured by carrying out similar runs without sample powder present in the sample tube. Finally, the volume of the pressure gauge changes with pressure in a known manner and the volumes at furnace temperature and at room temperature are all known.

P(c) isotherms measure relative changes in the oxygen content of $YBa_2Cu_3O_{6+\delta}$ by measuring actual changes in the number of moles of oxygen gas left in the closed system. However, to determine the absolute value of $\delta$ in the material, thermogravimetric analysis (TGA) was done on the powder samples.[2] The TGA was done on the initial sample that had been annealed in vacuum at high temperature for several hours and again on the final sample to check that there was no long term change to the sample. In TGA, a sample is heated while its mass is monitored. The samples were heated in Argon atmosphere at 10K/minute and the final endproducts were $Cu_2O$, $BaO$ and $Y_2O_3$. To ensure that no cations were lost to a gaseous phase, EDX was performed on the decomposed products. The ratio of cations was still 1:2:3. Since the cations remain in solid phase, any mass loss can be attributed to the loss of oxygen from this decomposition reaction. The choice of final products was then confirmed by x-ray diffraction. TGA gave a value of $\delta{\sim}0.15{\pm}0.03$ for the "fully discharged" tetragonal samples. A sample that had been "fully charged" with oxygen (i.e., annealed at 450°C for several hours and slowly cooled to room temperature) was also measured with TGA and gave a value of $\delta{\sim}0.94{\pm} 0.03$. This served as a check for the experimental calculations. Samples that have been "fully discharged" are referred to as $YBa_2Cu_3O_6$ for simplicity. Likewise, samples that have been "fully charged" are referred to as $YBa_2Cu_3O_7$.

# Pressure vs. Concentration Isotherms
## in $YBa_2Cu_3O_{6+\delta}$
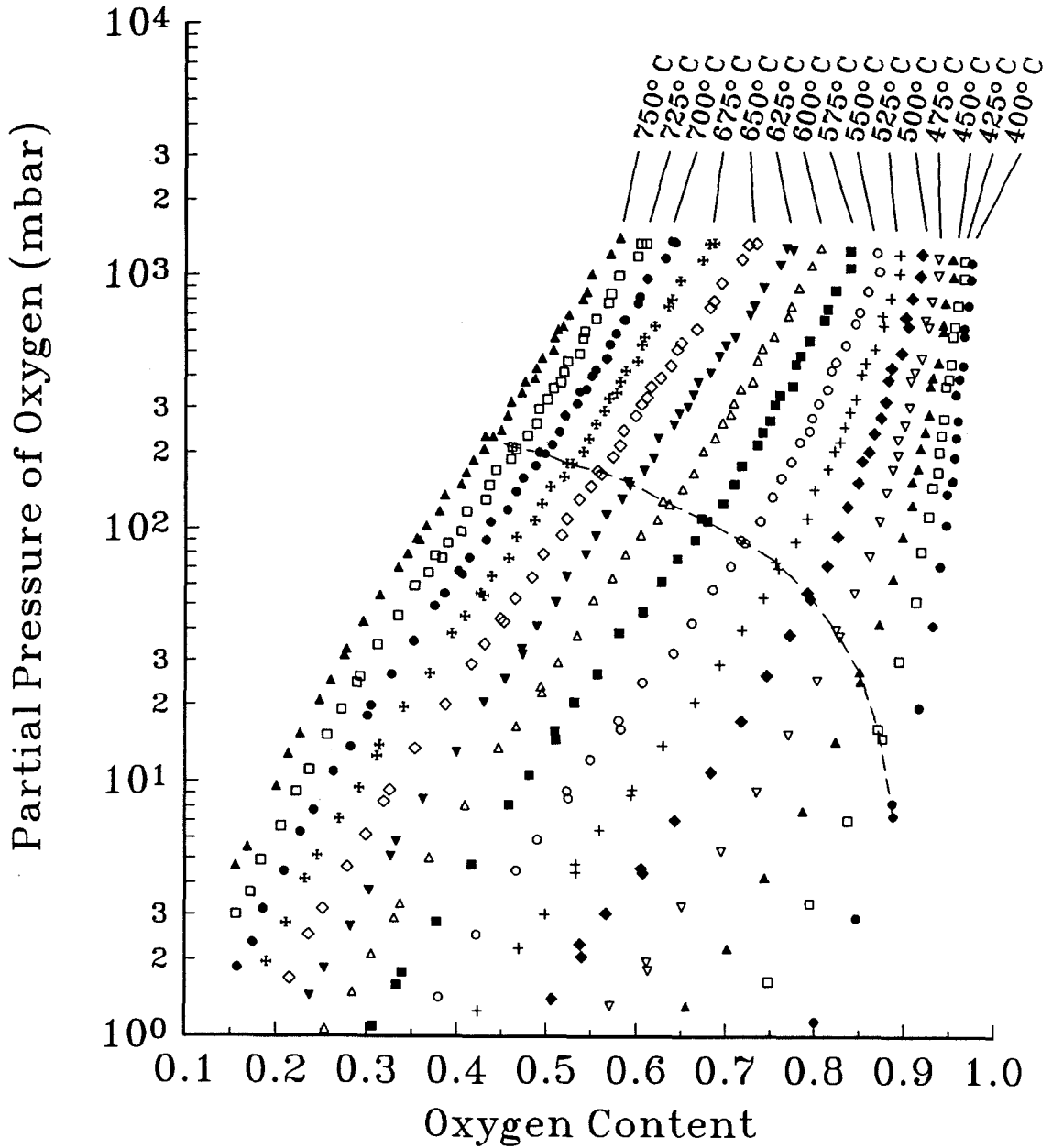


Figure 2.3a– The pressure-concentration isotherm data.

# Oxygen Content versus Anneal Time
## in $YBa_2Cu_3O_{6+\delta}$
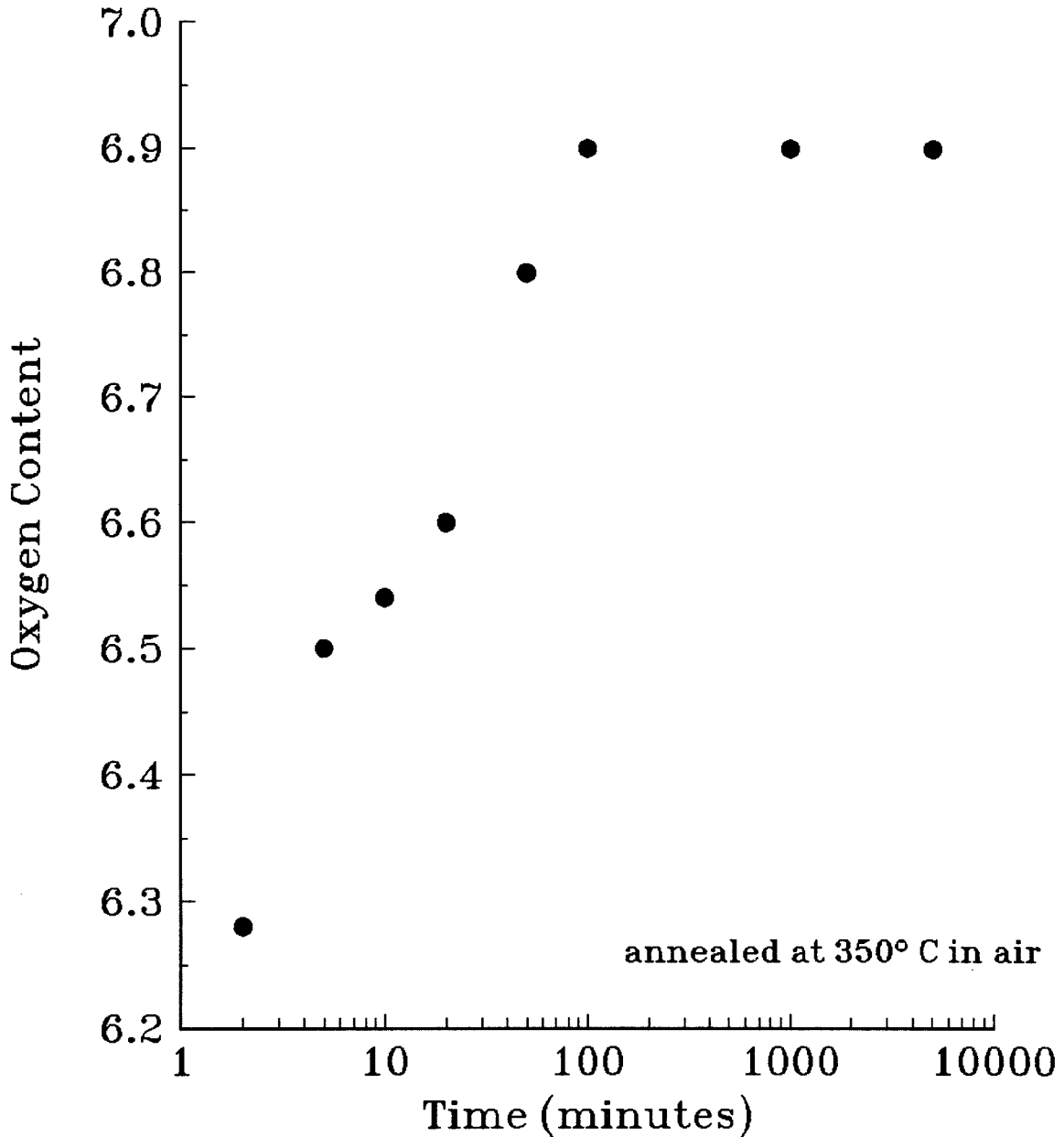


Figure 2.3b– Data from Shi et al.[3]  The data is for a sample annealed at 350°C in air.

### II.A.2. Experimental Results

The results of the P(c) isotherms are shown in figure 2.3a, where they have been plotted versus the amount of oxygen in the formula unit for the material. Uncertainties in δ are on the order of ±2% in relative error due primarily to errors in reading the pressure and temperature and errors in volume measurement and effective temperature calibration. The data displayed are absorption data for both algorithms of measurement described in the previous section. In the first algorithm, the powders were taken to a minimum oxygen configuration (750°C under vacuum) then cooled to the target temperature and allowed to equilibrate with a known amount of oxygen gas. In the second algorithm, a known amount of oxygen gas was introduced into the sample chamber at 750°C, and the powder/gas mixture was allowed to equilibrate before stepwise reducing the temperature further. Desorption runs were done occasionally and no differences were found once equilibrium had been established. It should be noted that there seemed to be a difference in the amount of time necessary for equilibrium to be established depending on whether or not the starting material was orthorhombic or tetragonal. This is not surprising since in outgassing, the oxygen atoms must combine to form diatomic molecules and in adsorption, they must break apart and find a lattice site. The two processes can have different energies.

### II.A.3. Discussion of Experimental Findings

As can be seen from the data, within the temperature and composition ranges examined, there were no plateaus observed; a miscibility gap between the orthorhombic

and tetragonal phases (or a mixture of two orthrhombic phases, as will be discussed later) does not seem to exist in this region of the phase diagram. The P(c) isotherms increase monotonically with increasing $\delta$ over the whole range. Although none of the isotherms exhibit any discontinuities or sharp changes in curvature, some of the lower temperature isotherms do suggest a change in curvature and an inflection at around $\delta \approx 0.55$. Similar observations have been made by Gerdanian et al.[4] and McKinnon et al.[5]

Note that the lower temperature isotherms have an asymptotic character as they approach $\delta \sim 1$. This is an indication that a solubility limit exists at this composition. However, as can be seen from figure 1.1, there are actually two available distinct sites in the Cu(1)-O basal planes for oxygen incorporation (the O[1] and O[5] sites). Because of this, in the ideal mixing regime, there are a maximum of 8 oxygens per formula unit. Furthermore, the data seems to indicate that the solubility limit is independent of temperature and is somewhere near full occupancy of the Cu(1)–O(1) chains.

## II.A.4    Thermodynamic Background for the Experiment

We can write the reaction that incorporates gaseous oxygen into $YBa_2Cu_3O_{6+\delta}$ as follows:

$$\frac{1}{2}O_2(g) \Leftrightarrow O\left(in\ YBa_2Cu_3O_{6+\delta}\right). \tag{II.1}$$
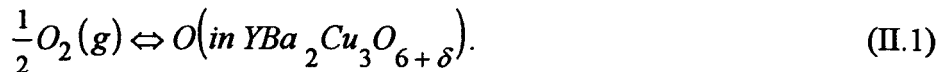
The equilibrium condition for this reaction is then:

$$\mu_{O_2}(g) = \mu_{O_2}^{ref}(123), \tag{II.2}$$

where the notation *"123"* means *"in $YBa_2Cu_3O_{6+\delta}$"* If the assumption is now made that $O_2$ is an ideal gas, then its chemical potential can be expressed by:

$$\mu_{O_2}(g) = \mu_{O_2}^{ref}(g) = RT\ln\left(P_{O_2}\middle/ p_{O_2}^{ref}\right), \tag{II.3}$$

where $\mu_{O_2}^{ref}$ is the standard chemical potential of oxygen gas at a partial pressure of oxygen, $p_{O_2}^{ref} = 1$ atmosphere.

In the solid, we write the chemical potential of one mole of oxygen atoms dissolved in $YBa_2Cu_3O_{6+\delta}$ in a manner that emphasizes its deviation from a random solid solution of oxygen atoms and vacancies. We begin with the hypothetical case of an ideal solid solution in which $\delta=1$. We call this value for the chemical potential $\mu_{O_2}^{ref}$. It serves as the reference chemical potential of oxygen for the solid and includes the site energy for the oxygen atom. A second term in the expression due to the ideal partial configurational entropy of mixing of oxygen atoms on the basal CuO planes is explicitly included. This is the mixing term that would describe the system if it were an ideal solid solution. We assume that oxygen is dissolved only in the basal CuO plane, where two sites, denoted O(1) and O(5), per unit cell are available (these sites are at $(0,\frac{1}{2},0)$ and $(\frac{1}{2},0,0)$. These two terms describe an ideal solution without any interactions between incorporated oxygen atoms. Any deviations from this behavior are grouped into the third term, $\mu_O^E$, the excess chemical potential. Finally, the chemical potential of oxygen in $YBa_2Cu_3O_{6+\delta}$ can thus be expressed per mole of oxygen atoms as:

$$\mu_O(123) = \mu_O^{ref} - RT\ln\left(\frac{2-\delta}{\delta}\right) + \mu_O^E, \tag{II.4}$$

where $\delta$ denotes the number of oxygen atoms in the basal Cu(1) planes per unit cell. The first two terms on the right hand side of this equation then define the ideal chemical potential ($\mu_O^{ref}$ is the reference chemical potential of oxygen in a dilute solution and $R\ln\left(\frac{2-\delta}{\delta}\right)$ is the ideal partial configurational entropy of mixing of oxygen atoms in the

basal Cu(1) plane, or, the random mixing term. $\mu_O^E$ groups all remaining composition dependent terms other than those derived from random mixing, such as oxygen-oxygen interactions (which may be responsible for the solubility limit at $\delta \sim 1$), into an excess chemical potential; $\mu_O^E$ measures just deviations from the ideal case. In the hypothetical ideal solution, $\delta = 1$ and $\mu_O^E$ is zero. As must be true for any infinitely dilute solution, $\lim\limits_{\delta \to 0} \mu_O^E = 0$.

Writing the chemical potential of oxygen in this way allows us to obtain the excess chemical potential, $\mu_O^E$ from the measured equilibrium P(c) isotherms. The quantity that can be measured from the P(c) isotherm experiments is the relative oxygen potential:

$$
\begin{aligned}
\Delta\mu_O &\equiv \mu_O(123) - \frac{1}{2}\mu_{O_2}^{ref}(g) \\
&\equiv \frac{1}{2}RT\ln\left(p_{O_2} \Big/ p_{O_2}^{ref}\right) \\
&= \Delta\mu_O^{ref} - RT\ln\left(\frac{2-\delta}{\delta}\right) + \mu_O^E \\
&= \Delta H_O - T\Delta S_O,
\end{aligned}
\tag{II.5}
$$

where $\Delta\mu_O^{ref} = \mu_O^{ref} - \frac{1}{2}\mu_{O_2}^{ref}(g)$ is the relative reference chemical potential. It is the difference between the reference potential for the solid and the reference potential for an oxygen atom in the gas (which is just one half the reference potential for diatomic oxygen gas). $\Delta H_O$ and $\Delta S_O$ are the relative partial molar enthalpy and entropy of the oxygen in YBa$_2$Cu$_3$O$_{6+\delta}$. Following the construction of $\Delta\mu_O$, we can split these quantities into reference and excess quantities:

$$
\begin{aligned}
\Delta H_O &= \Delta H_O^{ref} + H_O^E \\
\Delta S_O &= \Delta S_O^{ref} + R\ln\left(\frac{2-\delta}{\delta}\right) + S_O^E,
\end{aligned}
\tag{II.6}
$$

where $\Delta H_O^{ref}$ and $\Delta S_O^{ref}$ are the enthalpy and entropy changes that occur when one oxygen atom is incorporated from the gaseous phase into $YBa_2Cu_3O_{6+\delta}$ at $\delta=0$. $R\ln\left(\dfrac{2-\delta}{\delta}\right)$ is the entropy of mixing for an ideal solution. $H_O^E$ and $S_O^E$ are the excess enthalpy and entropy of the chemical potential. These quantities are a measure of how "non-ideal" the oxygen lattice gas is.

## II.B    Further Discussion of Experimental Results

Figure 2.4 is a plot of $\Delta \mu_O^{ref} + \mu_O^E$ vs. $\delta$, as calculated from the equations above. Clearly, $\mu_O(123)$ deviates significantly from that of the ideal solution in which :

$$\Delta \mu_O^{ref} + \mu_O^E = \Delta \mu_O^{ref} = \Delta H_O^{ref} - T \Delta S_O^{ref} \qquad \text{(II.7)}$$

and which does not depend on $\delta$. Note again that there is a change in curvature around the point $\delta \sim 0.55$. As we will see directly from *in situ* high temperature x-ray diffraction, this point corresponds to the orthrhombic-tetragonal phase transition.

By fitting the data for $\Delta \mu_O$ with respect to temperature (and at constant $\delta$) to a linear least squares fit, one can obtain values for $\Delta H_O$ and $\Delta S_O$. The P(c) isotherms were first smoothed with a cubic spline and the smoothed curves were used for calculation. $\Delta H_O$ and $\Delta S_O$ correspond to the intercept and slope of the resulting line. Figure 2.5 shows these plots of $\Delta \mu_O$ versus temperature and the least squares fit straight line through them. The extrapolation of these lines to T=0K gives values for the excess partial molar enthalpies and the slopes of the lines gives values for the partial molar entropies. The dotted line shows the position of the orthrhombic-tetragonal phase boundary in the system, as confirmed by Hi-TXRD. Values for $\Delta \mu_O$ at the O-T phase boundary were interpolated from the curves shown in figure 2.4.

The dependence of $\Delta H_O$ on $\delta$ is shown in figure 2.6. There is a significant drop in the partial molar enthalpy when moving from the tetragonal to the orthorhombic phase. Also, both phases seem to depend weakly on $\delta$. A linear extrapolation of the data in the tetragonal regime gives a reference value of $\Delta H_O^{ref} \approx -80$ kJ/mole(O) at $\delta=0$. The values of $\Delta H_O \approx -76$ kJ/mole(O) at $\delta \leq 0.5$ and $\Delta H_O \approx -83$ kJ/mole(O) at $\delta \geq 0.65$ agree

# Excess Chemical Potential vs. Oxygen Content
## in $YBa_2Cu_3O_{6+\delta}$
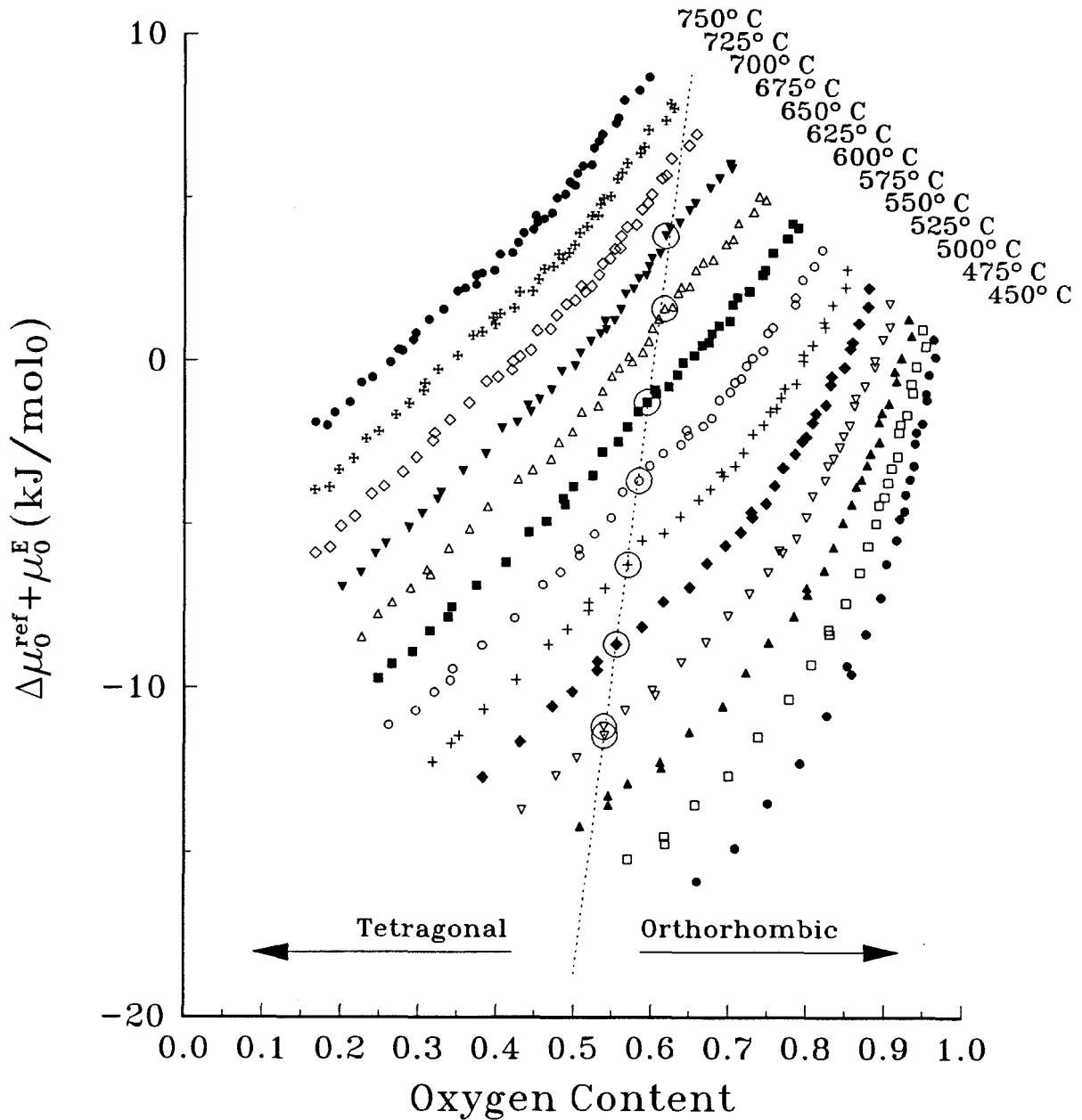


Figure 2.4– Excess chemical potential as a function of oxygen content. The orthorhombic-tetragonal phase line, indicated by a dashed line, was determined experimentally by high-temperature x-ray diffraction.

# Excess Chemical Potential vs. Temperature

## in $YBa_2Cu_3O_{6+\delta}$
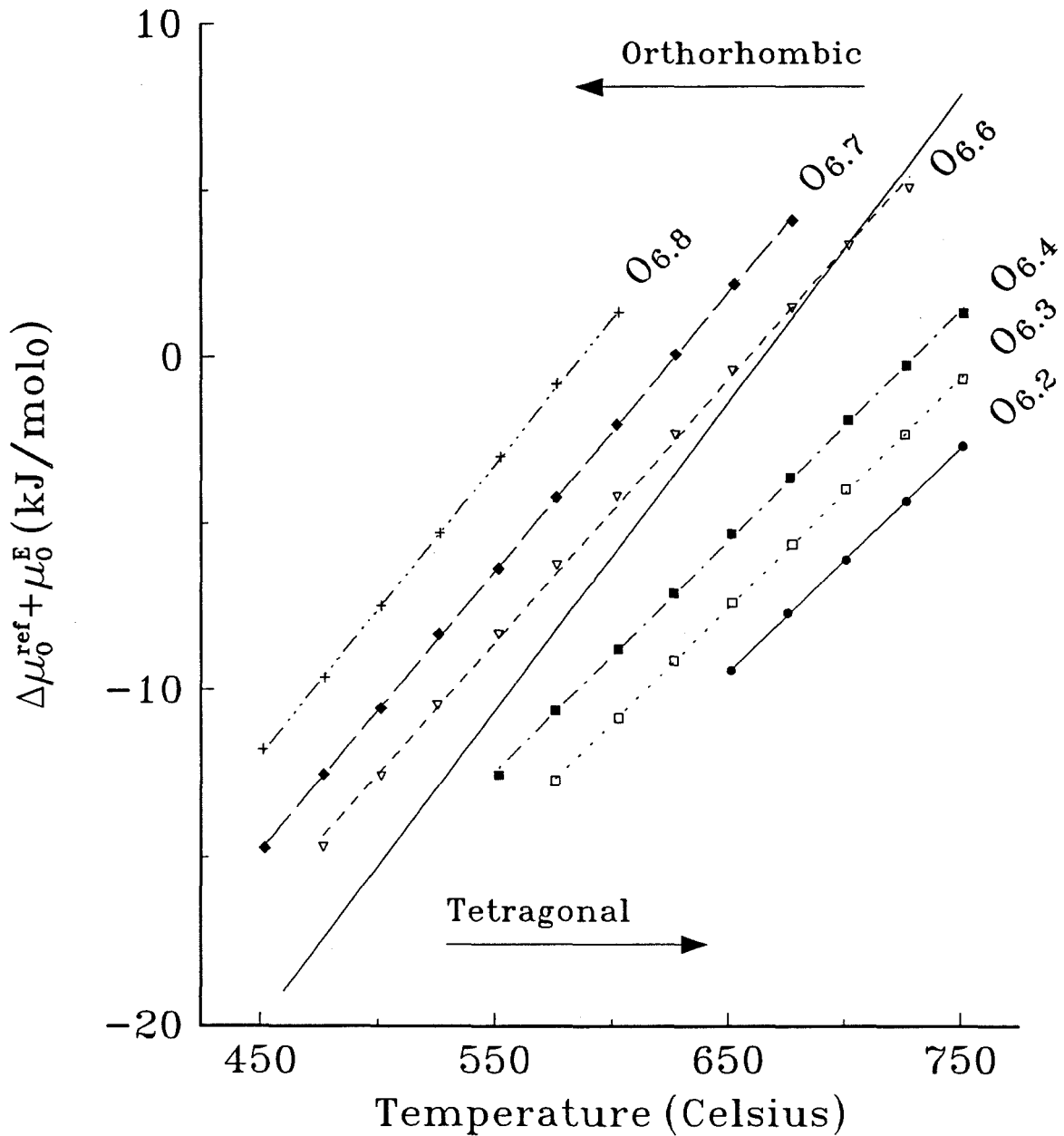


Figure 2.5– Excess chemical potential as a function of temperature. The orthorhombic-tetragonal phase line, indicated by a dashed line, was determined experimentally by high-temperature x-ray diffraction.

# Excess Enthalpy vs. Oxygen Content

## in $YBa_2Cu_3O_{6+\delta}$
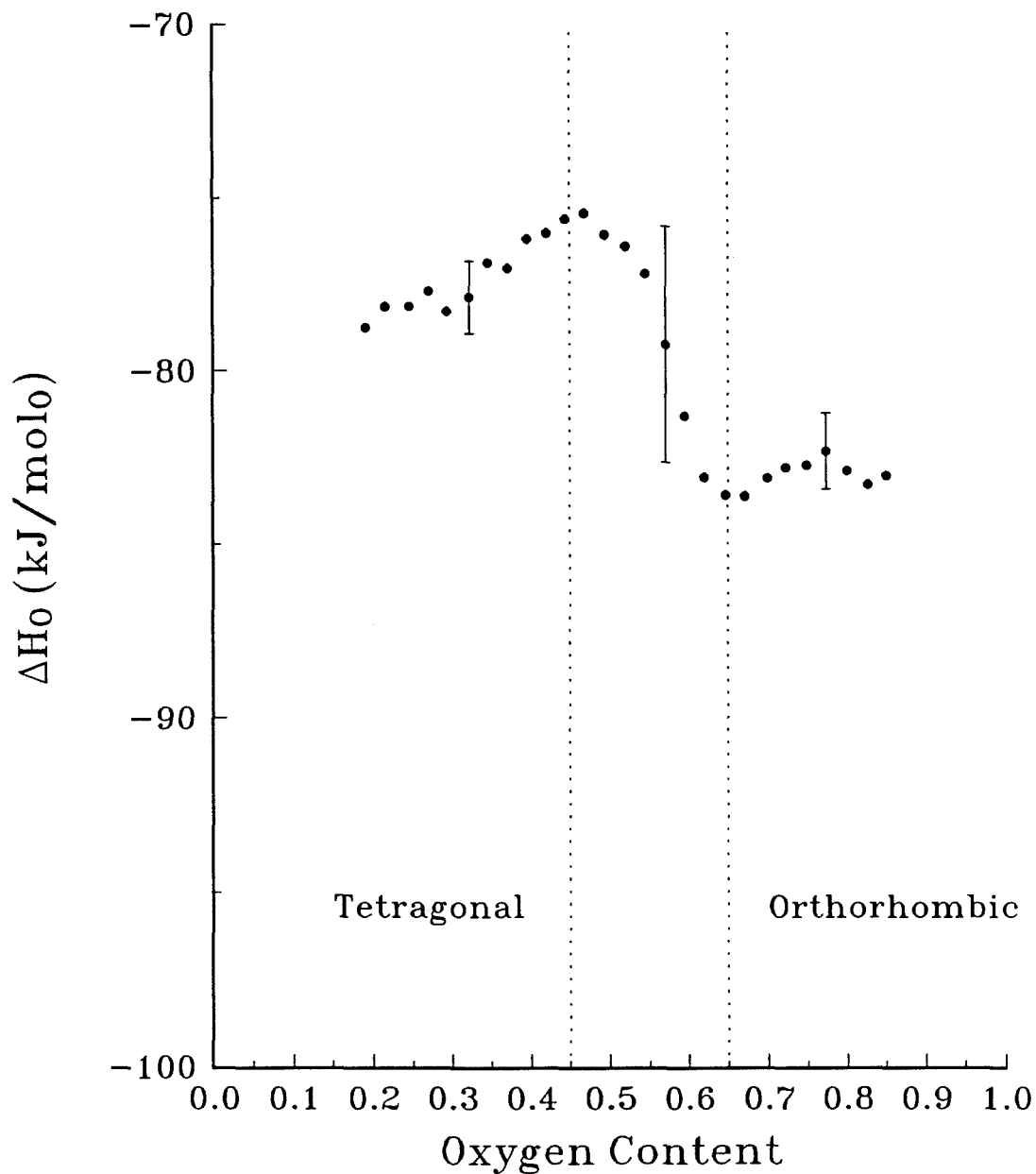


Figure 2.6– Excess enthalpy as a function of oxygen content as calculated from P(c) isotherm data.

reasonably well with the results reported by Gallagher et al.,[6] who found values of $-100$ kJ/mole(O) and $-111$ kJ/mole(O) for the tetragonal and orthrhombic phases, respectively, and results reported by Stroebel et al.,[7] who gave an overall average value of $-74$ kJ/mole(O) for the entire composition range.

The dependence of $\Delta S_O$ on $\delta$ is shown in figure 2.7. Plotted in the same graph is the calculated partial molar entropy for an ideal solution of oxygen, given by:

$$\Delta S_O^{ideal}\left[J/mole\,(O)\cdot K\right] = \Delta S_O^{ref} + R\ln\left(\frac{2-\delta}{\delta}\right). \qquad (\text{II.8})$$

Again, the value for $\Delta S_O^{ref}$ was determined by linearly extrapolating the data for $\Delta S_O^{ref} + S_O^E$ in the tetragonal phase back to $\delta=0$, and was taken to be $-74.0$ kJ/mole-K. It is not possible to do a similar extrapolation on the orthorhombic phase because at $\delta=0$, the material is tetragonal. It can be seen that $\Delta S_O$ is less than the ideal mixing entropy, $\Delta S_O^{ideal}$, over the entire composition range. The deviation from ideal mixing is particularly large in the orthorhombic regime. This is not too surprising since an ideal random solid solution would not exhibit the oxygen chain ordering that results from preferential occupation of O(1) sites in the basal plane. With two available sites, ideal mixing would allow a total of 8 oxygens per formula unit ($\delta$ would have a maximum value of 2).

The uncertainties in $\Delta H_O$ and $\Delta S_O$ are indicated on the plots and exist because the data for $\Delta\mu_O^{ref} + \mu_O^E$ shows some deviation from a purely linear temperature dependence. These deviations are small when the data examined are solely tetragonal or solely orthorhombic: that is, when the data falls in the ranges $\delta<0.5$ or $\delta>0.65$. Larger deviations from linearity occur for intermediate compositions because the corresponding data extends over both phase regimes. Moreover, it should be noted that this data gives average values for $\Delta H_O$ and $\Delta S_O$ over the range of temperatures explored for a given $\delta$.

# Excess Entropy vs. Oxygen Content
## in $YBa_2Cu_3O_{6+\delta}$
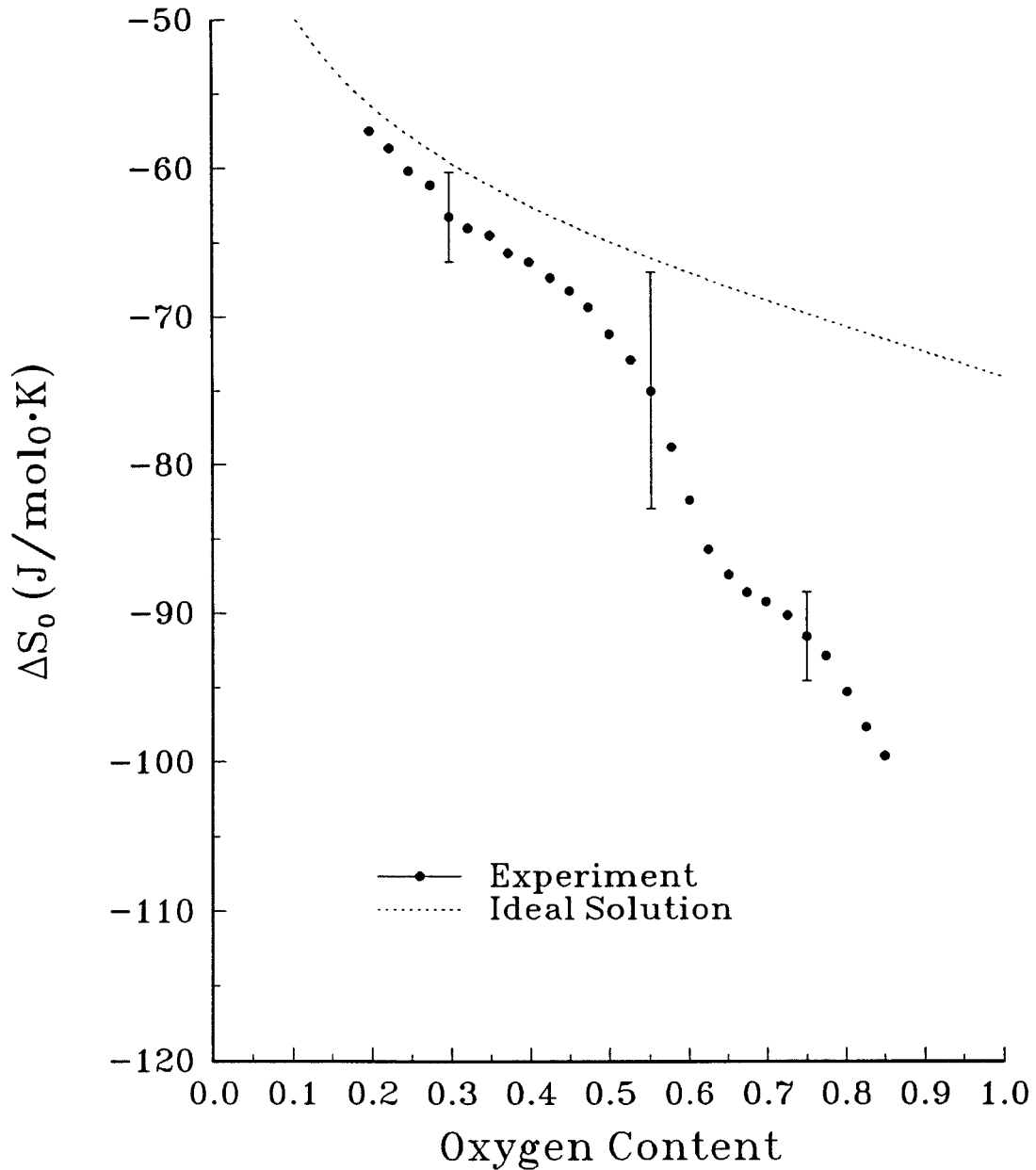


Figure 2.7– Excess entropy as a function of oxygen content as calculated from the P(c) isotherm data. Also shown is the ideal mixing entropy of a random solution.

As a result, the dependencies of $\Delta H_O$ and $\Delta S_O$ on $\delta$ are only an approximate indication of the true behavior, correct only insofar as the values do not depend on temperature. A more accurate representation requires the measurement of $\Delta H_O$ and $\Delta S_O$ vs $\delta$ at fixed temperatures. Gerdanian, Picard and Marucco[8] have taken such measurements using a high precision thermobalance in conjunction with a reaction microcalorimeter. They report that the orthorhombic-tetragonal phase transition is continuous in $\Delta G_O$, the relative Gibbs' free energy of oxygen in the oxide, and that $\Delta H_O$ undergoes a $\lambda$-type discontinuity. Their data for T=600°C is plotted in comparison to the P(c) isotherm measured here in figure 2.8. As can be seen from the figure, there is a shift in the position of the $\Delta H_O$ discontinuity with respect to oxygen content. The location of the $\lambda$–type anamoly measured by Gerdanian et al. is shifted higher by about $\Delta\delta{\sim}0.07$. This is due to the uncertainty in our measurement of $\delta$, which at the endpoints (fully charged and fully discharged) were only accurate to $\pm 0.03$; as was pointed out earlier, the error bars on our measurement of $\Delta H$ are particularly large in the area near the orthorhombic–tetragonal phase transition.

It is quite reasonable that the transition is of $\lambda$-type, as Jorgensen et al.[9] have shown with *in situ* neutron diffraction that the transition is an order-disorder transition concerning the basal plane oxygen atoms. $\lambda$-type transitions are transitions in which the free energy function changes continuously throughout the transition, but in which the heat capacity exhibits a cusp-like peak at the transition. One can show from an Ehrenfest-type argument that $\Delta H_O$ undergoes a functionally similar change.

Since the transition is of an order higher than 1, the free energy curves are all continuous at the transition point: i.e., $\Delta G=\Delta H=0$ (note also that $\Delta S=0$). Taking temperature, pressure and number of moles of components (O, Y, Ba and Cu) as theindependent variables and differentiating $\Delta H=0$ with respect to T and $n_O$ at constant P and $n_j$ along the transition line, one gets:

# Excess Enthalpy vs. Oxygen Content
## in $YBa_2Cu_3O_{6+\delta}$
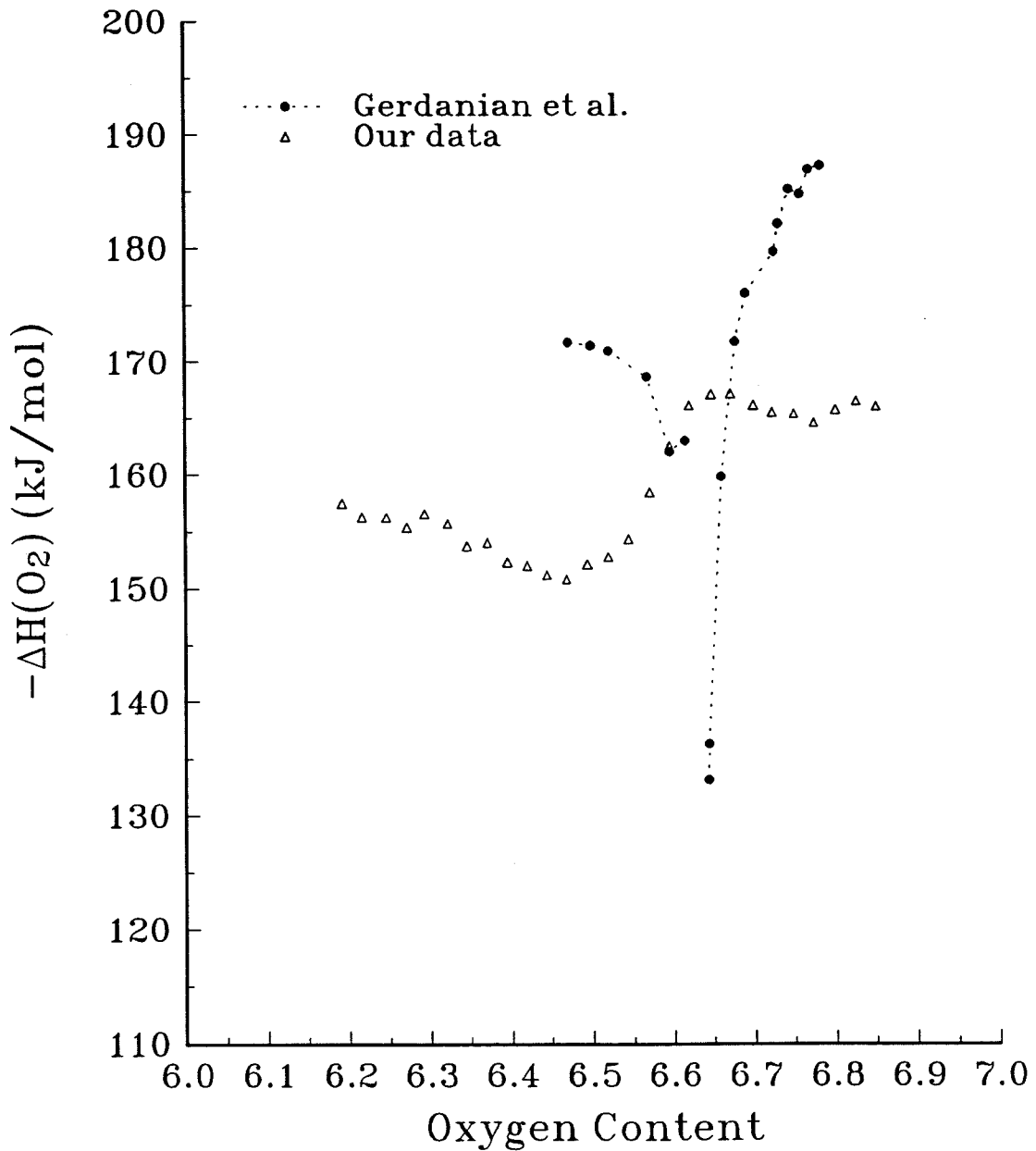


Figure 2.8– A comparison of excess enthalpy versus oxygen content, as taken from our experiments and data from Gerdanian et al.

$$\Delta\left(\frac{\partial H}{\partial T}\right)_{P,n_j} + \frac{dn_O}{dT} \cdot \Delta\left(\frac{\partial H}{\partial n_O}\right)_{T,P,n_j} = 0. \qquad \text{(II.9)}$$

$dT/dn_O$ is proportional to the slope of the orthorhombic-tetragonal transition line in the T-$\delta$ graph and is not 0 or $\infty$. The first term in the equation is just $\Delta C_P$ and the second term is $\Delta(\Delta H_O)$, thus,

$$\Delta C_P + \frac{dn_O}{dT} \cdot \Delta(\Delta H_o) = 0. \qquad \text{(II.10)}$$

Equation (II.10) implies that the discontinuity in $\Delta H_O$ must be of the same $\lambda$–type as the discontinuity in the heat capacity at constant pressure, $C_P$. Differentiation of the equations $\Delta S=0$ and $\Delta G=0$ with respect to T and $n_O$ at constant P and $n_j$ gives:

$$\frac{\Delta C_P}{T} + \frac{dn_O}{dT} \cdot \Delta(\Delta S_o) = 0$$
$$-\Delta S + \frac{dn_O}{dT} \cdot \Delta(\Delta G_o) = 0. \qquad \text{(II.11)}$$

Thus, $\Delta S_O$ also undergoes a $\lambda$-type transition, but $\Delta G_O$ is continuous.

## II.C    High Temperature X-Ray Diffraction

### II.C.1    The Experimental Setup

In order to verify that the inflections observed in the lower temperature P(c) isotherms were due to the orthorhombic to tetragonal phase transition, high temperature x-ray diffraction (Hi-T XRD) was performed on the powders. The advantage of this technique is that it allows the examination of specific points on the P(c) isotherm *in situ*. Hi-T XRD is not plagued by the uncertainties in oxygen content due to quenching the sample to room temperature.

The high temperature x-ray diffractometer, which is shown in schematic in figure 2.9, is a General Electric $\Theta-2\Theta$ diffractometer with a Buehler hot stage sample chamber. The hot stage is capable of reaching temperatures $\geq 1400°C$ and has a base pressure of $\sim 10^{-7}$ torr. Also, the internal heat shielding of the hot stage, originally made of tungsten, has been replaced by machinable nickel to allow the use of hot oxygen in the chamber. Experiments were run with temperatures in excess of 750°C and 760 torr of oxygen. The samples were heated with one of two heating stages: the original stage was a simple Kanthal™ strip onto which the sample pellet was silver painted and a Chromel-Alumel thermocouple was spot-welded. The second generation stage consisted of a boron-nitride holder with a focussing quartz lamp. The sample in the latter case was silver painted onto a block of machinable nickel which was in turn attached to the boron-nitride holder. A thermocouple sat inside a hole drilled into the center of the nickel block. The second setup was designed and used to ensure that thermal expansion of the Kanthal™ strip was not affecting the d-spacings of Bragg peaks in non-systematic ways. A schematic of the two sample stages is shown in figure 2.10.

The diffractometer is capable of high-resolution scans, with a stepping ratio of
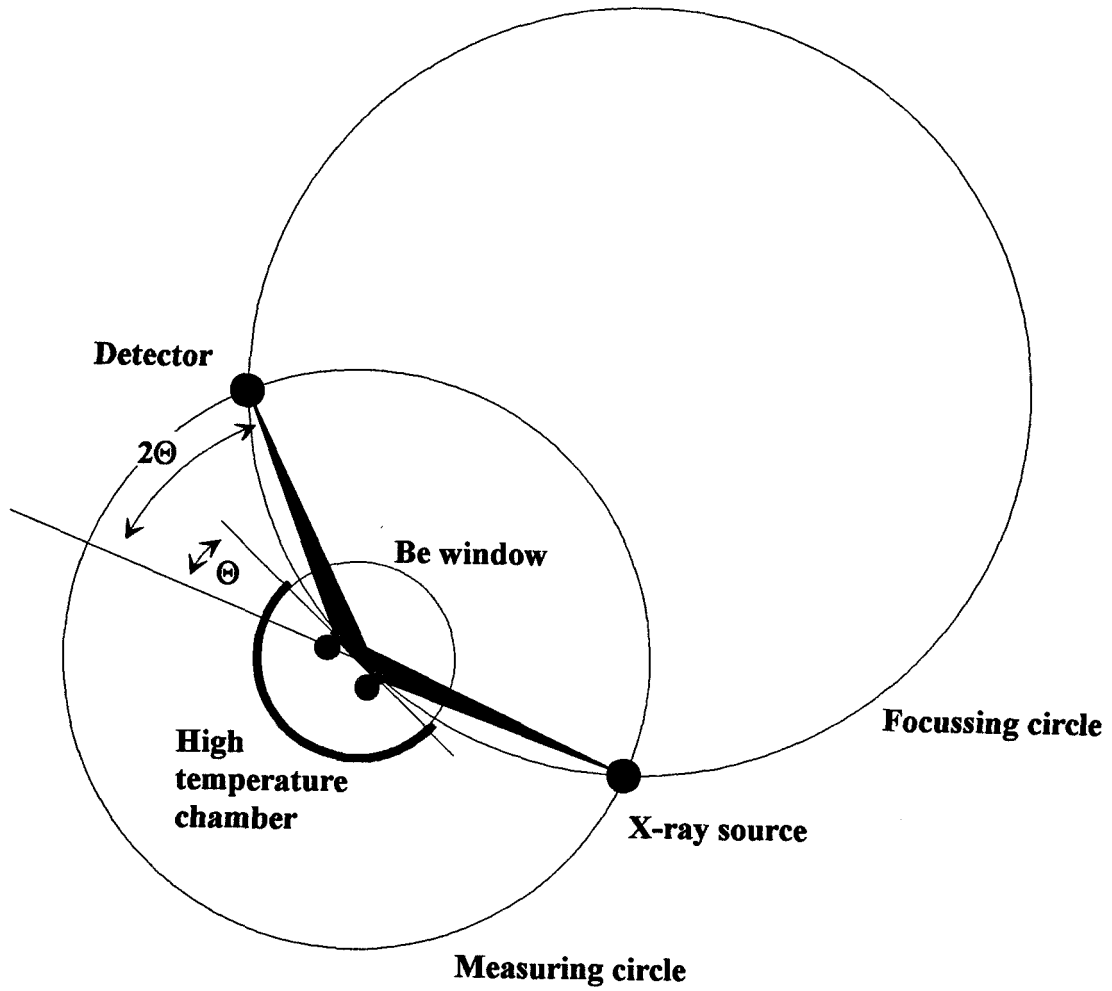
Figure 2.9– A schematic of the high-temperature x-ray diffractometer.

sample pellet
(silver-painted onto holder)

Kanthal heating stage

Chromel-Alumel thermocouple
(spot-welded onto holder)

sample

Nickel block

Boron-Nitride stage

Chromel-Alumel thermocouple
(inserted in hole)

focussing quartz lamp
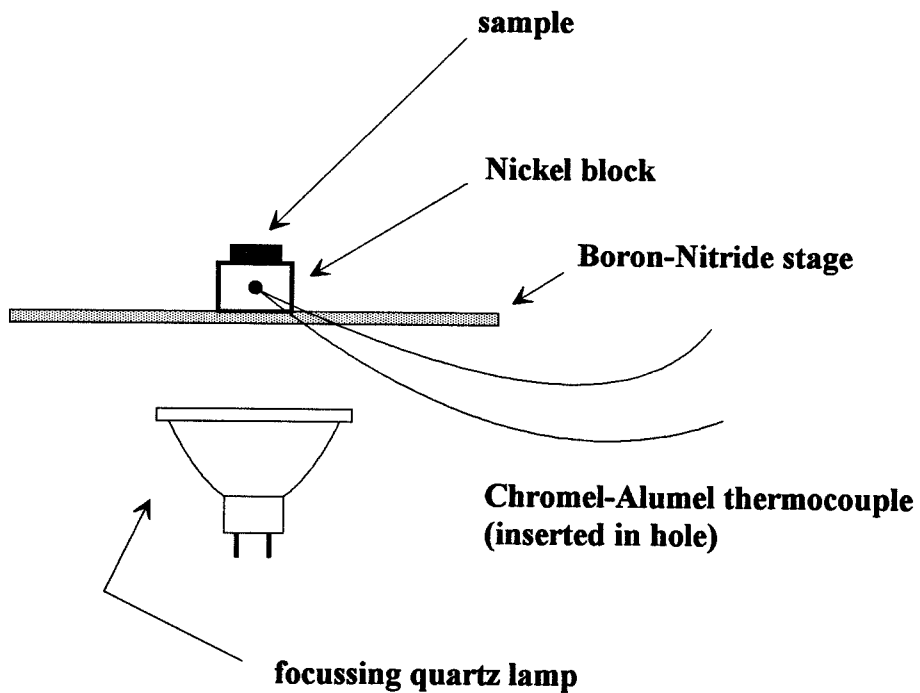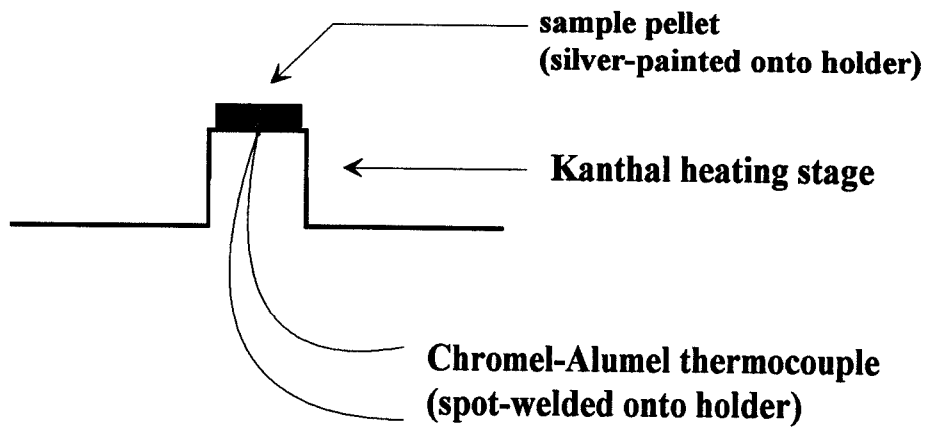
Figure 2.10– Schematics of the two types of sample stages used. The top is a Kanthal™ strip onto which the sample was attached with silver paint. The bottom used a focussing quartz lamp to heat a nickel block onto which the sample was placed.

30,000 steps per degree in 2Θ. Computer control of the stepping motor and data transfer was done serially through a Whiting box. A Seifert Corporation copper Kα x-ray tube was used at a takeoff angle of 7°. An EDS detector was used to detect the scattered x-rays. The detector's superior energy resolution (~185eV) obviated the need for a Kβ radiation filter (such as a Ni filter). The detector was not, however, able to resolve the splitting between Kα1 and Kα2 at approximately 50eV (for Cu radiation).

A Kα2 stripping routine was thus used to remove the contribution from the raw data. The algorithm employed is a modification of the standard Rachinger correction technique; the number of steps between the two overlapping α1 and α2 peaks is allowed to vary through 2Θ in such a manner as to make the distance between the peaks in two theta divided by the number of steps between the two peaks equal to the actual step size of the scan ($\Delta 2\Theta$/nsteps ~ scan stepsize). This minimizes the high angle noise so common to Rachinger-type corrections.(see Appendix A for a detailed description).

The sample chamber was evacuated with a Balzer's turbomolecular pump which was backed by a 1.6L Leybold-Heraeus mechanical pump; pressure was monitored by Balzers cold cathode gauges and pirani gauges. The cold cathode gauges were periodically checked with a hot filament gauge on a different UHV system to ensure that they had not drifted beyond acceptable limits. A variable rate leak valve allowed precise control of the total pressure of oxygen in the chamber. Vibrations transmitted by the mechanical pump to the system were reduced by using bellows between the turbo pump and the x-ray sample chamber. Appendix C contains additional details of the experimental setup.

## II.C.2    Experimental Data and Discussion

### *II.C.2.a        Location of the Orthorhombic-Tetragonal Phase Line*

Shown in figure 2.11 is the P(c) isotherm for 500°C. The corresponding Hi-T

XRD patterns are shown in the expanded windows. The patterns were taken from a

powder sample at constant temperature; during the experiment, only the partial pressure

of oxygen gas in the chamber was varied. The boundary between orthorhombic and

tetragonal phases can be clearly defined and has been plotted in figure 2.4 on a graph of

$\Delta\mu_O^{ref} + \mu_O^E$ vs $\delta$. It is shown again in figure 2.12. In these experiments, the boundary

between orthorhombic and tetragonal phases was defined as the point at which the

orthorhombic plitting of the peaks could no longer be distinguished. With the setup used,

this corresponded to a difference between the a-axis and b-axis of the unit cell of no more

than (b-a)<0.003Å. This type of experiment was repeated for many partial pressures of

oxygen and temperatures in order to define the phase line between the orthorhombic and

tetragonal phases shown in the figure. The plot shown in figure 2.5 also displays this

phase line in the $\mu$ vs. T plane.

### *II.C.2.b        Dependence of Lattice Parameters on Oxygen Content*

With the data taken from the pressure-concentration isotherms and

thermogravimetric analysis, it was possible to execute constant stoichiometry cooling of

powder samples in the high temperature diffractometer and determine the lattice

parameters for known oxygen contents. This technique allowed fast equilibration at high

temperature for a particular value of $\delta$ and subsequent cool down without changing the

Figure 2.11– The 500°C P(c) isotherm. The corresponding *in situ* x-ray diffraction patterns are shown.

# Orthorhombic–Tetragonal Phase Line
## in $YBa_2Cu_3O_{6+\delta}$
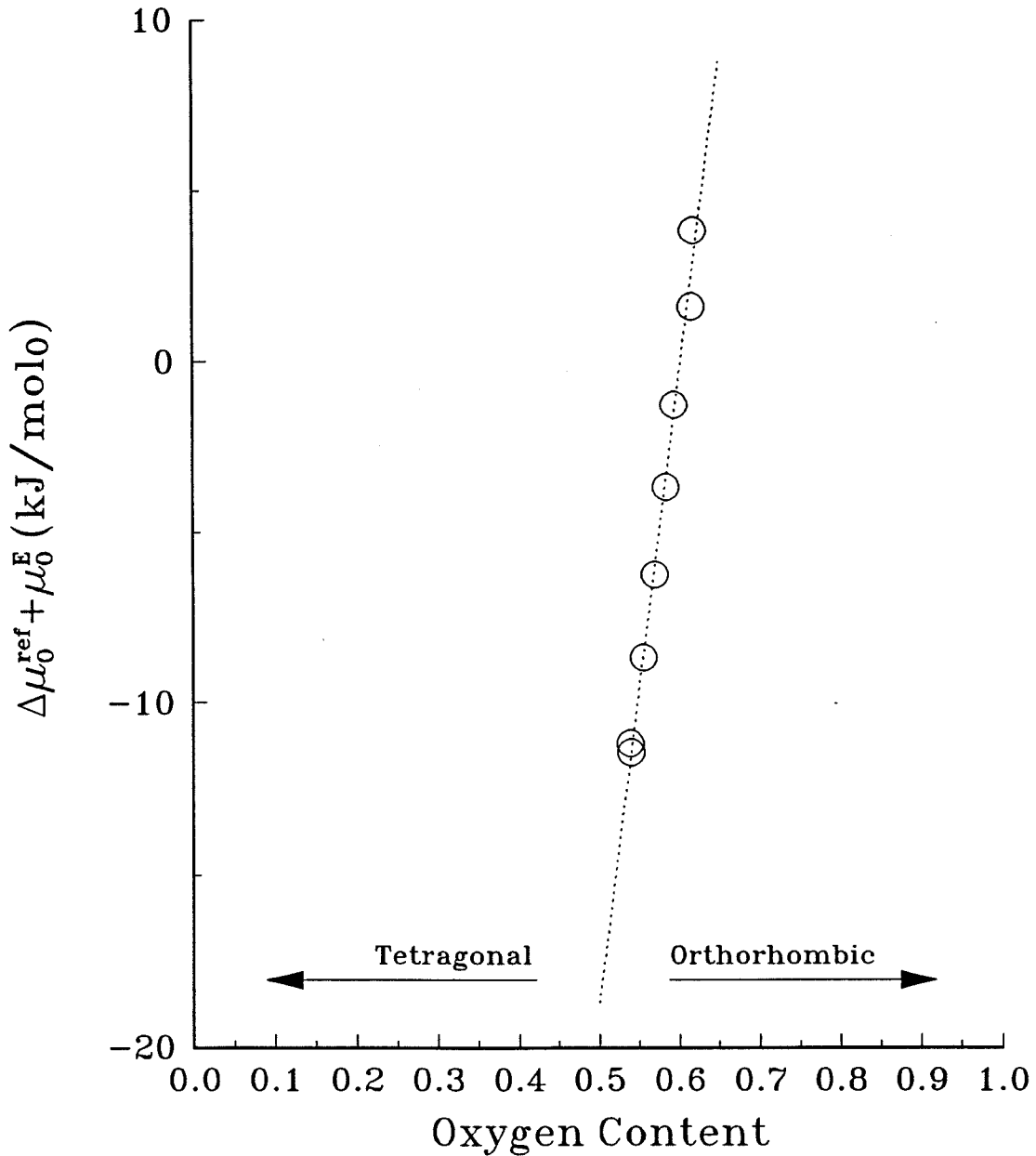


Figure 2.12– Plot of excess chemical potential as a function of oxygen content showing the orthorhombic-tetragonal phase line.

oxygen content in the sample. Other experiments of this type were usually cooled in a constant partial pressure of oxygen (constant chemical potential) which cannot guarantee equilibrium ordering.[10,11,12] As can be seen from the results shown in figure 2.13, there seem to be two distinguishable relations between the a, b, and c lattice parameters within the orthorhombic phase region. The region above about $\delta\sim0.8$ has unit cell parameters $a<b=c/3$. The region between $\delta\sim0.35$ and $\delta\sim0.8$ has unit cell parameters $a<b<c/3$. Of course in the tetragonal region, $a=b$ and both are less than $c/3$. Recall that the plot of $T_C$ vs. oxygen content showed a plateau centered around $\delta\sim0.6$ (figure 1.4). This set of experiments, with its constant stoichiometry cooling, strongly suggests that there is a direct correlation between the superconducting transition temperature and the equilibrium crystal structure. Unfortunately, as mentioned before, x-ray diffraction cannot determine whether or not this second orthorhombic region corresponds directly to the Ortho II phase seen in TEM[13,14] and predicted by various computer models.[15,16]

### II.C.2.c     *Thermal Expansion of the Tetragonal Phase*

After annealing the sample in high vacuum for several hours at temperatures above the orthorhombic–tetragonal transition, the sample was cooled and x-ray diffraction was done at various temperatures to find the thermal expansion of the tetragonal phase. The results are shown in figure 2.14.

# Lattice Parameter vs. Oxygen Content
## in $YBa_2Cu_3O_{6+\delta}$
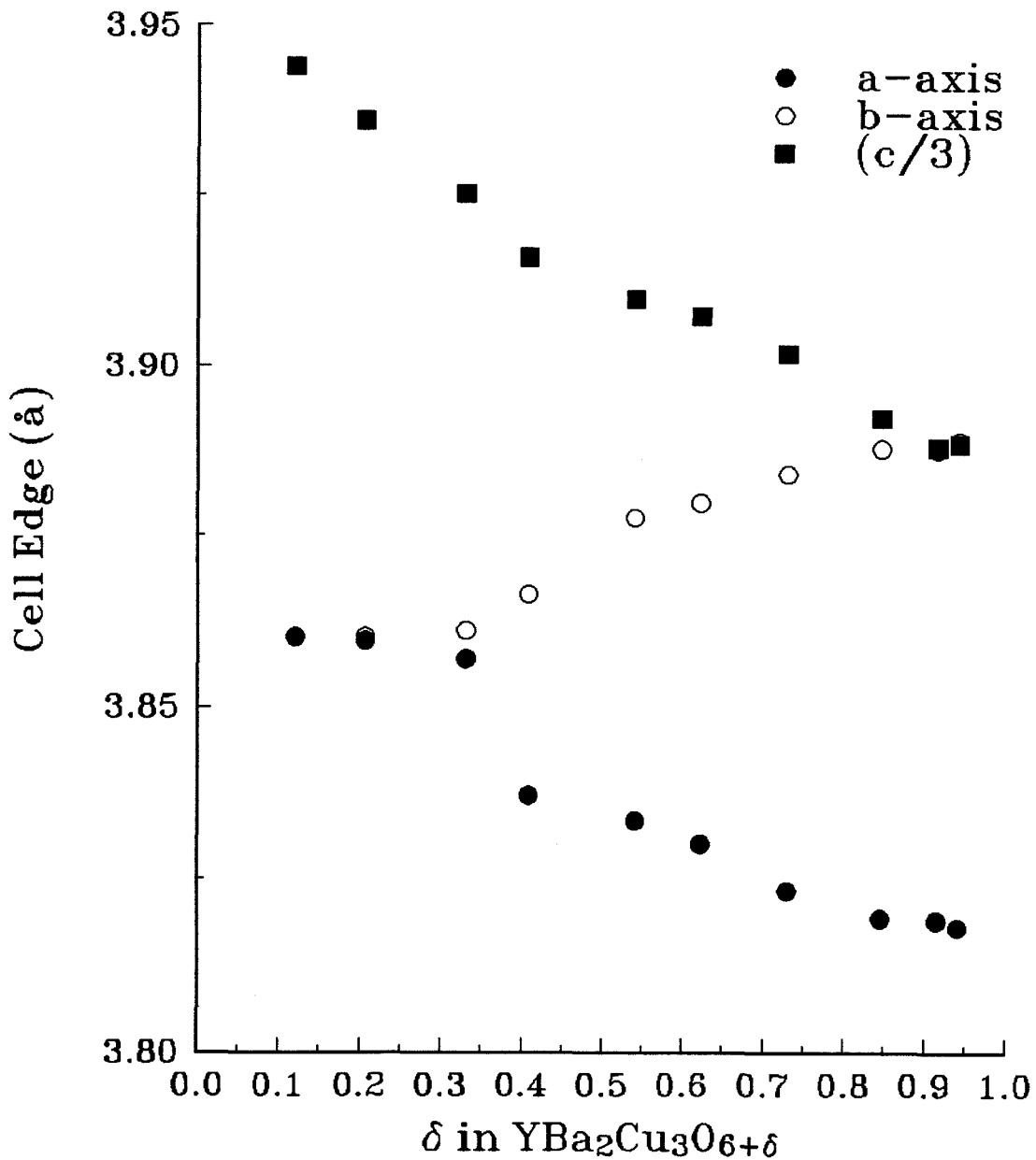


Figure 2.13– Room temperature lattice parameters as a function of oxygen content after constant stoichiometry cooling of $YBa_2Cu_3O_{6+\delta}$ powder. Note the three regions: a<b<c/3, a<b<c/3, and a<b=c/3.

# Thermal Expansion of Tetragonal YBa$_2$Cu$_3$O$_{6+\delta}$
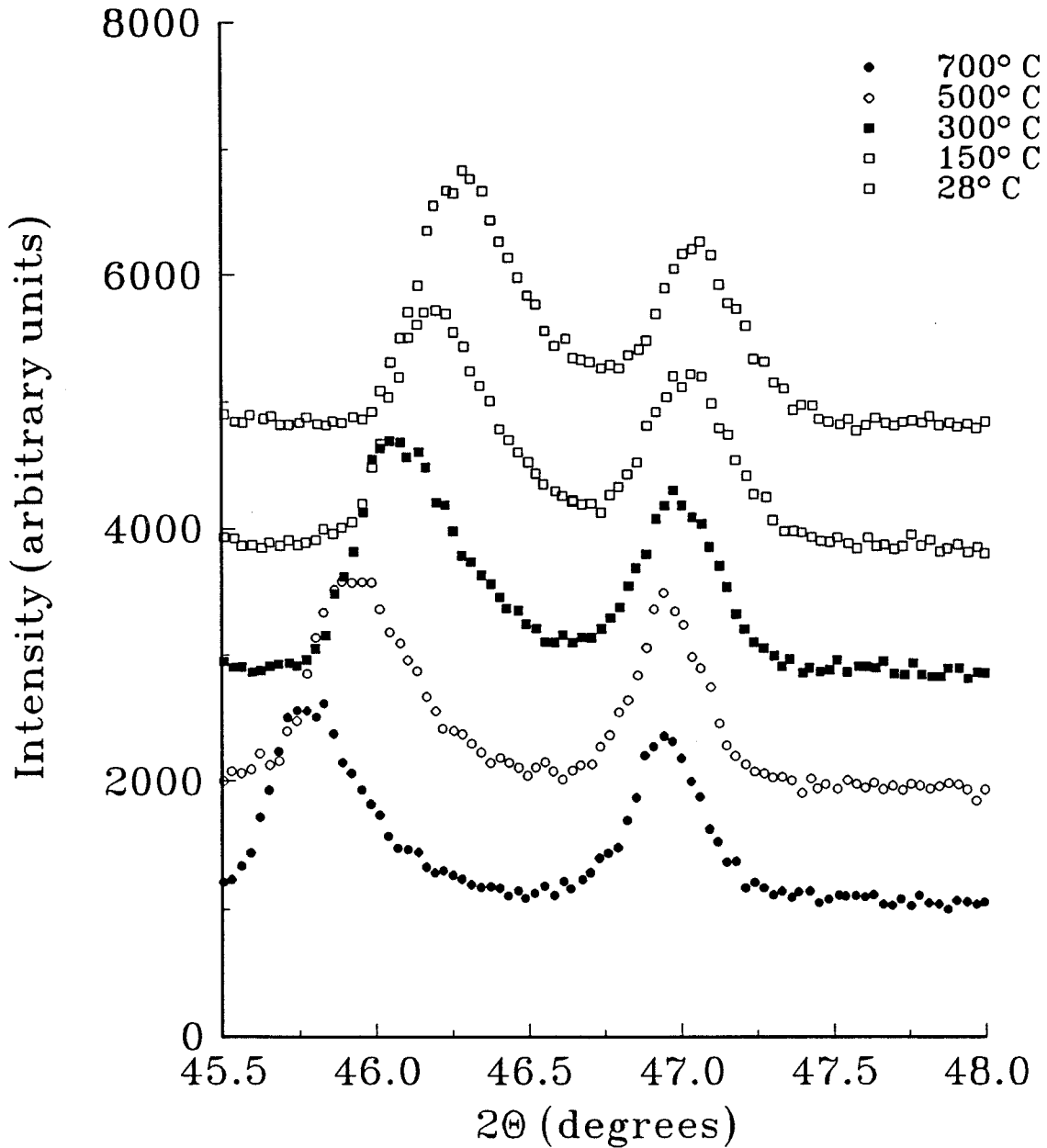


Figure 2.14– Thermal expansion coefficient data for tetragonal YBa$_2$Cu$_3$O$_6$.

## II.D    Models of the Transition

### II.D.1    The Anisotropic Two-Dimensional Ising Model

There have been many attempts to model the orthorhombic-tetragonal phase transition[17,18,19,20,21,22,23] which, as might be expected, have met with varying degrees of success. Among the most complicated and involved calculations were those of Aukrust, Novotny, Rikvold and Landau,[24] who performed large scale Monte Carlo and transfer-matrix studies on anisotropic lattice gas models with up to 8 sublattices. Berera and deFontaine[25] and Bell[26] used cluster variational methods in their models, which included up to fourth nearest neighbor interactions. However, the qualitative features of this transition can be described by a much simpler scheme; an anisotropic 2D Ising model in equilibrium with oxygen gas. Although the simpler models are satisfactory for predicting the phase boundaries, they fall short on quantitative agreement with experimental values for the various thermodynamic functions of the system. We will begin by examining the results of a simpler model and then consider several modifications to it and compare the predictions to the present results and other published data.

None of the calculations described in this section were done here. Our data was given to Kachaturyan et al.[27] to convert their effective temperature scale to a real one in their calculation of a pseudobinary phase diagram for the oxygen sublattice. This section is a survey of what has been found in simulations of the $YBa_2Cu_3O_{6+\delta}$ order–disorder transition and a comparison to our experimental results.

The work done by Bakker et al.[28] uses a model in which it is assumed that oxygen adsorption and desorption takes place exclusively in the CuO basal planes. They then use a quasi-chemical (or pair) approximation to calculate the free energy of the system. Although this model is too simple to give accurate fits to experimental data, it is a good

starting point for the inclusion of higher order effects.

In the Bakker et al. model, each plane is treated as an independent two-dimensional lattice gas. For the calculations, they define two oxygen sublattices, $\alpha$ and $\beta$, that correspond to the sites O(5) and O(1) in figure 1.1b. A heat of solution for oxygen initially in the molecular state is assumed (E, in electron volts), as is a nearest neighbor repulsion between an oxygen atom on the $\alpha$ sublattice and an oxygen atom on the $\beta$ sublattice (V, in electron volts). Short range order is introduced through the specification of a fractional site occupancy for $\alpha$-$\beta$ oxygen nearest neighbor pairs. If there are N sites available on the combined lattices and $N_{oo}$ is the number of oxygen-oxygen $\alpha$-$\beta$ pairs, then the fractional number of nearest neighbor pair sites occupied is $q = (N_{oo}/4N)$. A graphical representation of this can be found in figure 2.15.

The total oxygen concentration in the basal CuO plane, c, and the order parameter, s, can then be written as functions of the fractional site occupancies for each of the sublattices, $c_{\alpha}$ and $c_{\beta}$:

$$c = \frac{c_{\alpha} + c_{\beta}}{2} \quad \text{and} \quad s = \frac{\left(c_{\alpha} - c_{\beta}\right)}{c_{\alpha} + c_{\beta}} \tag{II.12}$$

or

$$c_{\alpha} = c(1 - s) \quad \text{and} \quad c_{\beta} = c(1 + s). \tag{II.13}$$

Minimizing the free energy with respect to the two parameters s and q gives:[29]

$$\ln\left[\frac{c(1+s)-q}{c(1-s)-q}\right] = \frac{3}{4}\ln\left[\frac{(1+s)\left[1-c(1-s)\right]}{\left(1-s\left[1-c(1+s)\right]\right)}\right]$$

$$\frac{V}{kT} = \ln\left[\frac{\left[c(1+s)-q\right]\left[c(1-s)-q\right]}{q(1-2c+q)}\right]. \tag{II.14}$$
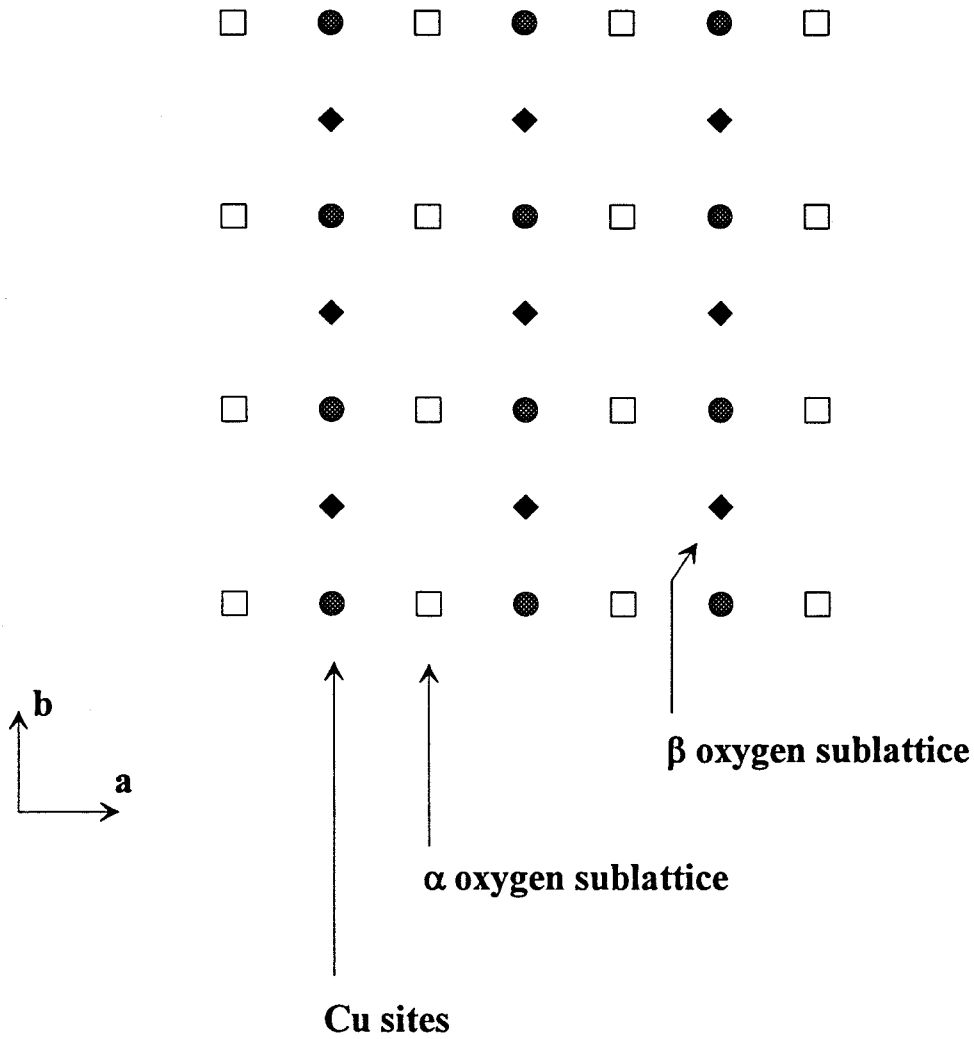
Figure 2.15– A schematic of the model used to describe the orthorhombic-tetragonal phase transition that occurs on the basal CuO plane.

Equating the chemical potential of an oxygen atom in the lattice gas to that of an oxygen atom in the molecular gas gives:

$$\ln\left\{\left[\frac{1-c(1+s)}{c(1+s)}\right]^3 \cdot \left[\frac{c(1+s)-q}{1-2c+q}\right]^4\right\} = \ln\left\{\frac{p}{p_o\left(1-e^{-\theta/T}\right)}\right\}^{1/2} - \frac{\varepsilon+\frac{1}{2}E_D}{kT}, \text{(II.15)}$$

where $\varepsilon$ is the site energy, $E_D$ is the energy of dissociation for an oxygen molecule (the entire heat of solution for oxygen is then $E=\varepsilon+\frac{1}{2}E_D$), $p_o=3.0401\cdot T^{7/2}$ for oxygen gas and the vibrational temperature for oxygen gas $\theta=2230K$[30]. The two minimization equations and the above equilibrium constraint uniquely determine c, s and q for any given T and P. Algebraic manipulation of these equations as s→0 yields the transition temperature and the interaction potential V;

$$\frac{V}{kT_C} = \ln\left[\frac{16c_c(1-c_c)}{1-4(1-2c_c)^2}\right]. \qquad \text{(II.16)}$$

In figures 2.16a and 2.16b, we see the results of the fit of this model to *in situ* neutron diffraction data of fractional site occupancy as a function of partial pressure of oxygen taken by Jorgensen et al..[31,32] Figure 2.16c shows the fit to data on fractional site occupancy versus temperature in one atmosphere of oxygen from the same experiments. In figure 2.17 is the fit to average overall occupancy (i.e., δ) as taken from other published data.[33,34] The fits are quite good. In figure 2.18 is the calculated orthorhombic-tetragonal phase boundary and data taken from our experiments and other published data.[35,36,37,38]

Figure 2.19 shows the calculated P(c) isotherms using this model. Clearly, the calculation shows a much stronger pressure dependence of the oxygen concentration than

the expermental isotherms. In addition, the sharpness of the kink in the $\delta$=0.6 isotherm is not seen. The experimental isotherms seem to show a stronger dependence at lower pressures, but the kinetics involved with oxygen uptake are so slow as to prevent good measurements.

# Site Occupancy vs. Oxygen Partial Pressure
## in $YBa_2Cu_3O_{6+\delta}$
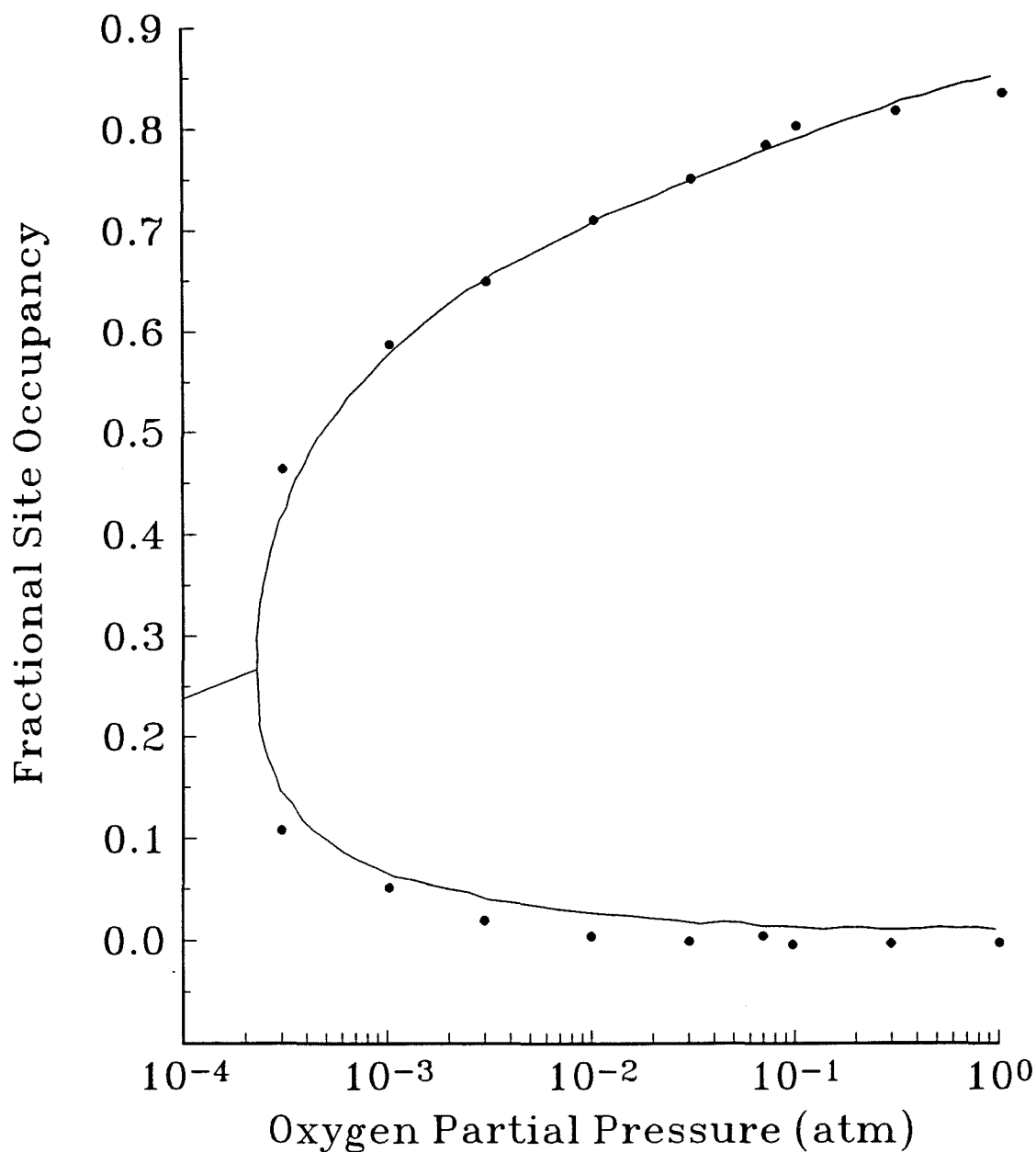


Figure 2.16a– Data from Jorgensen et al. The graph shows fractional O(1) site occupancy as a function of oxygen partial pressure at 440°C.

## Site Occupancy vs. Oxygen Partial Pressure
### in $YBa_2Cu_3O_{6+\delta}$
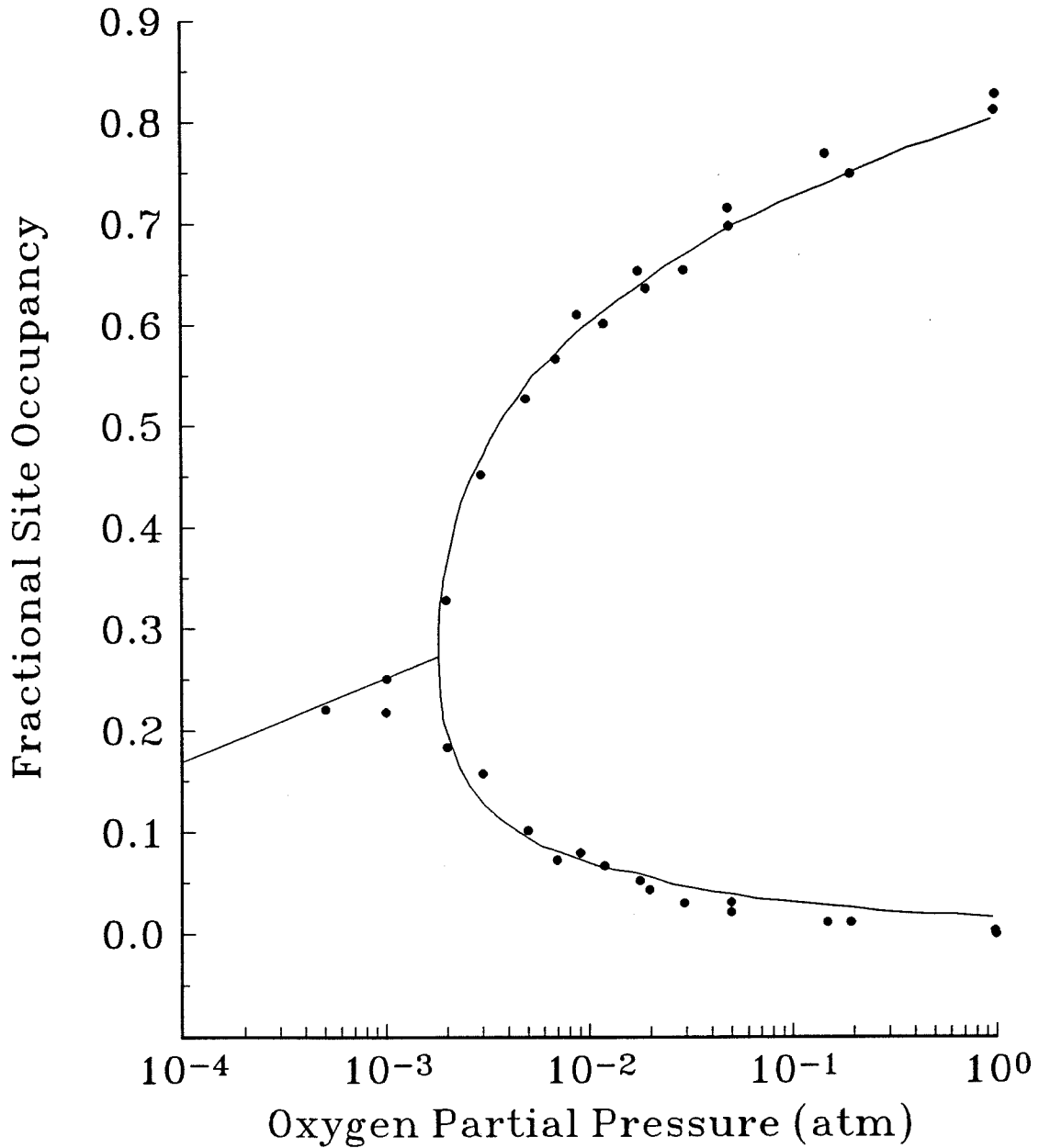
Figure 2.16b– Data from Jorgensen et al. The graph shows O(1) site occupancy as a function of oxygen partial pressure at 490°C.
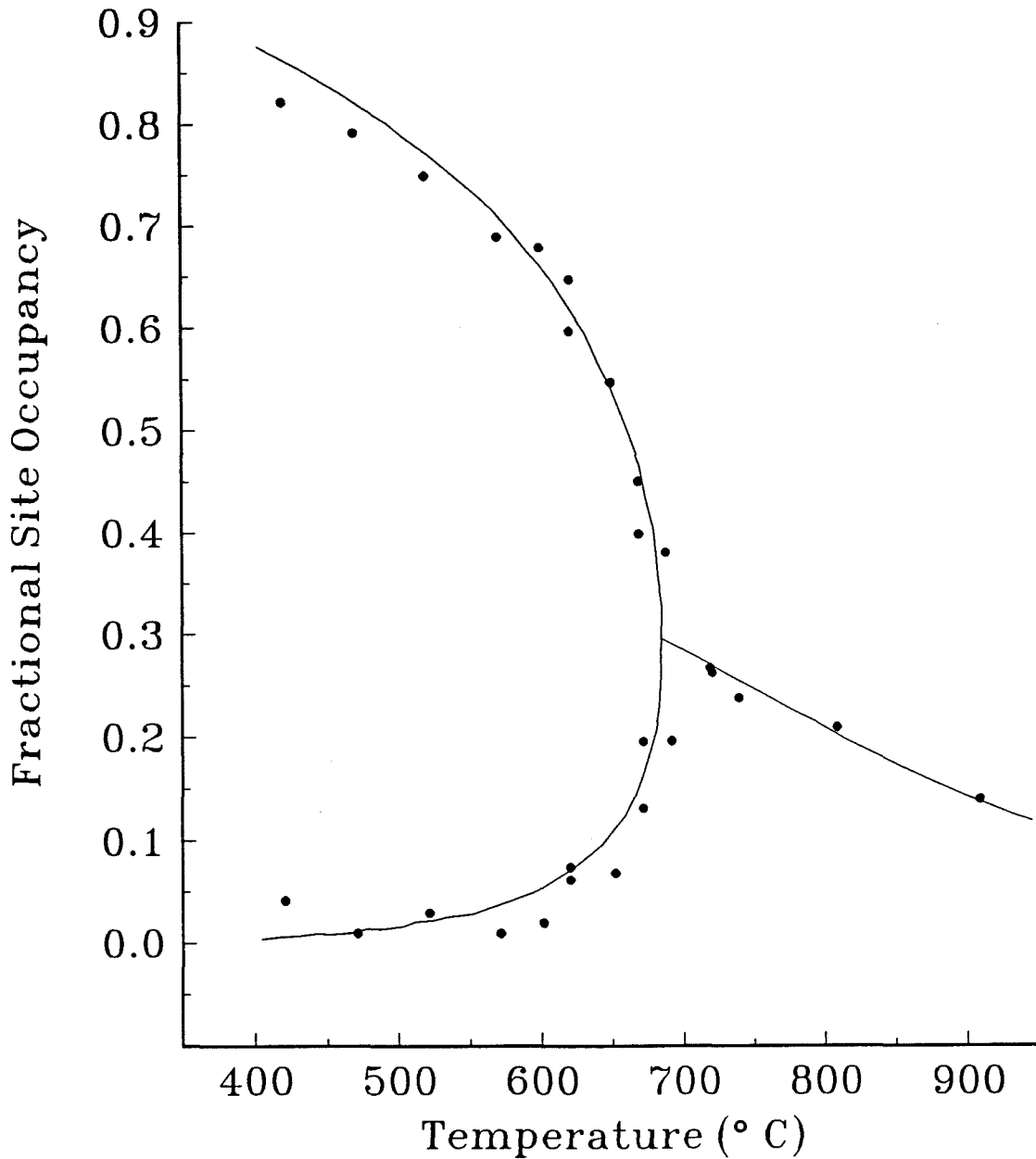
Figure 2.16c– Data from Jorgensen et al. The graph shows O(1) site occupancy as a function of temperature in 1013 bar of oxygen.

# Average Occupancy of Oxygen in CuO−planes

## in $YBa_2Cu_3O_{6+\delta}$
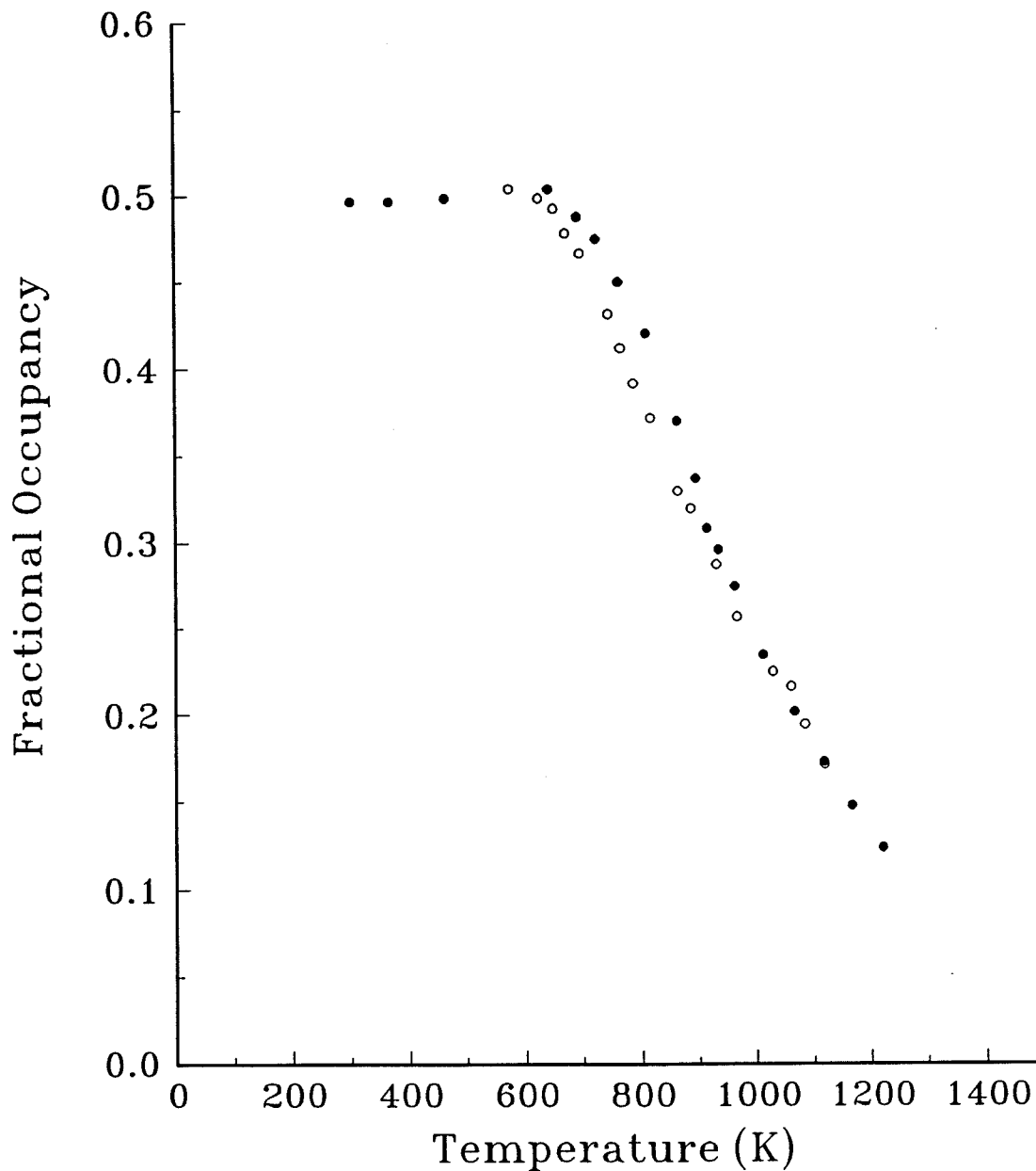


Figure 2.17– Average occupancy of oxygen in basal CuO plane as measured by TGA and P(c) isotherms.

# Orthorhombic–Tetragonal Phase Line
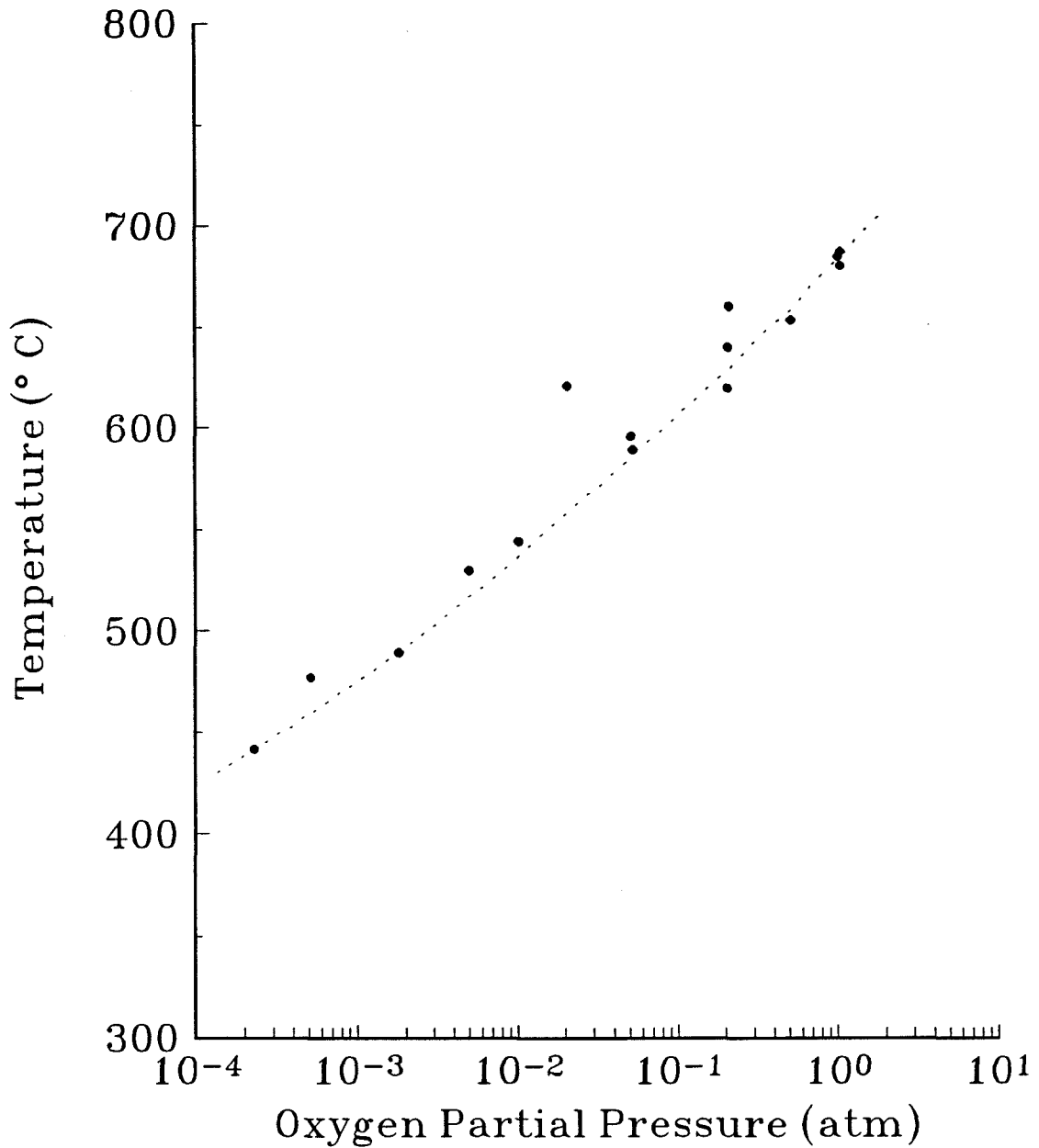
## in $YBa_2Cu_3O_{6+\delta}$



Figure 2.18– Orthorhombic-tetragonal phase line in the T–μ plane.
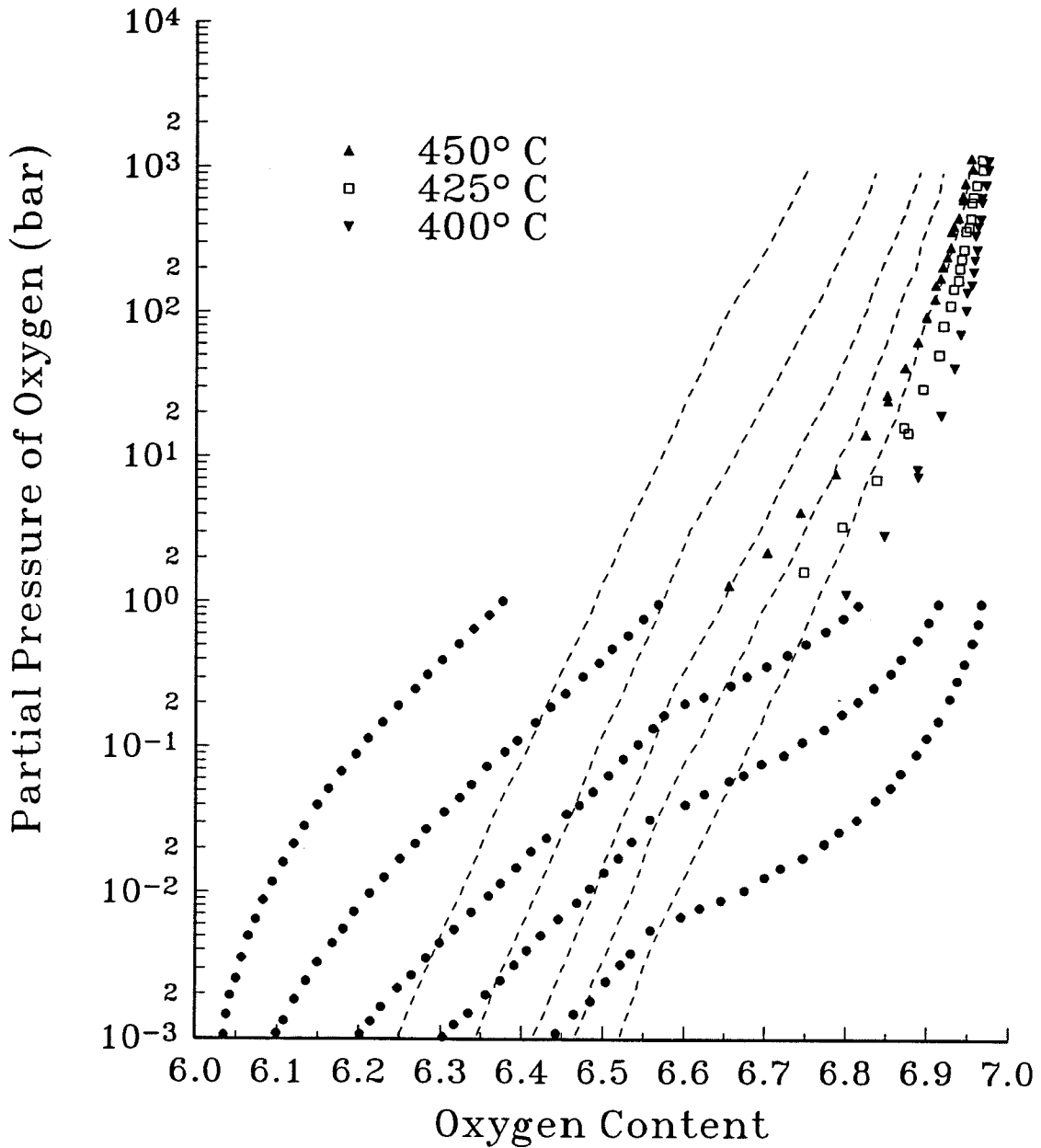
Figure 2.19– Calculated isotherms using the Bakker et al. model (dots) and the Salomons et al. model (dashed line). Experimentally measured data is shown for comparison.

## II.D.2    Concentration Dependence of the Heat of Solution of Oxygen

The first modification we consider to this model allows for a concentration dependence to the heat of solution, E. The dotted lines in figure 2.19 show P(c) isotherms calculated from the model, but modified to include a concentration dependent heat of solution [E=E(c)]. This model was proposed by Salomons et al.,[39] and shows considerable improvement over the Bakker model. The calculations done by Salomons used a linear functional dependence for the heat of solution.

The assumption of a concentration dependent heat of solution is not an arbitrary injection of complexity to the problem; for metal-hydrides, it is well-known that almost all hydrogen absorbing metals and alloys exhibit a strong concentration dependence in their heat of hydrogen solution. For example, Feenstra et al.[40,41] showed that for metal-hydrides with a low density of states at the Fermi energy, there is a large, positive electronic contribution to the heat of solution which is proportional to the hydrogen concentration. Both experiments[42,43] and calculations[44,45] suggest a low density of states at the Fermi energy in $YBa_2Cu_3O_{6+\delta}$. This led Salomons et al. to the assumption that the concentration dependence of the heat of solution is linear. This model seems to do the best job of fitting the experimentally observed isotherms. However, it has the drawback of not being able to reproduce the Ortho II phase, which will be described in the next section.

## II.D.3    Anisotropic Next Nearest Neighbor Interactions - the Ortho II Phase

The orthorhombic structure has atoms occupying the $\beta$ sublattice which result in the contraction of the basal plane along the a-axis. This suggests that an attractive next

nearest neighbor interaction might be justified in the model. Since the b-axis remains larger than the a-axis in the orthorhombic phase, the attractive interaction along the b-axis (which is mediated by a Cu atom) should be smaller in amplitude than the next nearest neighbor interaction potential along the a-axis. This is the plausibility argument for the model by Berera and deFontaine[46] in which they use a two-dimensional Ising model with isotropic nearest neighbor interactions and anisotropic next nearest neighbor interactions.

Beyond the simple plausibility argument given above lies a more substantial justification for the inclusion of these longer range interactions. It was found by Cava et al.[47] that samples carefully prepared by a gettering technique with oxygen contents in the range $\delta=0.4$-0.6 all seemed to have a superconducting transition temperature, $T_C$, of around 60K. The plot shown earlier of $T_C$ versus oxygen content (figure 1.4) measured by Cava et al. confirmed a plateau at 60K. The transition temperature was observed to decrease slightly from 90K for $0<\delta<0.2$, and then drop more rapidly to a constant plateau near 60K for $0.3<\delta<0.45$, followed by a drop to 0K (i.e., the material did not exhibit any signs of superconductivity) near the orthorhombic-tetragonal transition at $\delta\approx0.45$. The exact point at which the samples no longer superconduct is difficult to determine because the samples made in the range of interest exhibit broad transitions characteristic of inhomogeneity or two-phase behavior. The 60K superconducting samples were shown by electron diffraction to be orthorhombic, but with a doubled cell structure in the basal plane.[48,49] The structure has been dubbed the "Ortho II" phase. Such structure was not seen in x-ray diffraction experiments because x-ray scattering factors are proportional to the square of the atomic masses and therefore, in $YBa_2Cu_3O_{6+\delta}$, the scattering from one oxygen atom accounts for less than 0.1% of the total scattering from a polycrystalline sample. Figure 2.20 illustrates this ordering, which cannot be reproduced in the original nearest-neighbor-only model (the range of the interactions in the nearest-neighbor-only model do not extend far enough to order second nearest-neighbors). Actually, it will be shown that the inclusion of next nearest neighbor interactions does not improve agreement
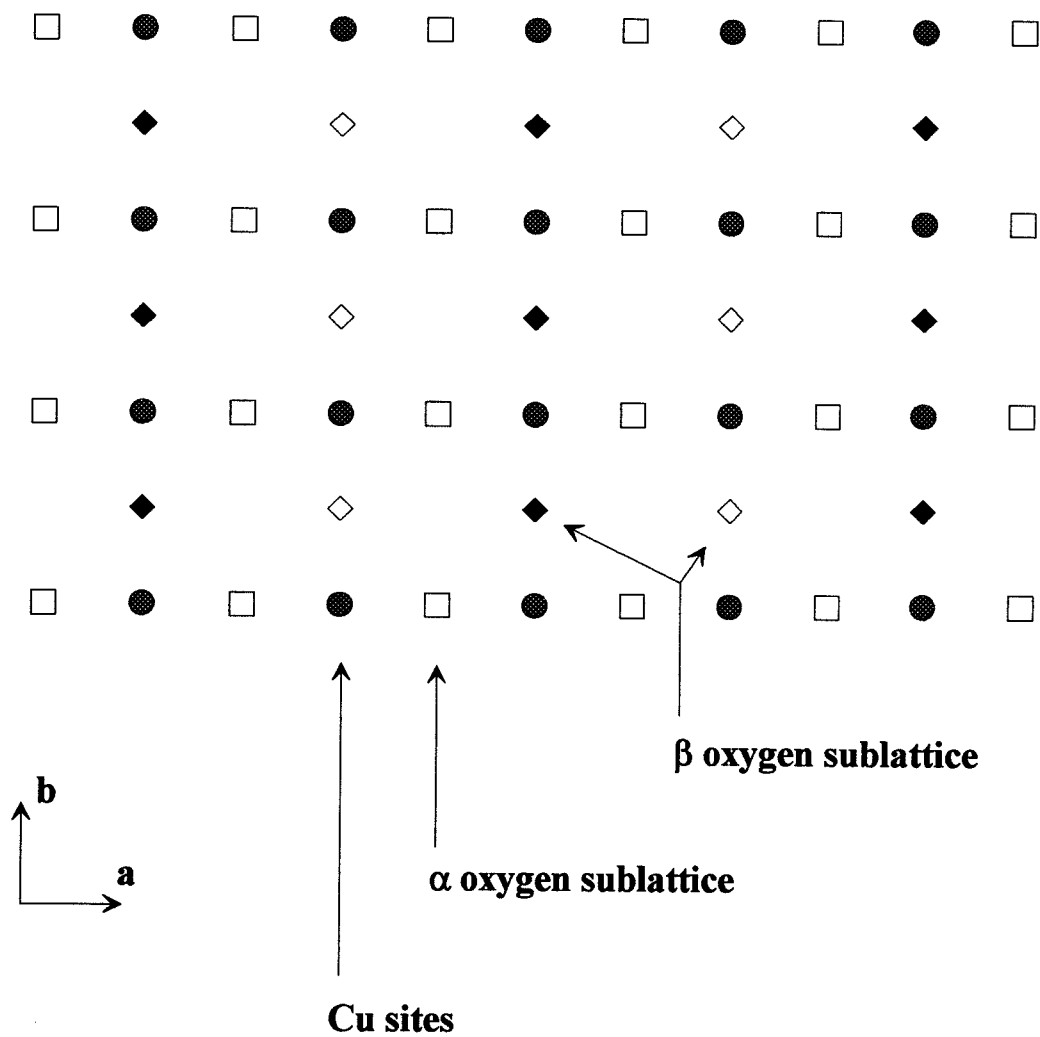
Figure 2.20– The Ortho II phase, in which every other chain of O(1) sites is occupied.

with experimental measurements of thermodynamic quantities, but that such interactions do allow the prediction of the Ortho II phase.

Berera and deFontaine have used cluster variation methods to compare their model of the orthorhombic–tetragonal transition with experimental data and Aukrust, Novotny, Rikvold and Landau used Monte Carlo and transfer matrix methods to study their model of the transition.[50,51] Other groups have also used cluster variation methods to study the transition,[52,53,54] and although their implementations differ slightly from one and other, they all agree on the sign of the effective oxygen-oxygen pair interactions: a repulsive nearest-neighbor interaction, $V_1$, an attractive next nearest neighbor interaction that couples O(1) sites along the CuO chains mediated by copper atoms, $V_2$, and an effective next nearest neighbor repulsion between O(5) sites normal to the chains, $V_3$. As stated before, this particular choice of interactions successfully predicts the orthorhombic-tetragonal transition and gives rise to an Ortho II phase, in agreement with observations made by transmission electron microscopy.

The thermodynamic properties of this system were explored by Monte Carlo simulations by Pörschke et al.[55] Calculations were done on a 64x64 square lattice with periodic boundary conditions in the Grand Canonical Ensemble. Figure 2.21 shows their results for the simulation of the configurational excess chemical potential,

$$\mu_O^{E,c} = \mu_o^c - RT\ln\left(\frac{2-\delta}{\delta}\right), \tag{II.17}$$

from the lattice gas model in comparision with our measured excess chemical oxygen potential. The superscript "c" points out that these are calculated quantities. Despite the fact that the model predicts the phase transition at concentrations which are in accordance with experimental findings, there are severe quantitative differences between the actual and calculated chemical potentials. Notice that in the orthorhombic phase, the calculated $\mu_O^{E,c}$ varies too slowly with concentration $\delta$. Pörschke et al. found no combination of

interaction parameters that was able to reduce the discrepancy between their measured data and the model.[56] A comparison of the calculated partial molar configurational energy contribution to $\Delta H_O$, $U_O^c = \dfrac{dU^c}{d\delta}$, shows that the drop in actual partial enthalpy of about 5.5 kJ/mol(O) across the transition cannot be accounted for by configurational mechanisms. Figure 2.22 compares the calculated partial molar configurational energy and the actual drop in partial enthalpy across the transition. Similar results are shown in figure 2.23 for the calculated partial entropy, $S_O^c = \left(U_O^c - \mu_O^c\right)/T$. Again, the measured partial entropy shows a much stronger decrease in the orthorhombic region. This might be an indication that during the transition, entropic degrees of freedom, which are not contained in the lattice gas model, are frozen out. Furthermore, Pörschke et al. point out that aside from questioning the validity of using two-body interaction energies (albeit *effective* pair interactions), there are also potential problems due to the fact that three-dimensional phononic and electronic contributions to the thermodynamic quantities are not taken into account in a two-dimensional lattice gas model. Finally, they point out that the assumption of concentration independent effective pair interactions is not necessarily reasonable because the system undergoes a severe structural change across the transition which should be reflected in the electronic structure of the system. In fact, as shown above, allowance for the concentration dependence seems to help greatly in the successful modeling of pressure-concentration isotherms.
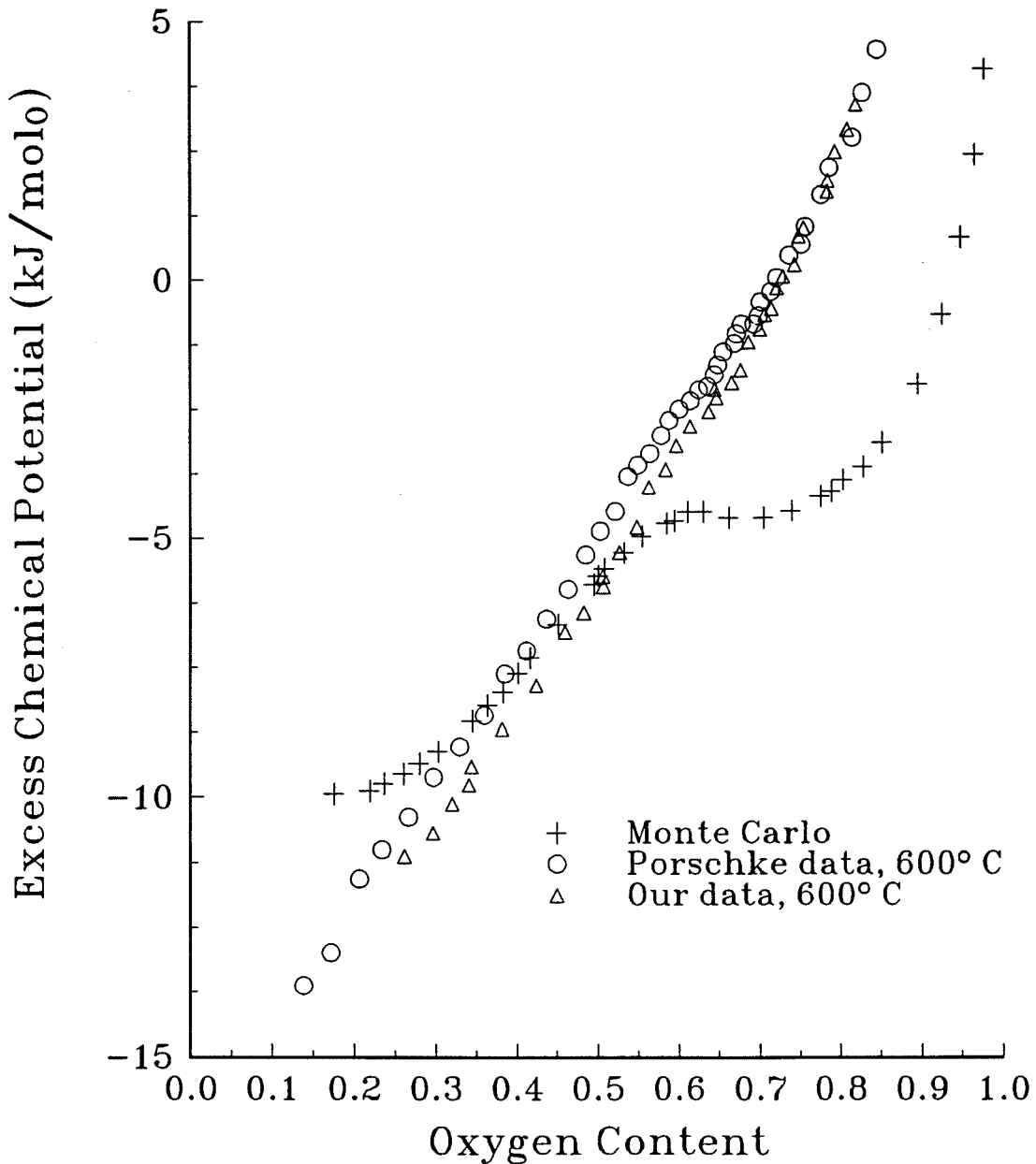
Figure 2.21– Comparison of calculated excess chemical potential with experimentally measured values. Note that the calculated points show a much stronger dependence on oxygen content.

# Calculated Configurational Partial Energy
## in $YBa_2Cu_3O_{6+\delta}$
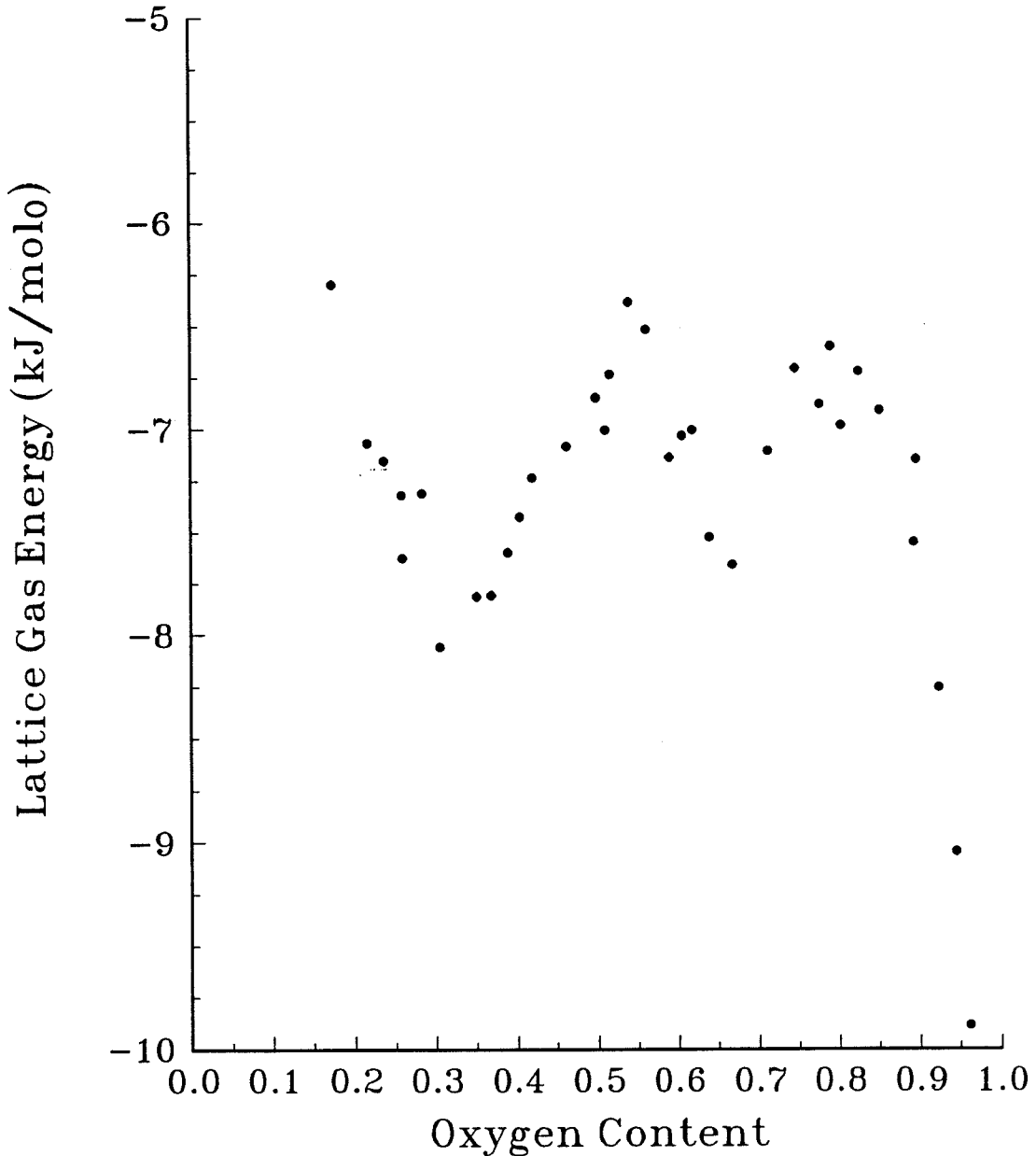


Figure 2.22– Calculated contribution of configurational energy to the excess enthalpy. Recall that the excess enthalpy drops 5.5 kJ/mol(O) across the transition (figure 2.12). Configurational mechanisms cannot account for this drop.

# Calculated Configurational Partial Entropy

## in $YBa_2Cu_3O_{6+\delta}$
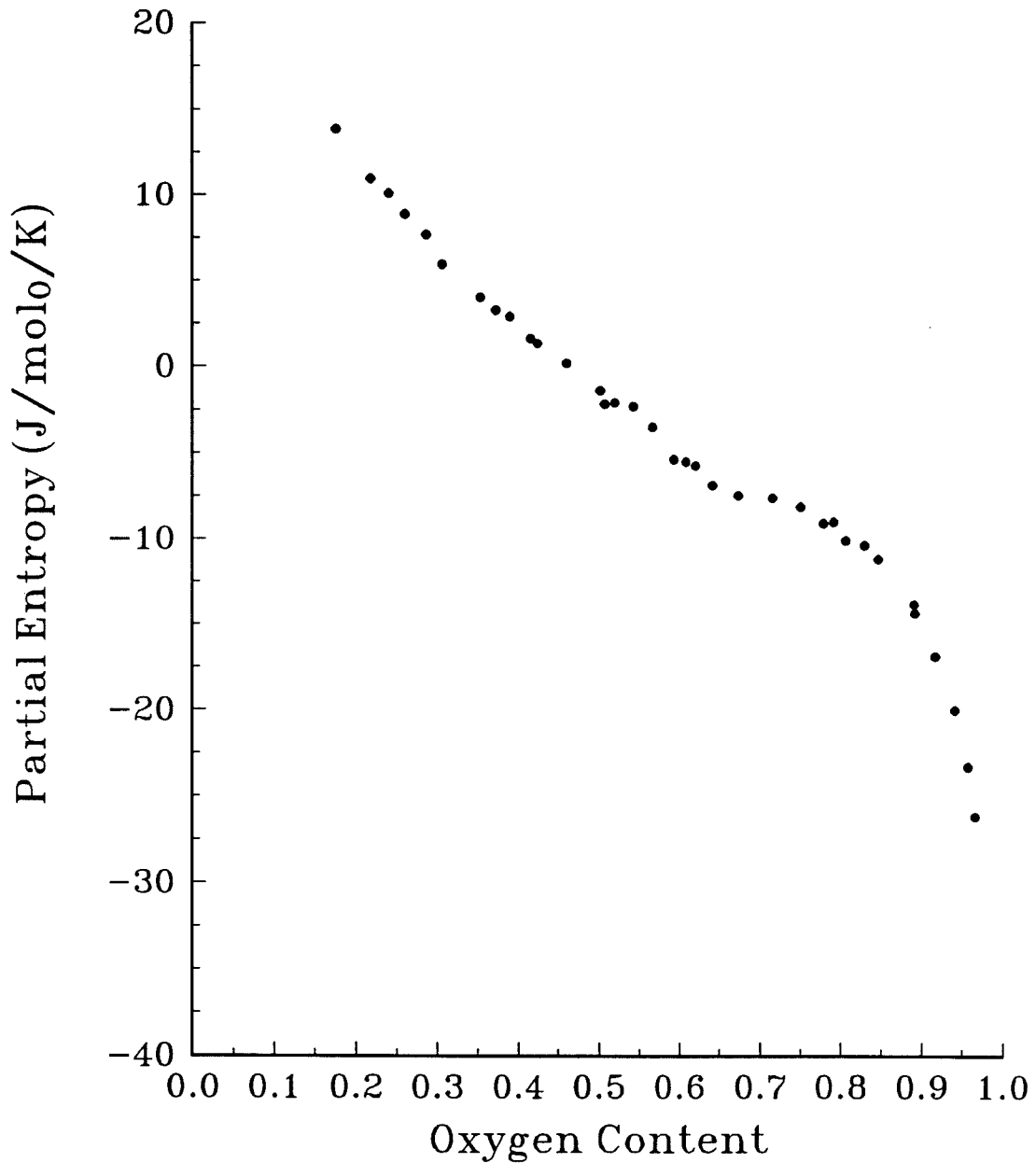


Figure 2.23– Calculated partial entropy. Again, the measured partial entropy shows a much stronger decrease across the O-T transition (figure 2.13).

## II.E    Differential Scanning Calorimetry of the Transition

### II.E.1    Experimental Details and Background

Differential Scanning Calorimetry (DSC) is a thermoanalytical technique for measuring the amount of heat absorbed or released from a reaction. In a DSC such as the Perkin-Elmer DSC-4, there is a sample pan and a reference pan, each of which is provided with its own heater (see figure 2.24a). A "null-balance" principle is employed in which the temperatures of the two pans are controlled. There are two control loops for temperature control: the first loop controls the average temperature so that both the reference and sample pans increase or decrease in temperature at a predetermined rate and are equal to each other. The second loop ensures that if a temperature difference develops between the sample and reference pans (presumably because of endothermic or exothermic reactions that occur in the sample), the power is adjusted to remove this difference. This null-balancing keeps the temperature of the sample and reference pans equal to each other by continuous and automatic adjustment of the heater power to the sample pan. A signal that is proportional to the difference between the heat input to the sample pan and the heat input to the reference pan, $\frac{dH}{dt}(T)$, is then monitored.

The thermal mass of the sample and reference holders are kept to a minimum and the thermal resistance between the pans and their holders, $R_0$ (which is the same for both the reference and the sample), are reduced as much as possible. This allows for the use of a high loop gain in the control of differential power. As a result, in the ideal situation, response time is short and the assumption that the sample and reference pans are always at the same temperature is valid. The response of the system depends on the thermal resistances between the holders and the surroundings, but this is independent of the sample. Moreover, for a small sample mass in close thermal contact with the sample pan,
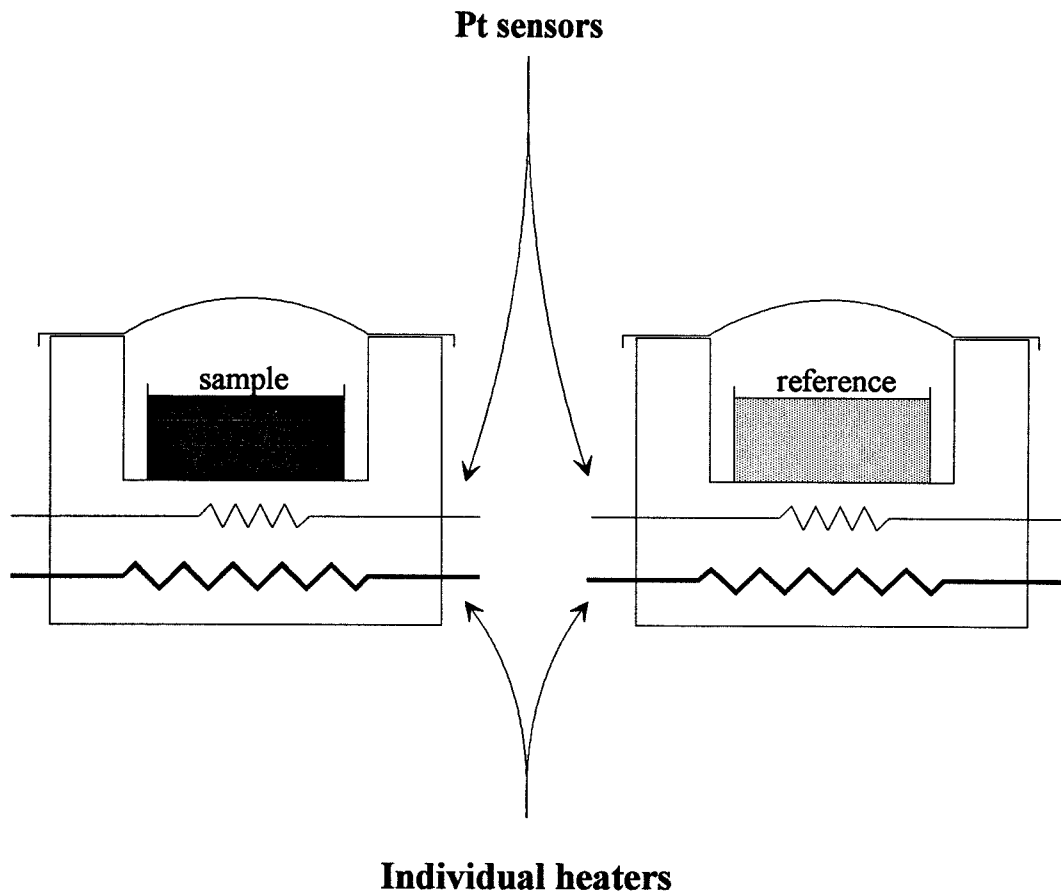
Figure 2.24a– A schematic of the DSC showing sensors, heaters and positioning of the sample and reference pans.
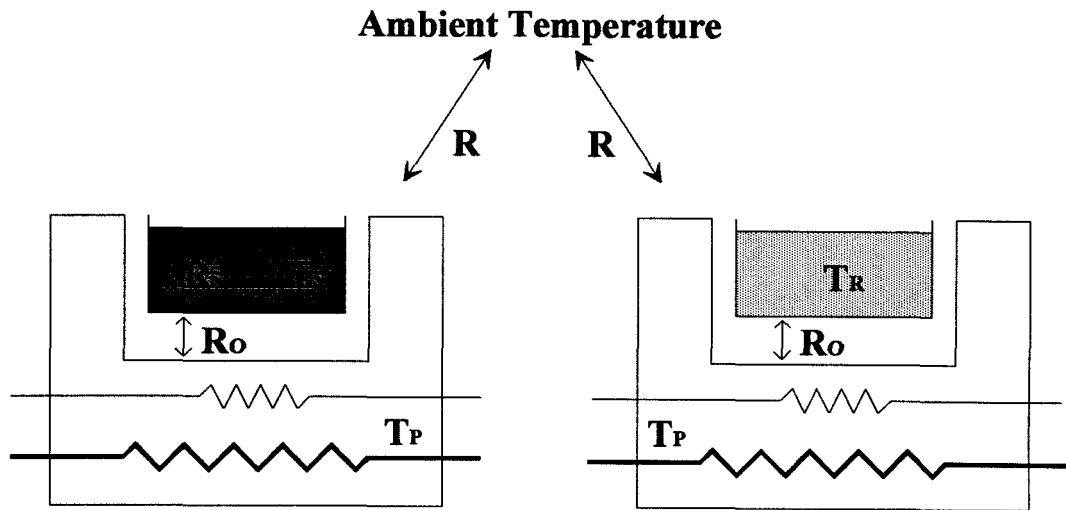
Figure 2.24b– A schematic showing the various thermal resistances in the DSC.

the thermal resistance associated with sample and the pan, $R_s$, is very small at moderate scanning rates when compared to the resistance between the pan and the holder, $R_0$. A schematic of the thermal resistances is shown in the inset in figure 2.24b.

DSC scans were done at various partial pressures of oxygen. The atmosphere in the sample area was controlled by two flowmeters: one for argon gas and one for oxygen. A bubbler at the exit ensured that the overall flow rate was constant from run to run (and that the total pressure in the system was approximately one atmosphere). The gaseous mixture was run through an $CaCO_3$ dessicant/filter before entering the DSC. When the run was to be done in pure Argon, the gas was also passed through an activated charcoal filter to remove any oxygen. The system was always taken to 600°C and left there for 45 minutes in the flowing gas mixture to be used before actually making the run. Baseline scans always followed actual DSC scans in order to obtain greater accuracy. The sample pans used were aluminum. An empty aluminum pan was run in full oxygen several times to ensure that no signal arose from its oxidation.

Scans were made in pure argon, pure oxygen and a 16% oxygen mixture at various scanning rates (5, 10, 20 and 40 K/minute). Scans were run with powders that were fully "charged" (i.e., with an oxygen content of ~6.9 oxygens per unit cell) and powders that were fully "discharged" (i.e., with an oxygen content of ~6.1 oxygens per unit cell). Typical sample weights were between 35 mg. and 50 mg. of material.

DSC scans made in open pans such as this result in measurements of enthalpy change at constant pressure. Measurement of this transition under such thermodynamic constraints results in the measurement of an enthalpy for the entire reaction, including any order-disorder phenomena occuring in the sample and any oxygen liberation from the sample. However, in the case of the orthorhombic–tetragonal transition studied here, the evolution of gas produces a strong endothermic signal that may mask other transitions in the sample, such as the disordering of oxygens on the sublattice prior to liberation from

the material. Also, the liberation of oxygen changes the composition of the material during the scan.

One way to maintain a fairly constant sample concentration of oxygen is to place the sample in a sealed DSC pan. A small amount of gas evolution will cause a rapid buildup in the oxygen pressure above the sample until the chemical potential of the gas equilibrates with the chemical potential of oxygen in the solid. Thus, gas evolution is reduced to the rate necessary to maintain equilibrium as the sample temperature is changed.

To accomplish this sealing of DSC sample pans, we first used Perkin-Elmer high pressure DSC pans made of 304 stainless steel and sealed by a Viton™ O-ring (shown schematically in figure 2.25). The seal is made by squeezing the closefitting lid over the base and O-ring using a handheld press. The compressed metal opposes the force generated by internal overpressure and the O-ring need only withstand a small force at the seal. The temperature limits of this pan are determined by the glass transition of Viton™ rubber at −40°C and the experimentally observed decomposition of the rubber O-ring at temperatures ≥425°C. No leakage was ever detected from the pan, but the pan's lid would bow out when the internal pressure reached too high a value. The pan is rated to an internal pressure of 25 atmospheres. The heat generated by deforming the pan is exactly canceled by the cooling of the gas inside the pan upon expansion of the internal volume. Nevertheless, a net endothermic signal occurs because more gas must be evolved to re-establish equilibrium with the chemical potential of the remaining gas in the solid.

For these experiments, pans were sealed in a glove bag in pure oxygen. Scanning rates used were between 5 and 40K/min. and a reference empty pan sealed in pure oxygen was scanned to make sure that no signal arose from the oxidation of the stainless steel pans.

DSC pans were also sealed hermetically by crimping aluminum pans with a form fitting lid in a hand-operated press. This method of sealing did not allow containment of

**Viton O-ring**



**304 stainless steel pans**
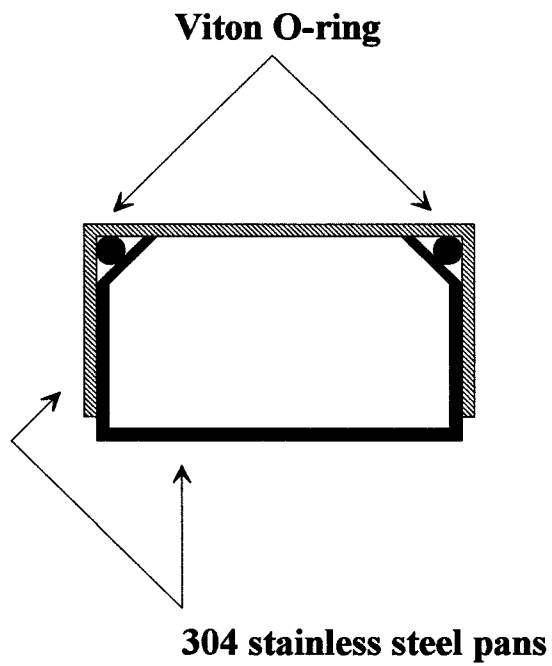
Figure 2.25– The Viton™ sealed stainless steel DSC sample pans.

as high an internal pressure as the aforementioned technique, but had the advantage of being structurally sound over the entire operating range of the DSC-4 (which has a maximum operating temperature of 600°C). Pans sealed in this way could, on the average, sustain internal pressure of 2-3 atmospheres, but leaked quite often and would burst if the sample mass was too great. This method of sealing was necessary because no signal was seen from the DSC up to the upper limit of usability in temperature for the stainless steel sample pans. It was possible that the transition was occurring above 425°C.

### II.E.2 Differential Scanning Calorimetry of YBa$_2$Cu$_3$O$_{6+\delta}$ as a Function of Oxygen Partial Pressure - Results with an Open Sample Pan

Shown in figure 2.26 is a scan done in pure Argon at 20K/min. in an open pan, beginning with fully "charged" material ($\delta$~1). As can be seen from the figure, the peak extends beyond the maximum upper temperature limit attainable with the Perkin-Elmer DSC-4. At the faster rate of 40K/min., this peak was shifted to even higher temperatures because of the lag in the system from finite thermal resistances. However, extending the baseline and transition peak curves until they intersect gives a closed area which can then be integrated to calculate an enthalpy for the transition. Table 2.1 shows the results of the enthalpies calculated in this manner. As a comparison, the enthalpy associated with the cubic–tetragonal transition in PbTiO$_3$ is 1.46 kJ/mol. The enthalpy associated with the $\alpha$–$\beta$ transition in the Pd–H system is 10.5 kJ/mol. By referring to figure 2.3, we can look up the ending oxygen content of the material at 600°C and the partial pressure of oxygen used. Because the peaks were not complete, the numbers are only estimates.

### Table 2.1 – Enthalpy of the Orthorhombic–Tetragonal Transition

| Atmosphere | Enthalpy (kJ/mol) |
|------------|-------------------|
| Argon | 5.2 |
| 16% Oxygen | 2.0 |
| 100% Oxygen | 1.7 |
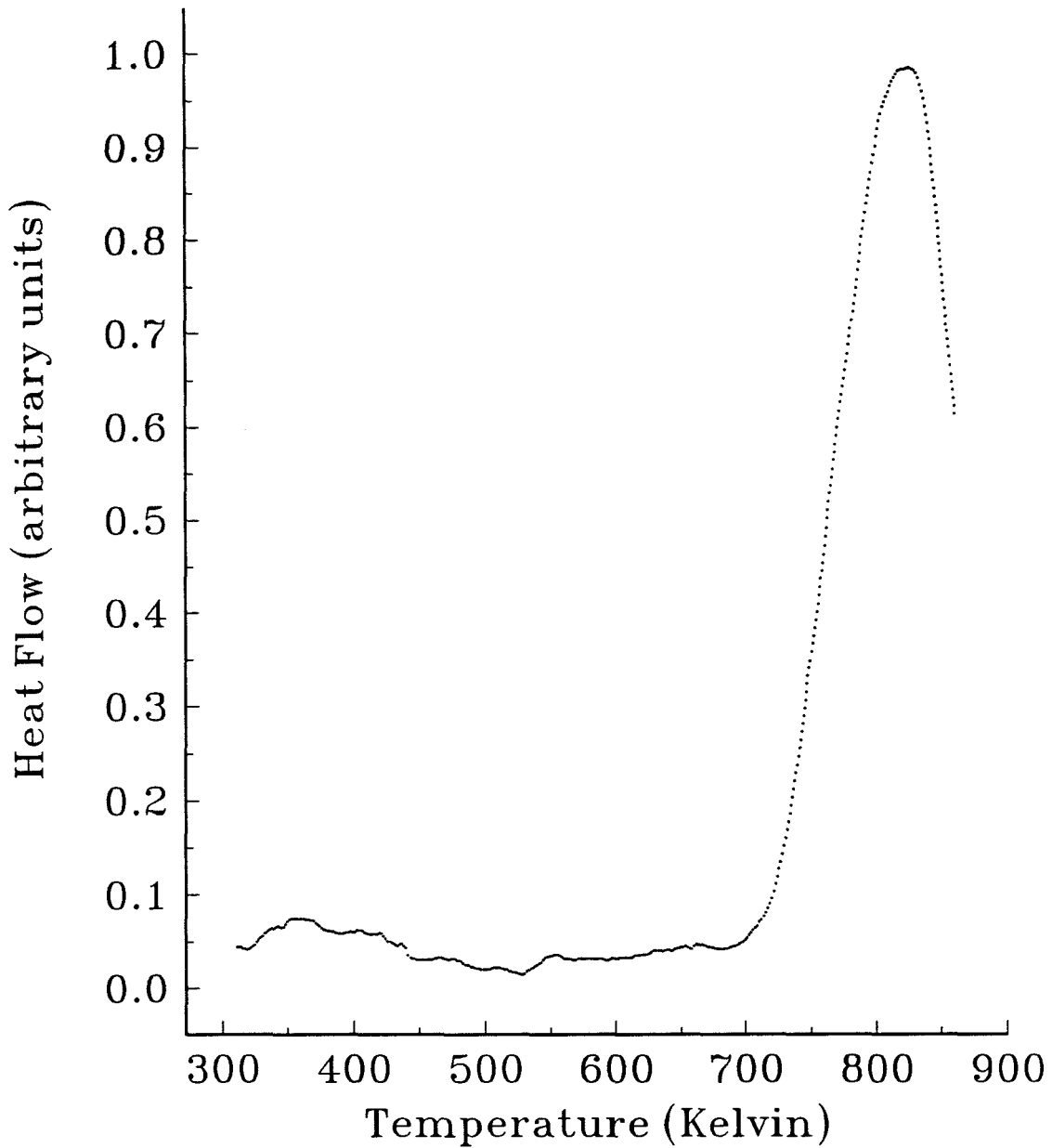
Figure 2.26– DSC trace taken at 20K/minute in flowing Argon.

Several different scan rates were used in order to attempt to perform a Kissinger analysis on the peak variation with scan rate. According to Kissinger,[57] the activation energy $E_A$ of a single, thermally activated endothermic or exothermic transition in a DSC trace can be estimated from the dependence of the transition peak temperature $T_p$ on scanning rate $r$ according to the equation:

$$\frac{d\left(\ln\frac{r}{T_p^2}\right)}{d\left(\frac{1}{T_p}\right)} = -\frac{E_A}{k_B} . \qquad \text{(II.18)}$$

This expression is only accurate when the reaction is dominated by one thermally activated process with an Arrhenius temperature dependence. If a reaction includes more than one thermally activated process, the analysis may not give reasonable results.[58] The slope of a best fit line to the above equation gives the activation energy and the fit of the line gives an estimate of its uncertainty.

The activation energy for the transition in the various pressures of oxygen are listed in Table 2.2. They were determined using a standard Kissinger analysis as described above. The regression analysis provides a good fit to the data. This indicates that the orthorhombic–tetragonal phase transition in the $YBa_2Cu_3O_{6+\delta}$ under conditions of constant chemical potential is in fact dominated by one thermally activated process.

Physically, what occurs during the transition is a combination of the disordering of oxygens on the sublattice and an evolution of oxygen from the solid. Thus, there are actually two possible thermally activated reactions that occur. Since the Kissinger analysis of peak variation seems to hold, it would imply that one of these two reactions is the dominant contributor to the endothermic signal seen in the scan. In the field of metal hydrides, liberation of hydrogen from a metal is often a large endothermic signal which can

**Table 2.2 – Kissinger Analysis of the Endothermic Peak**

| Atmosphere | Activation Energy (eV/atom) |
| --- | --- |
| Argon | 1.2  (r=0.98) |
| 16% Oxygen | 1.8  (r=0.97) |
| 100% Oxygen | 2.3  (r=0.97) |

mask any underlying transition occurring in the solid.[59]  Because we have seen that the physics of the orthorhombic–tetragonal phase transition in $YBa_2Cu_3O_{6+\delta}$ is similar to that of order-disorder phenomena metal-hydrides, we can guess that this large endotherm is probably due to the liberation of oxygen from the compound.

**II.E.3    Differential Scanning Calorimetry of $YBa_2Cu_3O_{6+\delta}$ as a Function of Oxygen Partial Pressure - Results with a Sealed Sample Pan**

One way to study the order-disorder transition on the oxygen sublattice without the effect of oxygen volatility is to seal the sample pan.  It might be possible to see the signal from the order-disorder transition if the sample were subjected to the proper thermodynamic constraints:  namely, one of constant composition in the sample.

In doing these experiments, it was found that when the weight of the sample in the pan exceeded 7mg., the pan exploded.  This event showed up as an instantaneous jump in the DSC trace above the maximum endothermic signal measurable.  An example of this signal is shown in figure 2.27.

Unfortunately, keeping the amount of sample under 7mg. reduces the signal from the transition (if it is there) to below detectable levels.  Scans done with pans that did not burst showed no signal throughout the entire temperature range.  If the transition were of second order, the jump in heat capacity would manifest itself as a step in the DSC signal.  However, no such signal was observed.

In conclusion, the sealed sample pan DSC runs provided no further information about the order–disorder transition on the oxygen sublattice in $YBa_2Cu_3O_{6+\delta}$.  The stainless steel pans, which are capable of withstanding up to 25 atmospheres of internal pressure, could not reach the temperature range of interest because the O-ring would melt at ~425°C, and the pressure sealed aluminum sample pans failed above ~3 atmospheres,

thus limiting the total amount of sample allowed in the pan to a point where the signal

from the transition was not detectable.
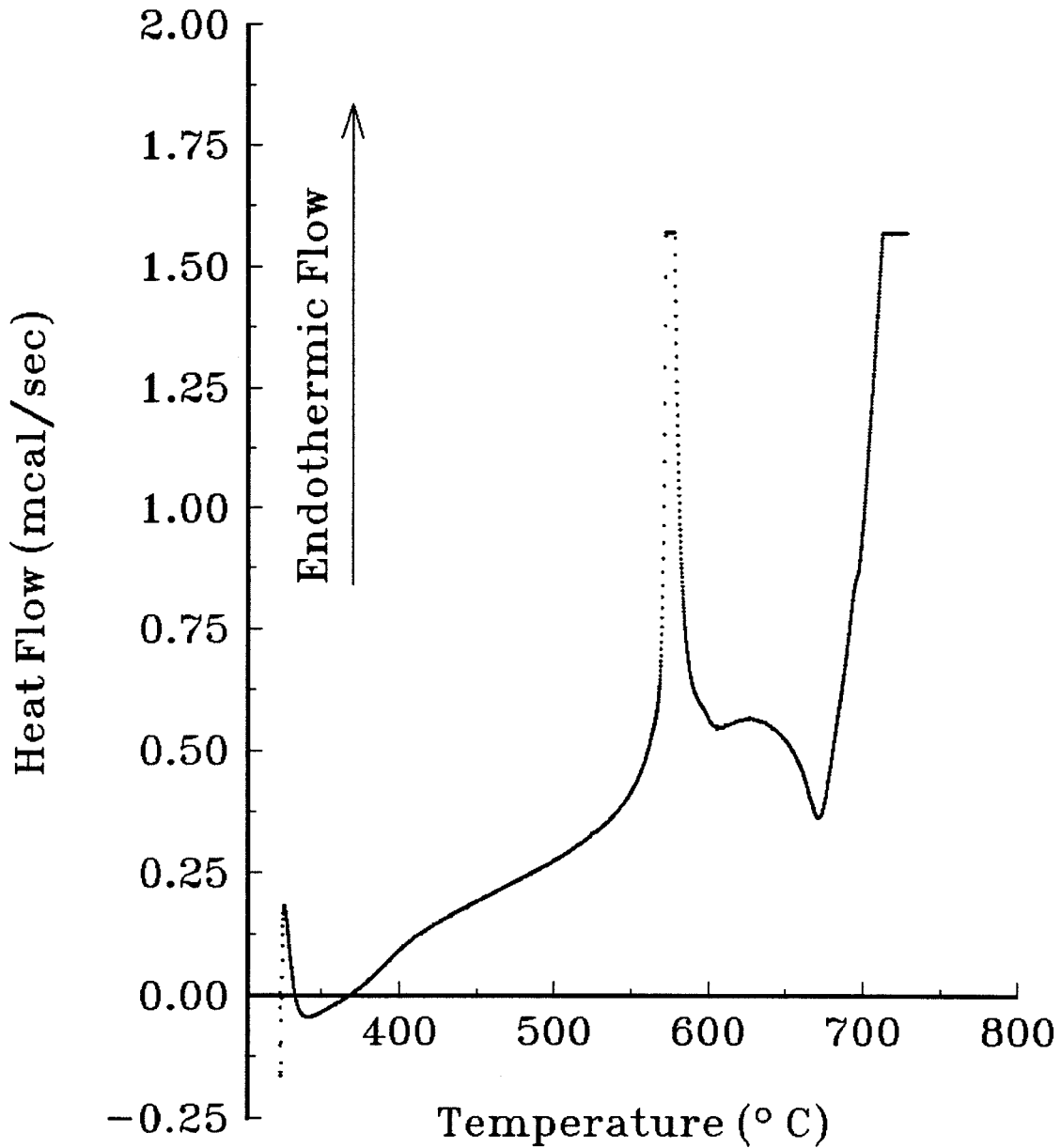
Figure 2.27– DSC trace of a sealed aluminum pan with mechanical failure at ~700K.

---

# <u>REFERENCES FOR CHAPTER 2</u>

[1]Shi, Capone II, Goretta, Zhang and Goudey, J. Appl. Phys. **63** (1988), p. 5411.

[2]The thermogravimetric analysis was done by Valerie Patrick, a former graduate student in Chemical Engineering.

[3]op. cit., Shi et al.

[4]Gerdanian, Picard and Marucco, Physica C **157** (1989), p. 180.

[5]McKinnon, Post, Selwyn, Pleizer, Tarascon, Barboux, Greene and Hull, Phys. Rev. B **38** (1988), p. 6543.

[6]Gallagher, Adv. Cer. Mat. **2** (3B) (1987), p. 632.

[7]Stroebel, Capponi, Marezio and Monod, Sol. St. Comm. **64** (1987), p. 513.

[8]op. cit., Gerdanian, Picard and Marucco.

[9]op. cit., Jorgensen et al.

[10]M. O. Eatough, D. S. Ginley, B. Morosin and E. L. Venturini, Appl. Phys. Lett. **51** (1987), p. 367.

[11]J. Hauck, K. Bickmann and F. Zucht, Z. Phys. B **67** (1987), p. 299.

[12]R. Liang and T. Nakamura, Jap. J. Appl. Phys. **27** (1988), p. 1277.

[13]R. Cava, A. Hewat, E. Hewat, B. Batlogg, M. Marezio, K. Rabe, J. Krajewski, W. Peck Jr. and L. Rupp Jr., Phys. C **165** (1990), p. 419.

[14]R. Beyers, B. Ahn, G. Gorman, V. Lee, S. Parkin, M. Ramirez, K. Roche and J. Vazquez, Phys. C **162** (1989), p. 548.

[15]op. cit., Aukrust, Novotny, Rikvold and Landau.

[16]op. cit., Berera and deFontaine.

[17]Bakker, Welch and Lazareth, Sol. St. Comm. **64** (1987), p. 237.

[18]Bakker, Westerveld, LoCascio and Welch, Physica C **157** (1989), p. 25.

[19]Bell, Phys. Rev. B **37** (1988), p. 541.

[20]Shaked, Jorgensen, Faber, Hinks and Dabrowski, Phys. Rev. B **39** (1989), p. 7363.

[21]Berera and deFontaine, Phys. Rev. B **39** (1989), p. 6727.

[22]Khachaturyan, Semonovskaya and Morris, Phys. Rev. B **37** (1988), p. 2243.

[23]op. cit., McKinnon et al.

[24]Aukrust, Novotny, Rikvold and Landau, Phys. Rev. B **41** (1990), p. 8772.

[25]op. cit., Berera and deFontaine.

[26]op. cit., Bell.

[27]op. cit., Khachaturyan, Semonovskaya and Morris.

[28]op. cit., Bakker, Westerveld, LoCascio and Welch.

[29]op. cit., Shaked et al.

[30]Kerr and Trotman-Dickson, *Handbook of Chemistry and Physics,* 62nd edition (CRC Press, Boca Raton, Florida, 1981) p.F-180.

[31]op. cit., Shaked et al.

[32]op. cit., Jorgensen et al.

[33]O'Bryan and Gallagher, Adv. Cer. Mat. **2** (3B) (1987), p. 640.

[34]Specht, Sparks, Dhere, Brynestad, Cavin, Kroeger and Oye, Phys. Rev. B **37** (1988), p. 7426.

[35]ibid.

[36]Jorgensen, Shaked, Hinks, Dabrowski, Veal, Paulikas, Nowicki, Crabtree, Kwok and Nunez, Physica C **153** (1988), p. 578.

[37]Kubo, Nakabayashi, Tabuchi, Yoshitake, Ochi, Utsumi, Igarashi and Yonezawa, Jpn. J. Appl. Phys. **26** (1987), p. L1228.

[38]Meuffels, Rupp and Pörschke, Physica C **156** (1988), p. 441.

[39]Salomons, Koeman, Brower, deGroot and Griessen, Sol. St. Comm. **64** (1987), p. 1141.

[40]R. Feenstra, R. Griessen and D. G. deGroot, J. Phys. **F16** (1986), p. 1933.

[41]R. Feenstra and R. Griessen, Sol. St. Comm. **59** (1986), p. 905.

[42]R. J. Cava, B. Batlogg, R. B. van Dover, D. W. Murphy, S. Sunshine, T. Siegrist, J. P. Remeika, E. A. Rietman, S. Zahurak and G. P. Espinosa, Phys. Rev. Lett. **58** (1987), p. 1676.

[43]P. Steiner, V. Kinsinger, I. Sander, B. Siegwart, S. Hufner and C. Politis, Z. Phys. **B67** (1987), p. 19.

[44]L. F. Mattheis and D. R. Hamann, Sol. St. Comm. **63** (1987), p. 395.

[45]S. Massidda, J. Yu, A. J. Freeman and D. D. Koelling, Phys. Lett. **122A** (1987), p. 198.

[46]op. cit., Berera and deFontaine.

[47]op. cit., R. J. Cava et al.

[48]op. cit., Beyers et al.

[49]D. I. Werder, C. H. Chen, R. J. Cava and B. Batlogg, Phys. Rev. B **37** (1988), p. 2318.

[50]op. cit., Berera and deFontaine.

[51]op. cit., Aukrust et al.

[52]G. Cedar, M. Aster, W. C. Kraitchman, D. deFontaine and M. E. Sluiter, Phys. Rev. B **41** (1990), p. 8698.

[53]R. Kikuchi and J. S. Choi, Physica C **160** (1989), p. 347.

[54]V. E. Zubkus, S. Lapinskas and E. E. Tornau, Physica C **159** (1989), p. 501.

[55]E. Porschke, P. Meuffels and H. Wenzl, J. Phys. Chem. Sol. **53** (1992), p. 73.

[56]They attempted to fit the model to their data with no success. My data is superimposed on the graph.

[57]R. N. Rogers and E. D. Morris, Jr., Analytical Chem. **38** (1966), p. 412. (obviously, the label "Kissinger analysis" is a misnomer. Kissinger actually developed a technique to

measure activation energies from a differential thermal analyzer (DTA); Rogers and Morris adapted it to the differential scanning calorimeter.

[58]D. W. Henderson, J. Non-Cryst. Sol. **30**, (1979), p. 301.

[59]C. E. Krill III, Ph. D. Thesis, Cal. Inst. Tech. (1992), p. 112.

# III.  The Effect of Mechanical Milling on YBa2Cu3O6+δ Powder

*Overview-*

High temperature x-ray diffraction (Hi-T XRD) and differential scanning calorimetry (DSC) were used to study the effect of high energy mechanical deformation on the structural and thermal characteristics of $YBa_2Cu_3O_{6+\delta}$ powder.  A Warren-Auerbach analysis was done on the x-ray peaks to determine the grain size of the material as a function of milling time.  A Phillips 430 transmission electron microscope (TEM) equipped with an EDX detector was used to determine chemical composition and to check the grain size of the ball-milled material.

Broadening of Bragg peaks due to the reduction of grain size makes the distinction between orthorhombic and tetragonal phases of $YBa_2Cu_3O_{6+\delta}$ difficult after only one hour of ball milling.  The equilibrium orthorhombic to tetragonal phase transition, characterized by the loss of oxygen from the basal Cu-O planes in the compound,[1] may occur within the first hour of ball-milling.  Longer milling times (>5hrs) produce a cationic disorder on the yttrium and barium sites.  A metastable cubic $(Y_{1/3}Ba_{2/3})CuO_{2+\delta}$ structure with a= 3.86Å is formed.  Further mechanical deformation does not induce the formation of an amorphous phase;  rather, an eventual decomposition into the constituent oxides $Y_2O_3$, BaO and $Cu_2O$ is observed.  Annealing of the metastable cubic $(Y_{1/3}Ba_{2/3})CuO_{2+\delta}$ phase in relatively low pressures of oxygen (≥100mbar) and at moderate temperatures (~400–600°C) produces an as yet unidentified cubic phase which is unstable in air and has a lattice constant of a= 5.47Å.

## III.A  The Mechanical Milling Experiment

### III.A.1  Experimental Details

The milling machine used was a SPEX model 8000 Mixer/Mill. It is shown in schematic in figure 3.1. Initially, steel vials and balls were used, but a subsequent EDX (energy dispersive analysis of x-rays) check on the powders revealed significant contamination from the vial and balls [≈1% by mass, or, assuming full substitution into the structure, $YBa_2(Cu_{~2.9}Fe_{~0.1})O_{6+\delta}$]. To avoid such severe contamination, the vial and ball material was switched to zirconia. After making this switch, contamination from the vial and balls was reduced to below detectable levels, even after 100 hours of milling. This is significant because the only previously published data on ball-milling of $YBa_2Cu_3O_{6+\delta}$, done by Lavallée et al., used hardened steel vials and balls, which have a hardness of roughly ½ GPa.[2] The $YBa_2Cu_3O_{6+\delta}$ compound has a hardness of about 2.0 GPa as a polycrystal[3] and 8.7 GPa as a single crystal,[4] both of which are far above the hardness of the steel balls and vial; the $YBa_2Cu_3O_{6+\delta}$ powder can thus grind down the vial wall and ball surface, resulting in non-negligible contamination. Lavallée et al. reported that after 60 hours of milling, they found contamination of between 0.5% and 1% by mass. Moreover, Tarascon et al.[5] have shown that iron readily substitutes for copper in the crystal structure and causes an orthorhombic to tetragonal structural phase transition in the compound. A substitution of $YBa_2(Cu_{2.9}Fe_1)O_{6+\delta}$ gives a tetragonal structure with an a-axis lattice parameter of 3.86Å. Figure 3.2 shows the lattice parameter of the compound $YBa_2(Cu_{3-x}Fe_x)O_{6+\delta}$ as a function of iron content.

As might be expected, iron substitution also results in a degradation of the superconducting properties, though not severely when substituted in small quantities.

# Clamp, Pillow Block and Shaft Assembly
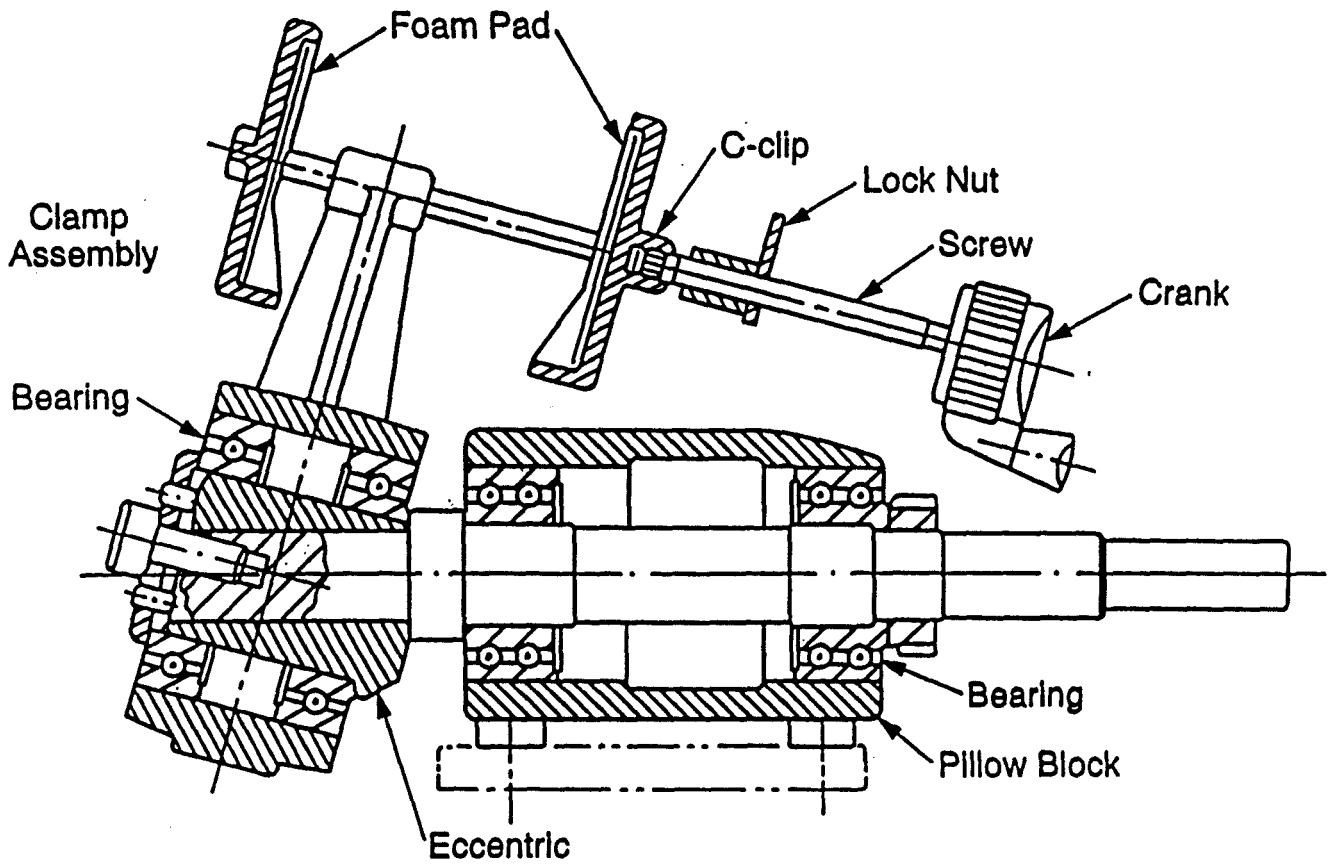


Figure 3.1– Schematic of the Spex 8000 Mixer/Mill.

# Lattice Parameter versus Iron Content
## in $YBa_2(Cu_{3-x}Fe_x)O_{6+\delta}$
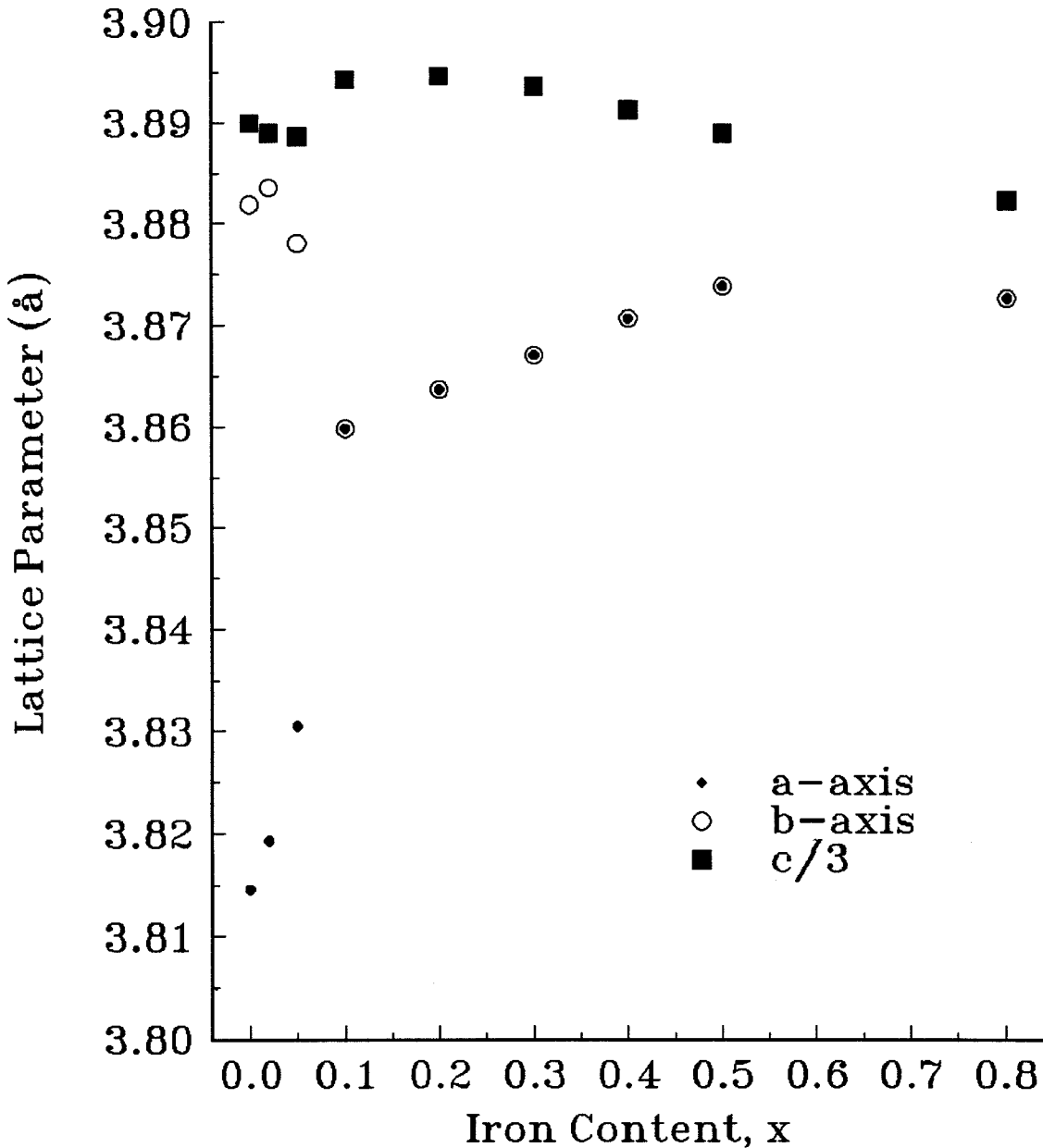


Figure 3.2– Lattice parameter as a function of iron content in $YBa_2(Cu_{3-x}Fe_x)O_{6+\delta}$. Note that the structure is tetragonal by the time the substitution reaches $YBa_2(Cu_{2.9}Fe_1)O_{6+\delta}$.

Shown in figure 3.3 is a plot of the superconducting transition temperature, $T_C$, versus iron content. A substitution of 5% iron (by mass) results in the total loss of superconductivity in the compound (this would be equivalent to a formula of $YBa_2(Cu_{2.5}Fe_{0.5})O_{6+\delta}$).

Iron contamination introduces an additional level of complexity to the problem: namely, how the $YBa_2Cu_3O_{6+\delta}$ compound behaves under mechanical milling. This added complexity manifests itself through its effect on both crystal structure and crystal physics.

Some of the x-ray diffraction patterns were taken on the same GE high temperature x-ray diffractometer as described in the previous chapter.[6] However, for x-ray diffraction patterns that did not require either high temperature or high resolution, an Inel 120° parallel detection diffractometer equipped with cobalt radiation ($\lambda=1.79$Å) was used. The system consists of a curved wire anode in flowing krypton gas and is shown in schematic in figure 3.4. An incident beam monochromator is used to remove $K_\beta$ radiation and the system has an equivalent resolution of about 0.03° in $2\theta$.[7] Because the system does not have true $\theta-2\theta$ geometry, an instrument correction for the detected intensity is required. Gao et al.[8] have shown that this function has the following analytical form:

$$I_D = I_o b \int_0^t \frac{A}{\sin\phi} \exp\left[-\mu z\left(\frac{1}{\sin\phi} + \frac{1}{\sin\xi}\right)\right] dz, \qquad (3.1)$$

where $A$ is the area of the incident beam $I_O$, $\phi$ is the incident angle, $\xi$ is the angle from the sample plane to the point of detection ($\xi=2\theta-\phi$), $t$ is the thickness of the sample, $I_D$ is the diffracted intensity off an incident beam intensity at depth $z$ of $I_O exp(-\mu z/\sin\phi)$ and $\mu$ is the linear absorption coefficient for the material. If the sample is assumed to be infinitely thick (that no x-rays penetrate the entire sample and emerge in transmission), then $t\rightarrow\infty$ and the equation simplifies to:

# $T_C$ versus Iron Content
## in $YBa_2(Cu_{3-x}Fe_x)O_{6+\delta}$
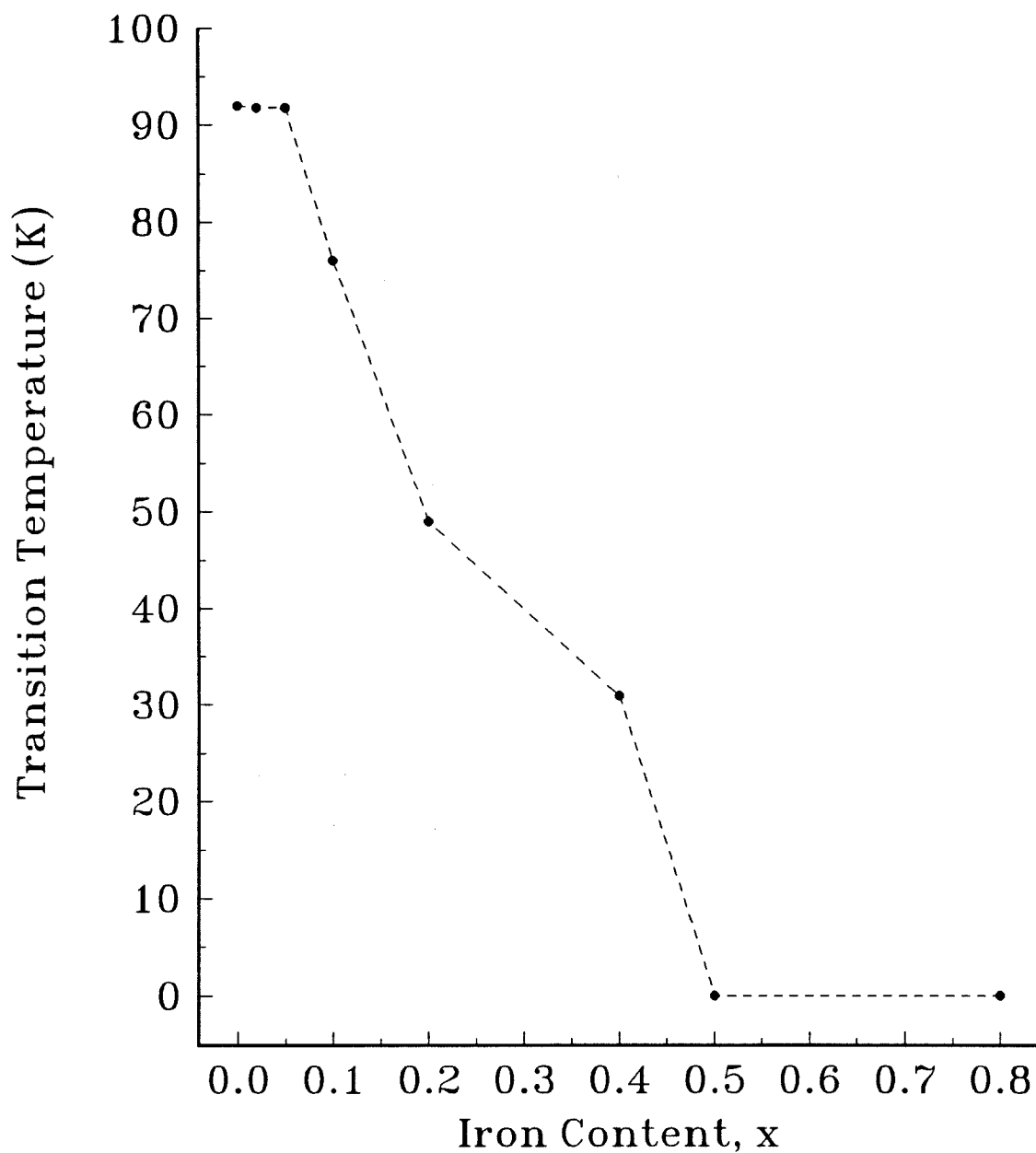


Figure 3.3– Superconducting transition temperature for the series $YBa_2(Cu_{3-x}Fe_x)O_{6+\delta}$.
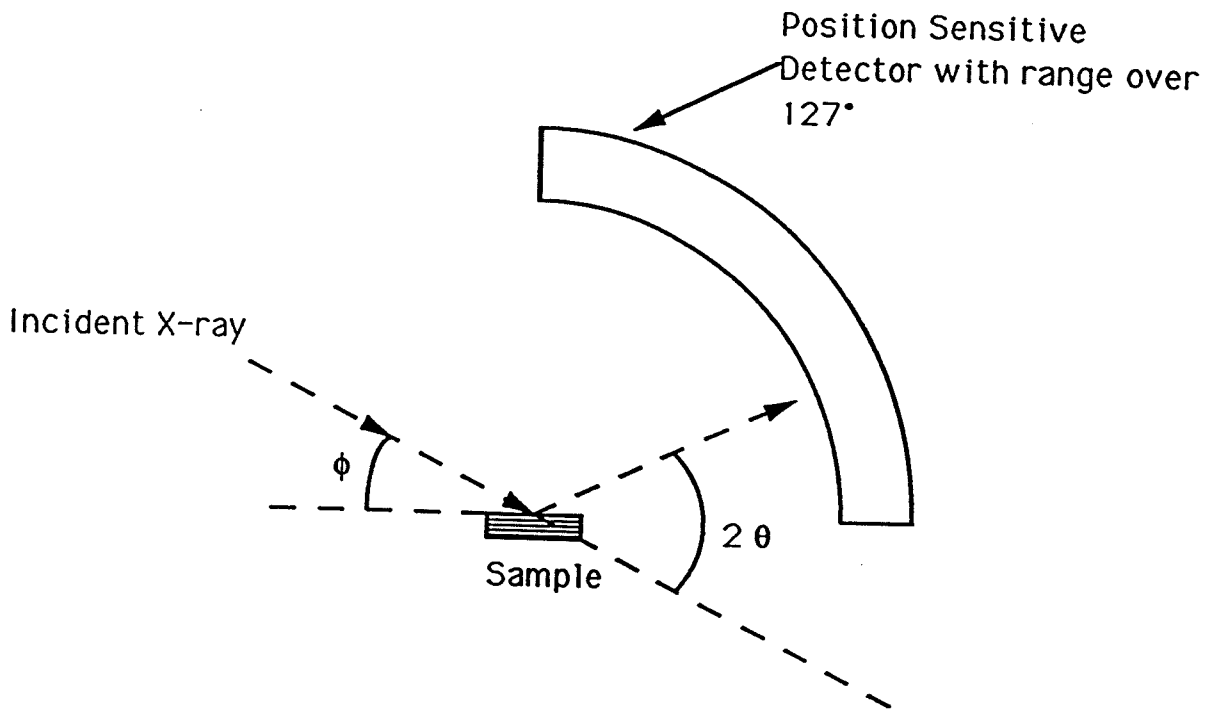
Figure 3.4– Schematic of the Inel 120° diffractometer.

$$I_D = \frac{I_o A}{\mu} \cdot \frac{\sin \xi}{\sin \phi + \sin \xi}.$$  (3.2)

The disadvantage of this system is its poor resolution in angle. The relatively poor energy resolution of a gas proportional counter (~1KeV) is circumvented by the use of an incident beam monochromator; however, bremmstrahlüng and flourescence radiation from certain samples can still reach the detector and must be removed by software corrections. Aluminum foil placed over the detector window can in theory be used to absorb the flourescence radiation, but wrinkles in the foil are known to produce spurious peaks in the spectrum. Also, the percentage absorption is dependent on the foil thickness.

Nonetheless, the disadvantages are far outweighed by the phenomenal reduction in time required for good counting statistics in the x-ray pattern for most materials. A typical powder sample reached 2% statistics on the background in less than fifteen minutes. Scans to the same statistical accuracy over the same angular range on the high temperature x-ray diffractometer took more than twelve hours. For the mechanically milled samples, it was clear that as deformation broadened the peaks through the introduction of defects and the reduction of grain size, good angular resolution would not be necessary.

We began with a ball-to-powder ratio of 1:1 (4.518g ball weight) and removed approximately 0.25g of powder during the milling at 1hr, 3hrs, 10hrs and 30hrs for x-ray and thermal analysis. By the end of the experiment, the ball-to-powder ratio was therefore about 1.28:1.

### III.A.2 Diffraction of the Milled Samples

X-ray diffraction patterns taken from samples milled for 1hr, 3hrs, 10hrs, 30hrs and 100hrs are shown in figure 3.5. Also shown are reference scans of the fully orthorhombic and fully tetragonal structures. As is evident from the scan of powder milled for one hour, peak broadening has made classification of the structure as either orthorhombic or tetragonal difficult. The peak broadening is due to a rapid reduction in grain size and some nominal strain accumulation. It is possible that the order-disorder transition on the oxygen sublattice has already occurred within the first hour of milling. Carbothermal reduction, done by Schulz et al.,[9] indicates that the compound does not lose oxygen during the first twenty hours of ball milling within the accuracy of their apparatus. However, as is shown in figure 3.6, the incorporation of Fe atoms onto Cu sites in $YBa_2Cu_3O_{6+\delta}$ causes an increase in the total oxygen content of the material. Thus, the observation of no loss of oxygen by Schulz et al. may in fact be an indication that their powders have lost some oxygen. The total amount of oxygen lost would still be small (on the order of $\Delta\delta \sim 0.1$), but easily within the resolution of their apparatus. As was shown in chapter 2, the amount of oxygen possibly lost is still far below that necessary to induce the orthorhombic–tetragonal phase transition in equilibrium $YBa_2Cu_3O_{6+\delta}$ powder. On the other hand, it is possible that after twenty hours of ball milling, iron substitution for copper may have been sufficient for an orthorhombic-tetragonal phase transition. In any event, the material that was mechanically milled here did not show any signs of superconductivity down to 20K after being milled.

After 30 hours of milling, the diffraction pattern contains only the six most intense peaks of the $YBa_2Cu_3O_{6+\delta}$ compound. Certain relatively intense orthorhombic peaks are

# Ball-milled $YBa_2Cu_3O_{6+\delta}$ Powder
## Hi−T XRD in rough vacuum
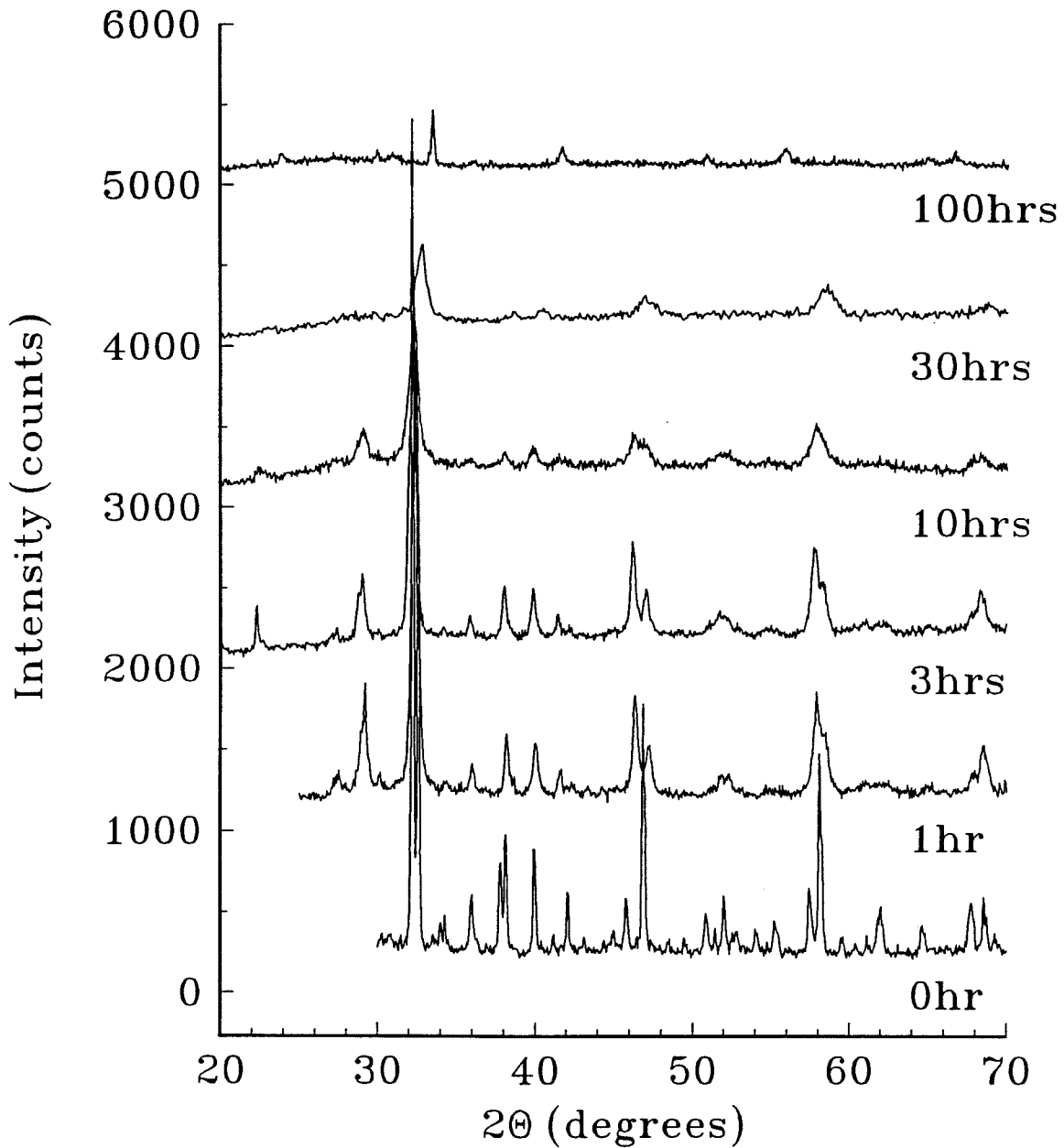


Figure 3.5– X-ray diffraction patterns of milled $YBa_2Cu_3O_{6+\delta}$.

# Oxygen Concentration versus Iron Content
## in $YBa_2(Cu_{3-x}Fe_x)O_{6+\delta}$
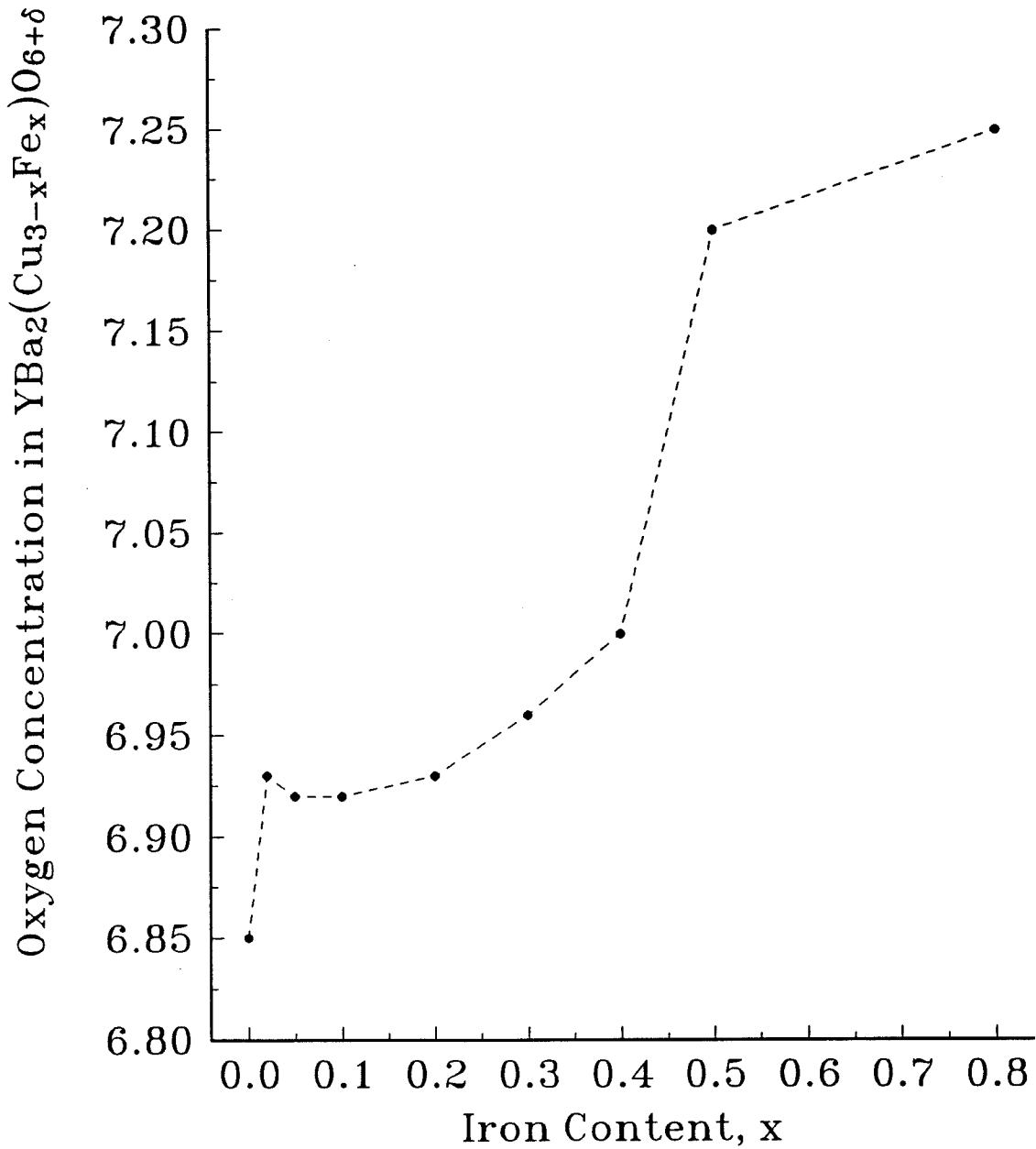


Figure 3.6– Oxygen content in $YBa_2(Cu_{3-x}Fe_x)O_{6+\delta}$ as a function of iron content.

notably absent; namely, the (001), (002) and (014) reflections (for reference, figure 2.2 is repeated as figure 3.7 and contains a diffraction pattern for orthorhombic $YBa_2Cu_3O_{6+\delta}$ with the major peaks indexed). The absence of these peaks, coupled with the presence of the other six major peaks associated with the $YBa_2Cu_3O_{6+\delta}$ compound, strongly suggests that the new compound is a derivative of the original $YBa_2Cu_3O_{6+\delta}$ structure shown in figure 1.1. Energy dispersive x-ray analysis done on a Phillips 430 TEM equipped with an EDX detector indicated that the cations were in the same ratio as that for the orthorhombic $YBa_2Cu_3O_{6+\delta}$ compound, so the new phase must have the same ratio of cations in its formula unit. A simple structure with complete disorder on the cationic (yttrium and barium) and anionic (oxygen) sites fits the data well. The six peaks can be indexed to such a cubic unit cell with lattice parameter a=3.86Å and two oxygen atoms per formula unit: $(Y_{1/3}Ba_{2/3})CuO_2$. Figure 3.8 shows the structure of the original tetragonal unit cell and the proposed new cubic unit cell. Table 3.1 shows the results of the calculated d-spacings and intensities for this unit cell along with the experimentally measured values. The agreement is excellent for the d-spacings and satisfactory for the intensities. The discrepancy between measured intensities and calculated intensities is probably due to displacement of the oxygen sites in the cubic unit cell from the ideal positions used. No structural refinements were performed on this structure to determine the precise placement of oxygen atoms within the unit cell.

## Table 3.1 – Intensities & d-spacings Of Cubic Phase

| (hkl) | $d_{Obs}$(Å) | $d_{Calc}$(Å) | $I_{Obs}$(%) | $I_{Calc}$(%) |
|-------|--------------|---------------|--------------|---------------|
| 100   | 3.87         | 3.86          | 9.2          | 5.7           |
| 110   | 2.73         | 2.73          | 100.0        | 100.0         |
| 111   | 2.24         | 2.23          | 8.0          | 8.4           |
| 200   | 1.93         | 1.93          | 25.2         | 29.2          |
| 210   | 1.73         | 1.73          | 4.0          | 2.8           |
| 211   | 1.58         | 1.58          | 34.7         | 41.0          |
| 220   | 1.37         | 1.37          | 7.7          | 18.7          |
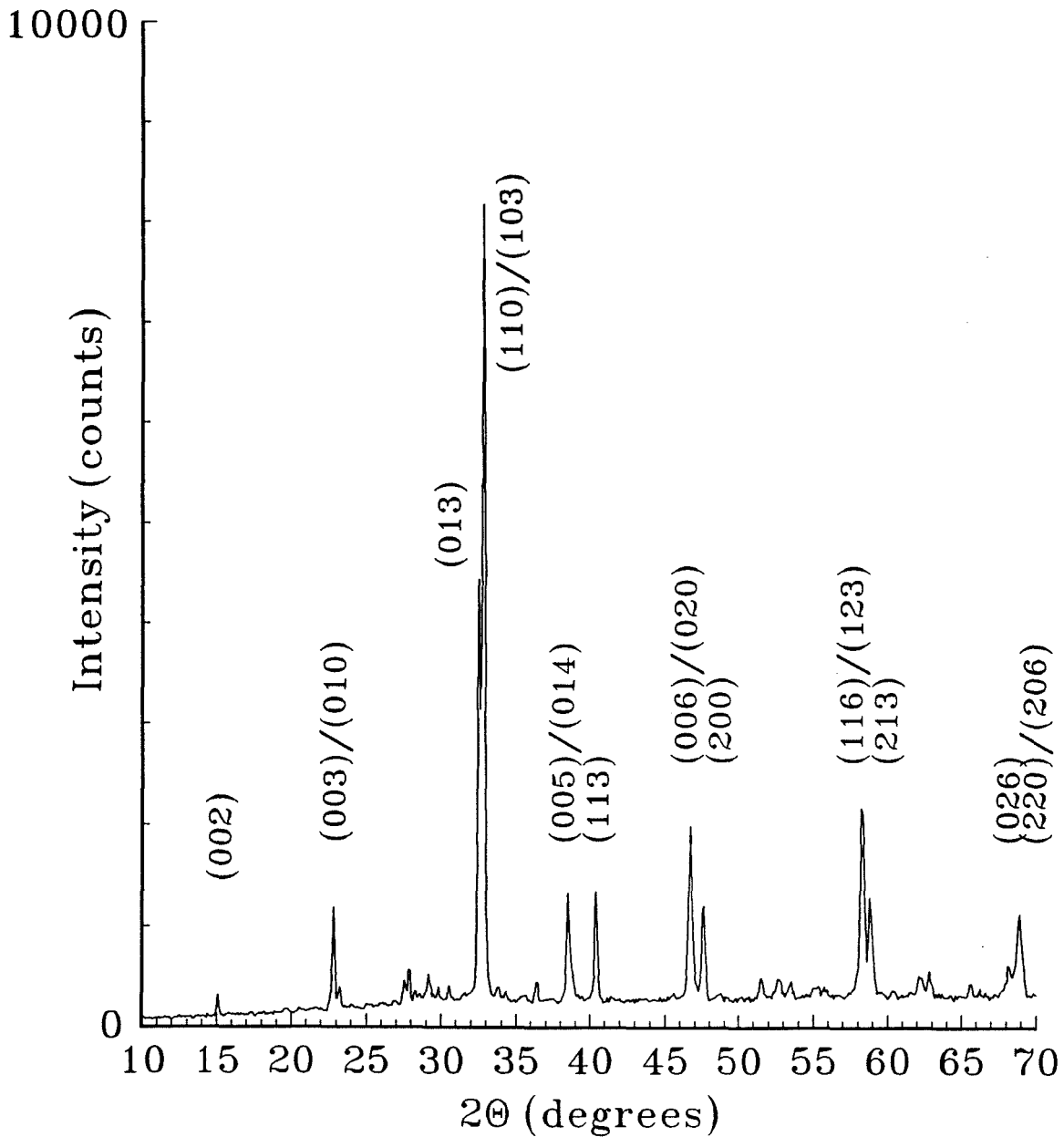
Figure 3.7– The orthorhombic $YBa_2Cu_3O_{6+\delta}$ diffraction pattern with its major peaks indexed.

**Y or Ba**
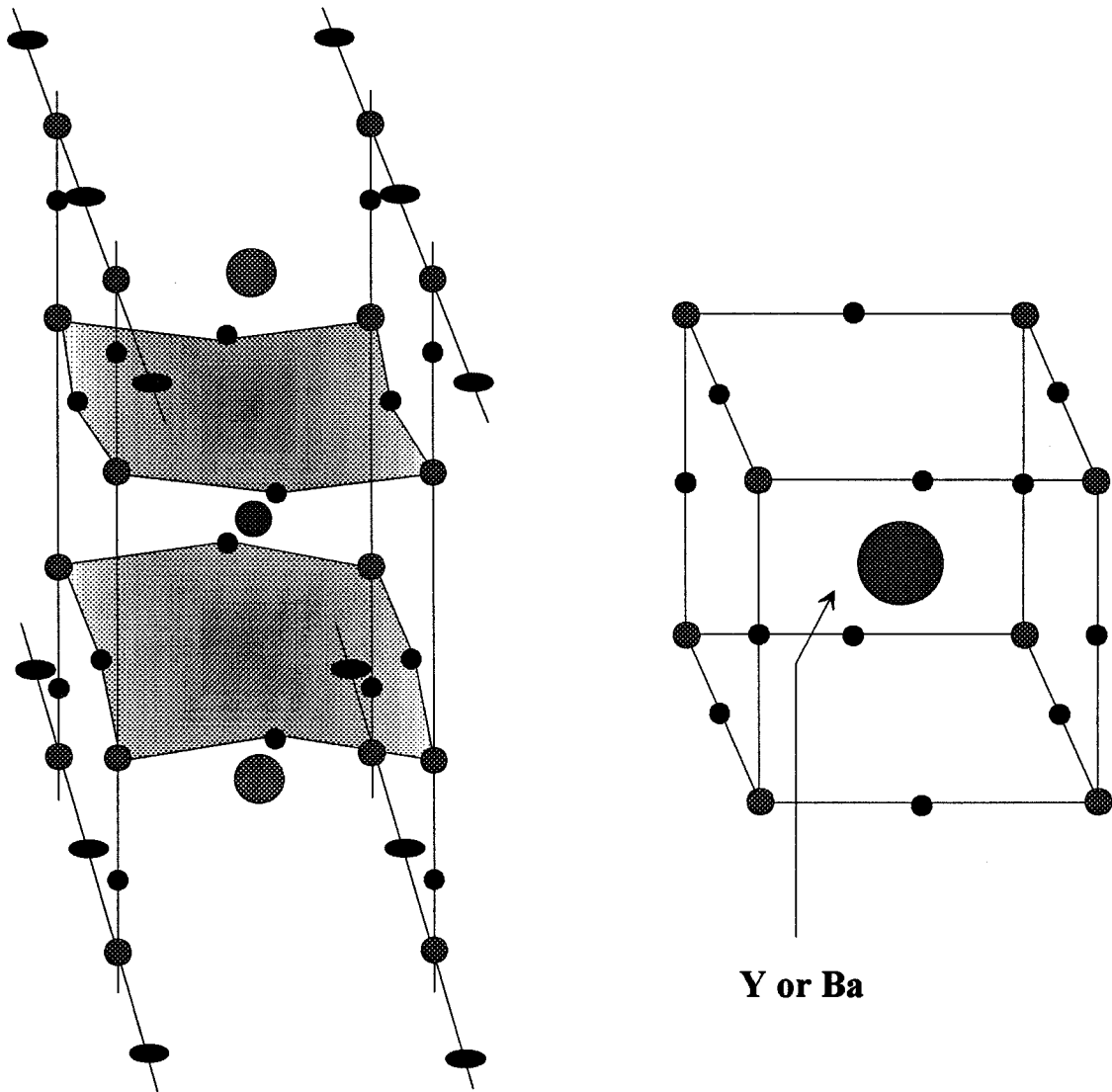
original
tetragonal
unit cell

proposed
cubic
unit cell

Figure 3.8– The tetragonal $YBa_2Cu_3O_{6+\delta}$ cell and the proposed new cubic $(Y_{1/3}Ba_{2/3})CuO_{2+\delta}$ cell.

### III.A.3 Transmission Electron Microscopy of the Milled Samples

Transmission electron microscopy was also used to determine the average grain size of the ball-milled powder as a function of milling time. The samples were prepared by grinding the milled powder in methylene chloride in an agate mortar and pestle and then floating onto a holey carbon grid. $YBa_2Cu_3O_{6+\delta}$ grows in flat platelets, with an aspect ratio of about 0.1 (heighth to width). Thus, powder samples thin enough to do dark field imaging in the TEM tended to be aligned in the [001] direction (or nearly along this axis). The grain sizes determined from TEM are therefore grain sizes "in the a-b plane." After the material becomes cubic, this corresponded to the natural grain size of the material.

With TEM, it was possible to see the manner in which the grain size decreased. At the shorter milling times, smaller grains first formed around the edges of larger grains as the brittle material crumbled on impact with other grains. After one hour of milling, the larger grains were still 400nm. in diameter, although the average grains size had decreased significantly. On the edges of these grains were much smaller grains (10-50nm). After three hours of milling, relatively scarce larger grains were typically 100-200nm with more fine-grained material at the edges. After ten hours of milling, most of the grains were in the 10-50nm range. The image field showed a mixture of the original tetragonal $YBa_2Cu_3O_{6+\delta}$ phase and the cubic phase. After thirty hours of milling, the distribution of grain sizes narrowed even more as the grains were 5-20nm in size. At this point, the first signs of phase decomposition into $Y_2O_3$ and $BaCuO_2$ at the grain boundaries were seen. The image field now consisted of a mixture of the phases found after ten hours and the decomposed oxides. Finally, after 100 hours of milling, a large percentage of the material had decomposed into an oxide mixture. These results are consistent with x-ray diffraction

**Table 3.2 – Grain Size by TEM**

| Milling Time (hours) | Grain Size (nm) |
| --- | --- |
| 0 | 1000 |
| 1 | 20-200 |
| 3 | 10-50 |
| 10 | 10-50 |
| 30 | 5-20 |
| 100 | — |

patterns shown in figure 3.6. Throughout the milling process, the particle size stayed relatively constant at about 1 μm. The results are shown in Table 3.2.

Formation of the metastable $(Y_{1/3}Ba_{2/3})CuO_{2+\delta}$ phase by mechanical deformation of $YBa_2Cu_3O_{6+\delta}$ powder seems to be straightforward: ball-vial wall and ball-ball collisions introduce defects such as grain boundaries, dislocations and vacancies into the structure. Atomic diffusion proceeds until a complete random mixing is achieved on the cationic sites. The transformation is not unlike an order-disorder transition.

TEM allows one to view the evolution of grain size in a material, but is biased by the fact that only thin samples (such as edges of particles) are available for analysis. As a result, an analysis of peak broadening in the x-ray diffraction patterns give a much more quantitative description of the grain size evolution as a function of milling time. This will be done in section III.C.

### III.A.4 Differential Scanning Calorimetry of the Milled YBa$_2$Cu$_3$O$_{6+\delta}$ Samples

Figure 3.9 shows a DSC trace taken of (Y$_{1/3}$Ba$_{2/3}$)CuO$_{2+\delta}$ powder milled for thirty hours. The scan was done at 20K/min. in an open pan with flowing argon as the purge gas. A single exotherm is observed at about 550°C (with an onset temperature of about 510°C). X-ray diffraction patterns of the YBa$_2$Cu$_3$O$_{6+\delta}$ powder sample annealed to temperatures just before and after the exothermic DSC peak show a decrease in the widths of the Bragg peaks. However, since no change in the relative intensities of the Bragg peaks is observed, the exothermic peak in the DSC scan is probably due to grain growth or recrystallization of the metastable cubic phase (Y$_{1/3}$Ba$_{2/3}$)CuO$_{2+\delta}$. Any ordering of yttrium and barium atoms on their sites would be reflected by a change in the relative intensities of the peaks. Samples milled for longer times (>54 hours) had DSC scans with extremely complicated traces, indicative of the fact that several chemical and/or structural changes were occurring. An x-ray pattern taken after the scan showed complete phase separation into at least three phases. A DSC trace of a sample milled for 54 hours is shown in figure 3.10a and its corresponding diffraction pattern is shown in figure 3.10b.

# DSC of $(Y_{0.33}Ba_{0.67})CuO_{2+\delta}$ Powder

## 20° C/min., flowing Argon
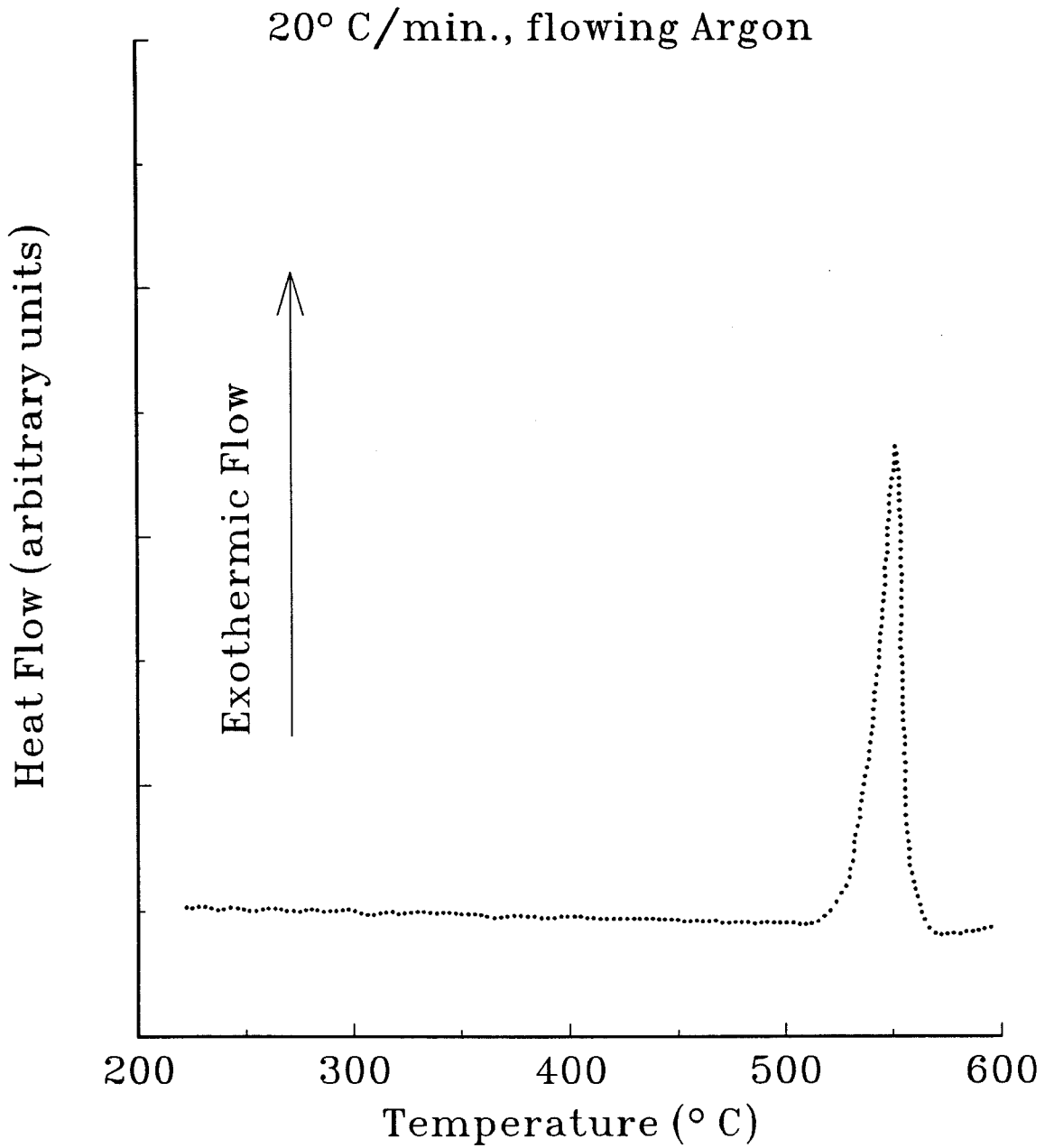


Figure 3.9– DSC trace of the cubic $(Y_{1/3}Ba_{2/3})CuO_{2+\delta}$ phase.

# DSC of $YBa_2Cu_3O_{6+\delta}$ Powder
## Milled for 54 hours



20 ° C/min
Ar atmosphere
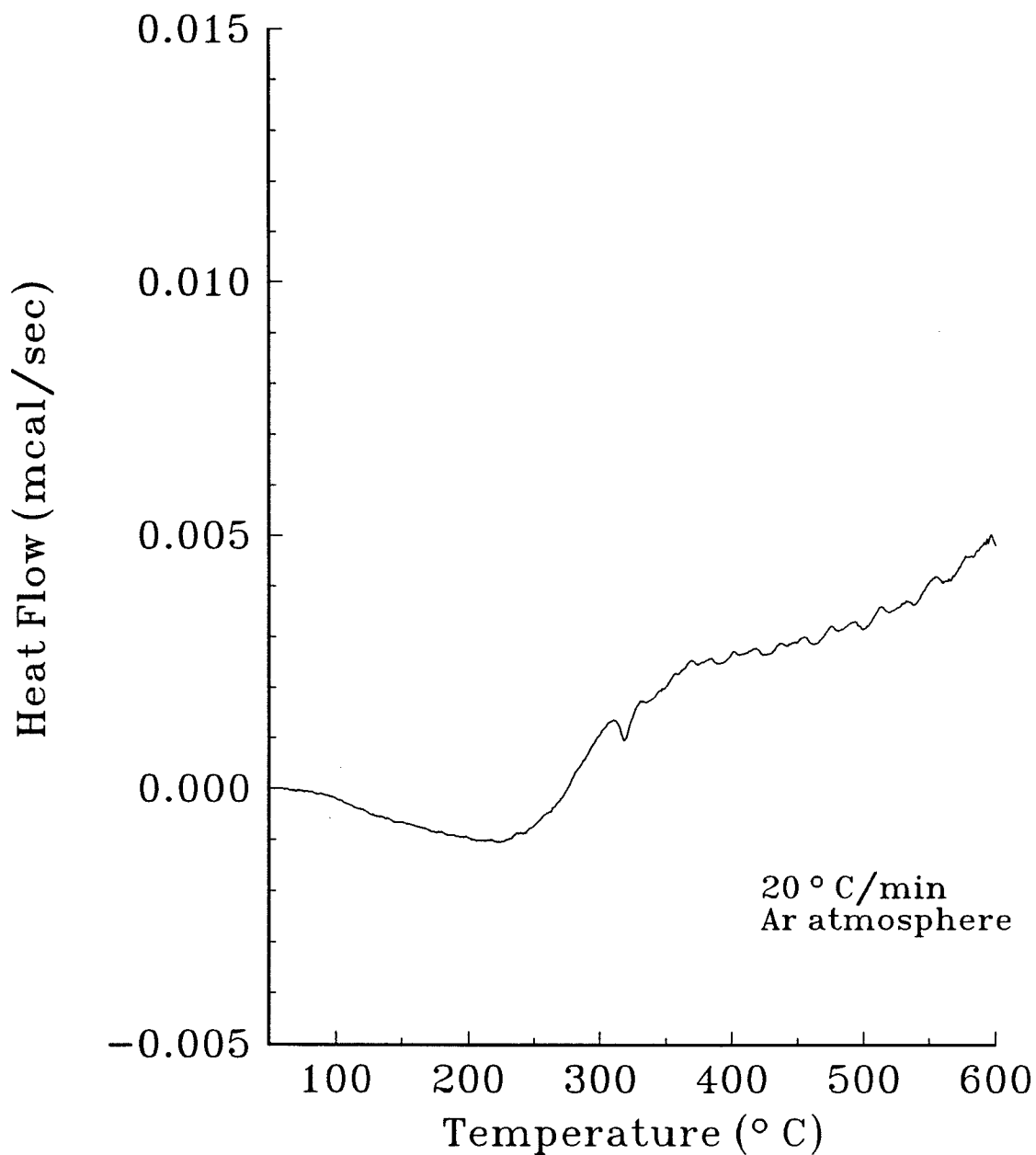
Figure 3.10a– DSC trace of a $YBa_2Cu_3O_{6+\delta}$ sample milled for 54 hours.

## After DSC Scan in Argon Atmosphere
### 54 hour Ball−Milled $YBa_2Cu_3O_{6+\delta}$ Powder
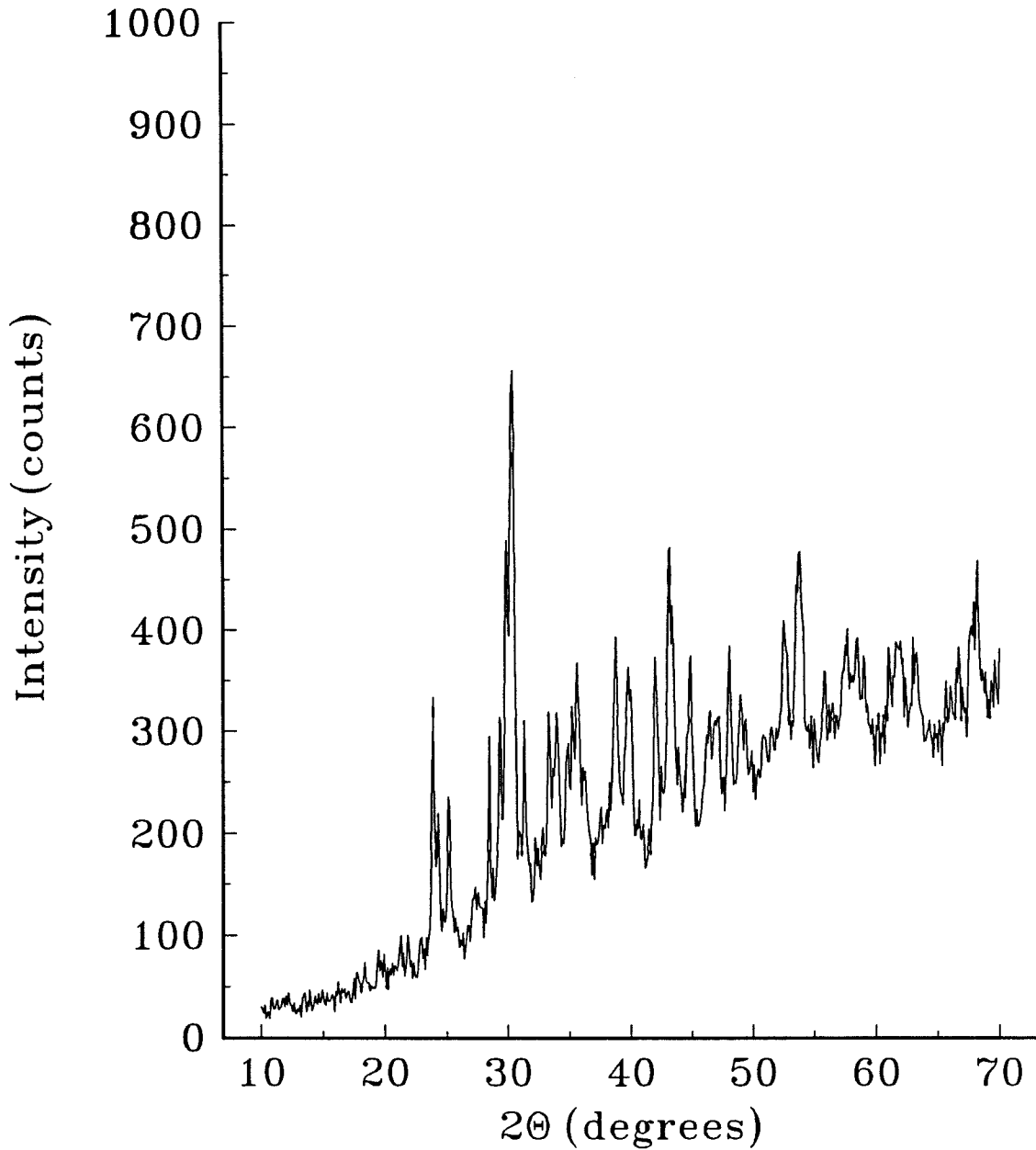


Figure 3.10b− X-ray diffraction pattern of 54 hour sample after DSC.

**III.B    Analysis of the X-ray Diffraction Patterns of Milled Samples**

**III.B.1    Crystallite Size and Lattice Strains from X-ray Line Broadening**

A polycrystalline specimen that is comprised of sufficiently large and strain-free crystallites will in theory give diffraction lines with peak breadths measured in seconds of arc.[10] In reality, a combination of effects arising from instrumental limitations and physical attributes of the specimen broaden this theoretical diffraction line width. Specifically, contributions to the broadening of Bragg peaks from instrumental limitations include the profile of the x-ray source, the flatness of the specimen, the axial divergence of the diffractometer, specimen transparency, the rectangular shape of the receiving slit, and more. From the physical attributes of the specimen, broadening occurs because of contributions from the mean size and distribution of crystallite/grain sizes and the imperfections of the prevailing crystal lattice.

The experimentally measured diffraction profile, h($\varepsilon$), can be considered a convolution of the pure diffraction profile, f($\varepsilon$), and the net broadening profile, g($\varepsilon$):

$$h(\varepsilon) = \int_{-\infty}^{+\infty} g(\eta) \cdot f(\varepsilon - \eta) d\eta. \qquad (3.3)$$

The pure diffraction profile contains broadening contributions from the distribution of crystallite/grain sizes and any lattice imperfections present in the specimen. The net broadening profile contains all the aforementioned instrumental contributions to the peak widths. This function is often called the "instrument function" or "instrument profile," and is unique to a particular diffractometer.

The instrument function can be determined by taking the diffraction pattern of a reference powder that has infinite (say, larger than one micron) grain/particle size and relatively few lattice imperfections. Typically, as was the case for the experiments done

here, silicon powder is used (another common reference powder is alpha quartz). Once the instrument function for the diffractometer has been determined, any additional breadth to the observed diffraction peaks can be attributed to the pure diffraction profile, $f(\varepsilon)$. The instrument profile can be written as either peak breadth as a function of $2\Theta$ – for a rough analysis done directly from the diffraction pattern – or as a set of Fourier coefficients to be deconvoluted from the Fourier transform of the experimentally measured profile.

*III.B.1.a*        *The Method of Warren-Averbach*

In 1950, Warren and Averbach introduced a method to separate the contributions of crystallite size and elastic strain in the diffraction profile.[11] Essentially, their analysis shows that a set of uncorrected Fourier coefficients can be obtained for a diffraction peak by plotting the observed power density against the vertical component of the diffraction vector (by "vertical," they refer to the component of the vector in the (00l') reflection of an orthorhombic unit cell. It is always possible to redefine any set of diffracting planes [hkl] as the [00l'] planes of a new orthorhombic unit cell). Once these coefficients are obtained, the Fourier coefficients for the instrument function can then simply be divided out to obtain the Fourier coefficients for the pure diffraction profile.

Warren and Averbach go on to show that the coefficients of the cosine series are the product of two terms:  the first, $A_n^S$, depends only on the number of equivalent orthorhombic unit cells per column contributing to the diffraction, which is a measure of the crystallite/grain size. The second term, $A_n^D$, depends only on the distortion in the crystallite, and is therefore a distortion coefficient. The cosine coefficient, $A_n$, is given by:

$$\ln A_n = \ln\left( A_n^S \cdot A_n^D \right) \approx \ln A_n^S - 2\pi^2 l^2 \left\langle Z_n^2 \right\rangle, \qquad (3.4)$$

where $Z_n$ is the component of the distortion displacement vector perpendicular to the [00l] reflecting planes. A plot of this function will give the size coefficients as the zero intercepts and a mean-square value for the strain as the initial slope of the line.[12] Therefore, if we plot several orders of (00l), such as (001), (002), (003), etc., the size coefficient will be independent of the order and the distortion coefficient will depend on the order l in such a way as to approach unity as l→0. In practice, for cubic systems, it is only possible to plot the first two orders of any set of diffracting planes because the third order always overlaps with another set of planes of higher multiplicity. For example, the planes have coincident d-spacing with the (221) planes, and the (333) planes are coincident with the (511) planes.

For a cubic system, $d = a/h_0$, where $h_0^2 = h^2 + k^2 + l^2$. Equation (3.4) can be expressed as follows:

$$\ln A_L(h_0) = \ln A_L^S - 2\pi^2 L^2 \frac{h_0^2}{a^2}\langle \varepsilon_L^2 \rangle, \qquad (3.5)$$

where the equivalent orthorhombic cell has been converted back to the real cubic cell of the specimen.

Appendix A contains the programs written in MathCAD™ for Windows™ (version 3.1) that were used to do this analysis. Also discussed in the appendix is the modified Rachinger correction used to strip $K_{\alpha 2}$ scatter from the diffraction pattern. First, a Rachinger correction was applied, then the background was removed from the pattern, then the Fourier analysis was performed.

The main drawback of this particular approach to Bragg peak analysis is that it is almost as much an art as it is an algorithm. It is extremely difficult to choose the starting and ending points for a given peak. The tails of the peaks contain the information that gives this technique its power (because the higher intensity center portion of the peak looks like a peak no matter what function one uses to describe it – Lorentzian, Gaussian,

Voight, etc). Thus, choosing the starting and ending points for the peak often corresponds to choosing a shape for the peak. Cut the tails off and the peak resembles a Gaussian (and its Fourier coefficients will reflect this), extend it too far and the peak resembles a Lorentzian. Because of this, one often uses the Warren-Averbach analysis as a check for the consistency of the method of integral breadths.

### *III.B.1.b*        *Size and Strain Directly from Peak Widths*

It is possible to estimate both crystallite size and strain by analyzing the Bragg peaks without resorting to a Fourier analysis. In order to do this, it is necessary to make an assumption about the shapes of the two contributing line profiles. Typically, the contributions are assumed to be either Gaussian or Cauchy in form. Klug and Alexander state an empirical observation that strain broadening can often be approximated by a Gaussian function and that crystallite size broadening can often be approximated by a Cauchy profile.[13] Equations for peak breadth dependence on 2Θ can be developed for each of the possible relationships: Cauchy/Cauchy, Gaussian/Gaussian, or Cauchy/Gaussian size/strain distributions. A plot of peak breadth against $s = \dfrac{2\sin\theta}{\lambda}$ will show a straight line for Cauchy/Cauchy broadening, a parabola for Gaussian/Gaussian broadening, and an intermediate curve for Cauchy/Gaussian broadening. A program to perform this analysis was written in MathCAD™ for Windows™ and is also included in the Appendix, with a more detailed explanation. The most comprehensive explanation for this approach is given by Klug and Alexander.[14] This method is known as the *method of integral breadths* (where we have adapted the equations to use FWHM).

## III.B.2    Instrument Function for High Temperature X-ray Diffractometer

Shown in figure 3.11 is the instrument function for the high-temperature x-ray diffractometer plotted against detection angle. An x-ray diffraction pattern was taken of reference silicon powder for this analysis. The function is a smooth, very slowly varying function of $2\Theta$. Each Bragg peak was fitted to either a Lorentzian or Gaussian peak shape to determine its full width at half maximum. Note that there is basically no gain in resolution by going to a smaller receiving slit. This can be attributed to the $1°$ source slit used to gain intensity at the detector. A $1°$ source slit allows axially divergent x-rays to scatter off areas of the flat specimen and still reach the detector.

Figure 3.12 shows the instrument function for the Hi-T XRD as a set of Fourier coefficients. In this case, the peaks were first smoothed by a cubic spline interpolation and then transformed and normalized to the first coefficient. Writing the instrument profile in this way offers two advantages: first, a peak shape is not assumed as is done in the other method, and second, these coefficients can be divided out of the experimental profile to determine the pure diffraction profile. The Fourier coefficients from the silicon reference powder were linearly interpolated to determine their values at the specimen's Bragg peak. This is not necessarily valid because, as shown in the figure, the coefficients are not a slowly varying function of angle over the entire range. There is a dip in their values at about $2\Theta \approx 70°$. The origin of this dip has not been determined, but it is likely that the sample is slightly eucentric from the true axis of the focussing circle. This has no adverse effect on the determination of d-spacings because a Nelson-Reilly extrapolation was done for all such calculations. The Warren-Averbach technique was nonetheless used only for consistency checks.

### III.B.3    Instrument Function for the Inel 120° Diffractometer

When a similar analysis was performed on the Inel 120° diffractometer a sharp change in the FWHM as a function of angle was found.  This occurs from 65°–90° in 2Θ, making an interpolation of instrumental peak breadths in that angular range highly suspect.
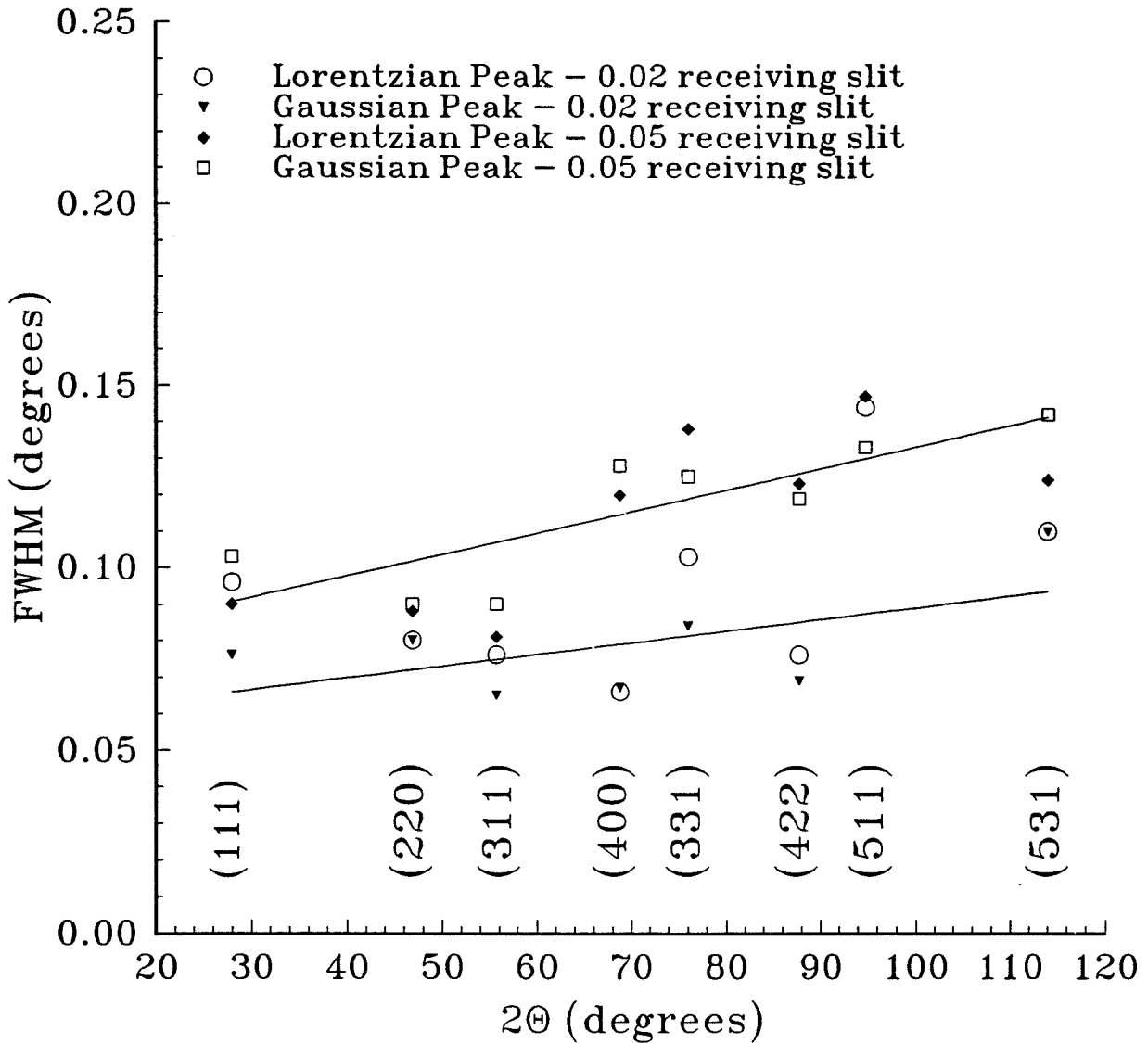
Figure 3.11– Instrument function for the high temperature x-ray diffractometer in terms of FWHM as a function of 2Θ.

# Hi−T XRD Fourier Coefficients
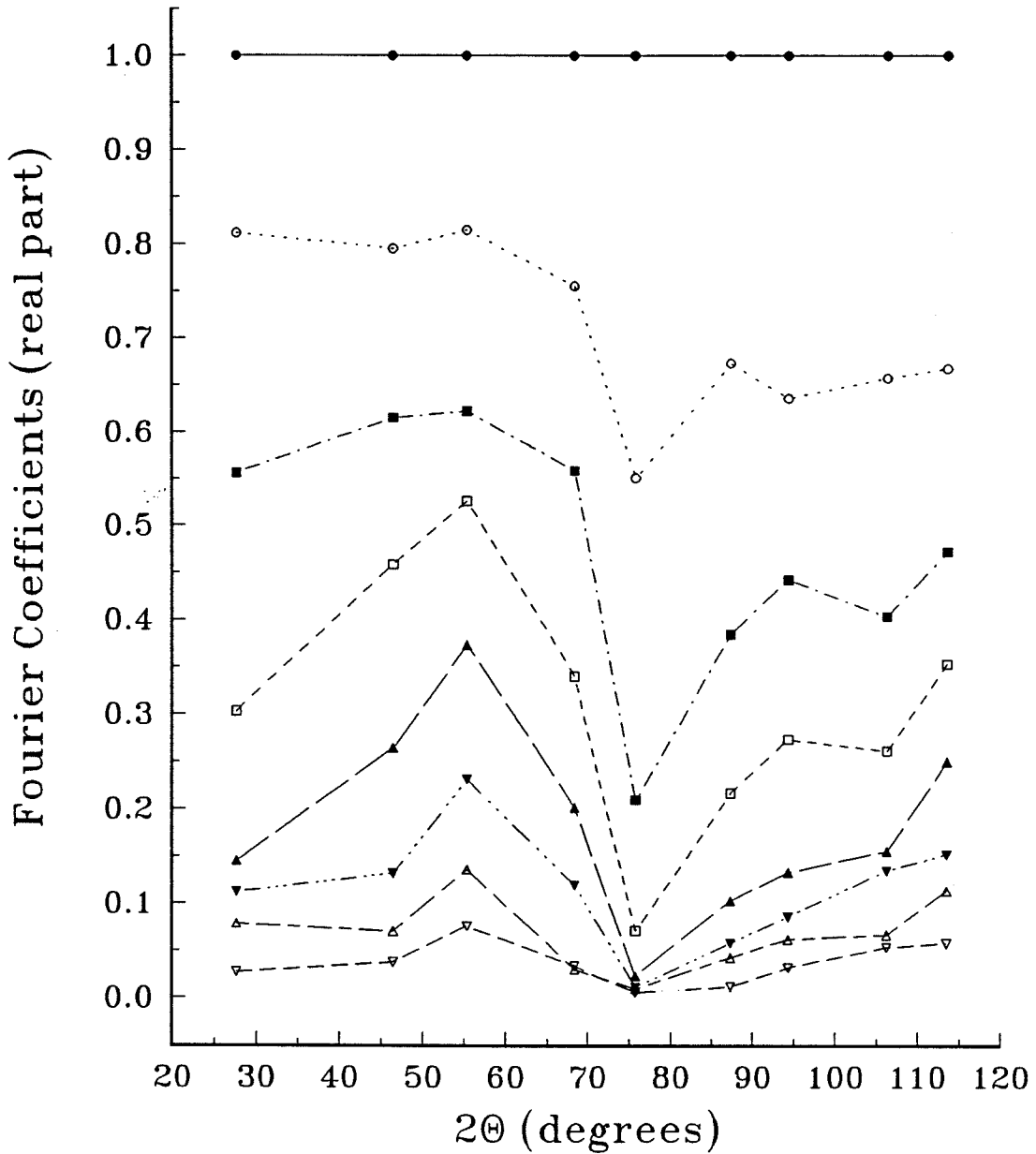


Figure 3.12– Instrument function for the high temperature x-ray diffractometer in terms of its Fourier coefficients as a function of 2Θ. Writing the function in this manner allows a simple Stokes type correction to the experimental profile.

Figure 3.13 offers some insight into why this may be the case: the effective stepsize of the Inel diffractometer as a function of $2\Theta$ varies across angular range. Because the Inel is not a $\Theta-2\Theta$ diffractometer, it does not have a true "step size" (i.e., a particular angular resolution at which its detector moves on the diffraction circle). One can only define an "effective step size," which is some function of the deviation of its curved anode from a perfect circle and the positioning of the parallel detection diodes behind it. Essentially, the Inel detector does not coincide perfectly with the measuring circle of a true $\Theta-2\Theta$ diffractometer. As can be seen from the graph, this function does not have a simple dependence on angle. It is believed that this is the reason for the non-systematic behavior of the FWHM of the reference Bragg peaks on $2\Theta$.

The Fourier coefficients as a function of $2\Theta$ are shown in figure 3.14. The dip in stepsize through 65°–90° shows up as a local minimum in the higher order Fourier coefficients. However, the higher order coefficients are not used in the analysis.

# Step Size of the Blue Inel Diffractometer

## incident angle of 15°
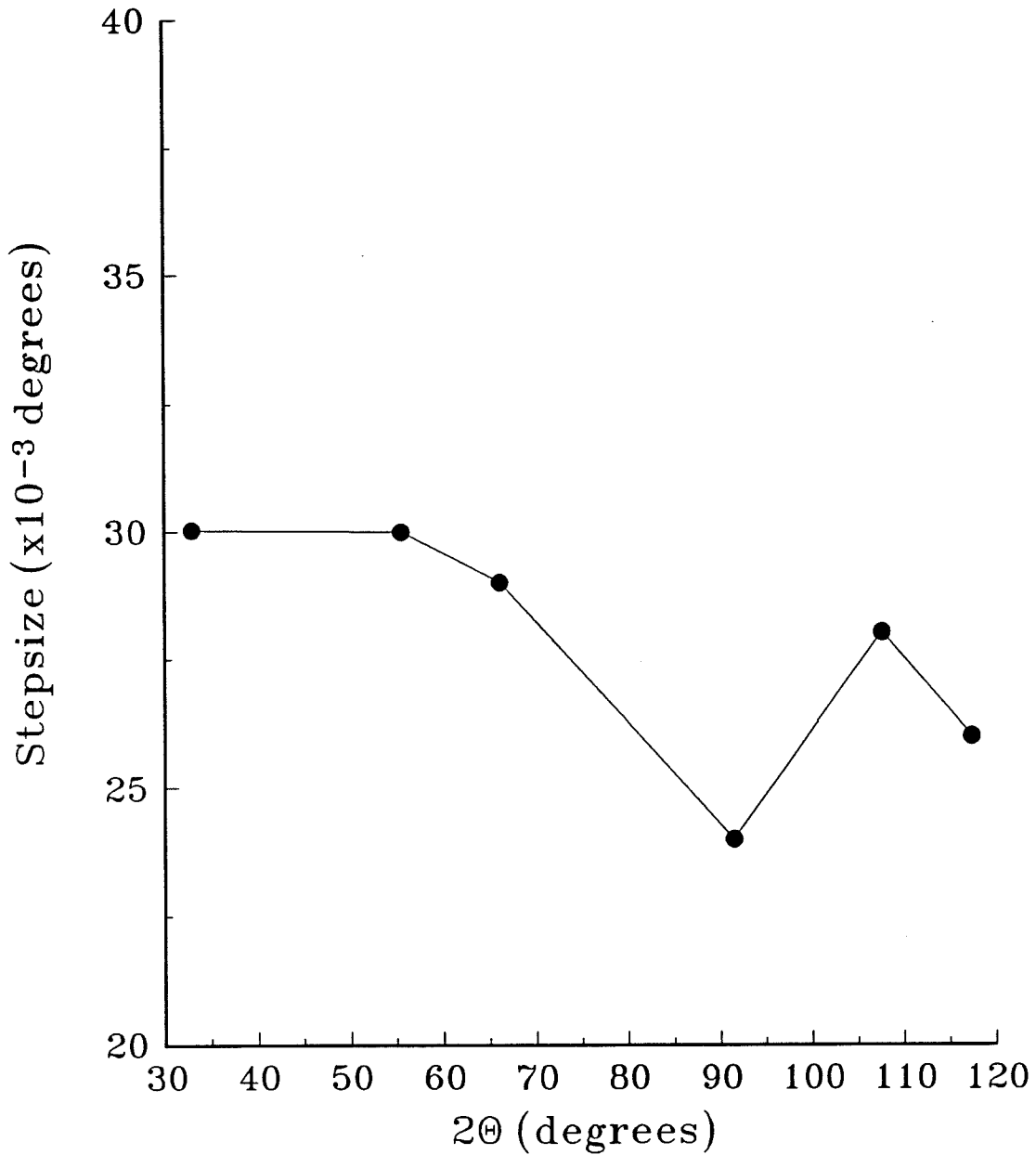


Figure 3.13– Effective step size of the Inel over its angular range.

# Blue Inel Fourier Coefficients
## incident angle of 15°
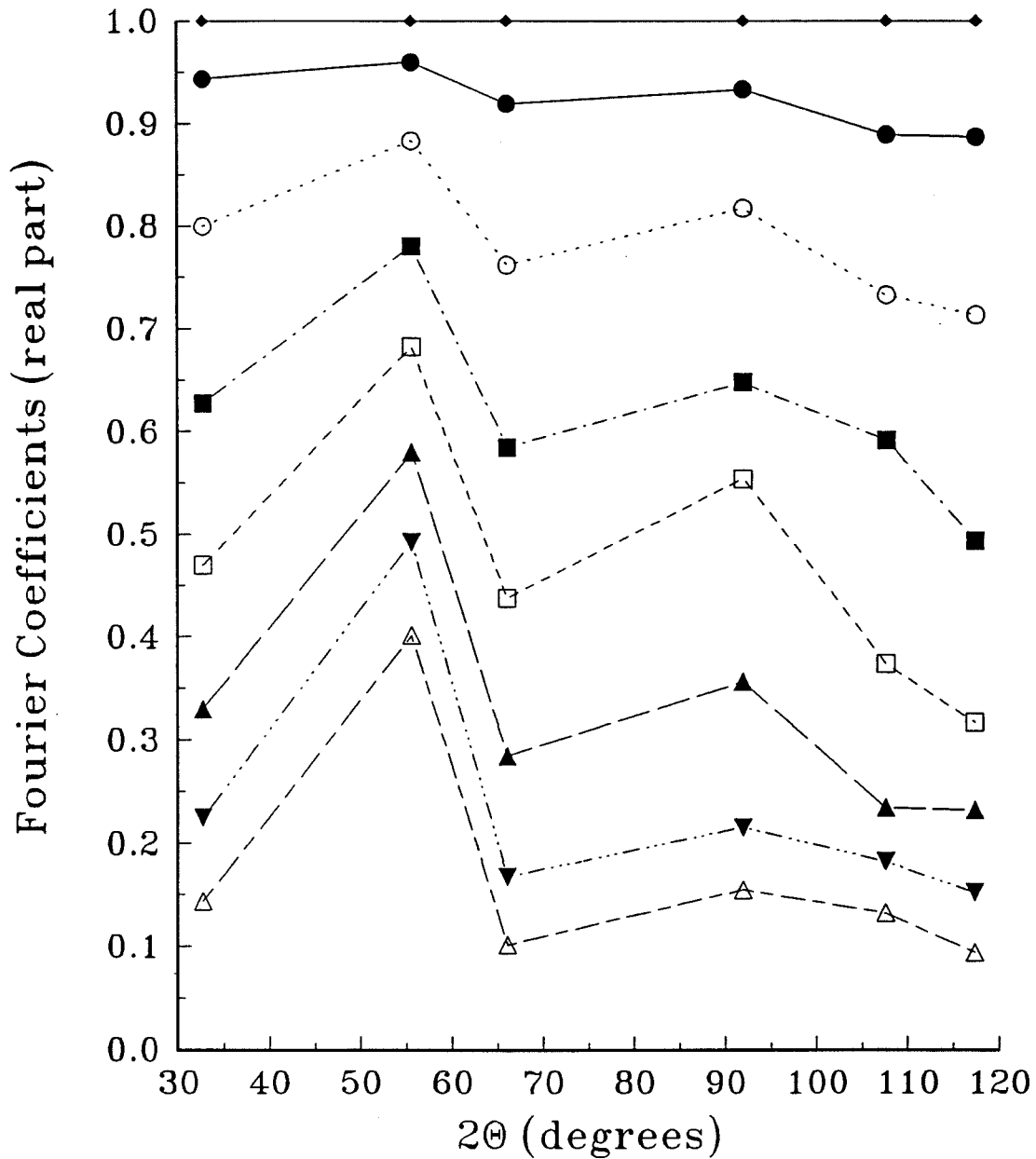


Figure 3.14– Instrument function for the INEL in terms of its Fourier coefficients. Writing the function in this manner allows a simple Stokes type correction to the experimental profile.

### III.B.4    Analysis of $(Y_{1/3}Ba_{2/3})CuO_{2+\delta}$ Powders

The analysis of the metastable $(Y_{1/3}Ba_{2/3})CuO_{2+\delta}$ powders presented a difficulty in that no reference peaks were available for comparison. Ideally, the specimen to be studied is available in large, strain-free crystallites for direct comparison of peaks. The analysis is made more complex when there is an overall expansion or contraction of the lattice, which shifts the peaks in addition to broadening them. If the Stokes correction is made using the same origin for the broadened and standard peaks, this expansion will be included as part of an asymmetric strain. On the other hand, if separate origins are chosen for the experimental and pure diffraction profiles, a smaller mean-square strain is obtained. In this case, the average lattice expansion is gotten directly from the shift of peak positions and the mean-square strain is relative to the new average lattice parameter. Both procedures are correct but they give different quantities. In general, the second procedure is used since it simplifies the calculations considerably and either result can be obtained approximately from the other.

In the case of the metastable $(Y_{1/3}Ba_{2/3})CuO_{2+\delta}$ powders, we cannot define a standard lattice size. As a result, we choose the latter approach and make the centers of the experimental peaks and the "pure profile" peaks coincident. An argument (albeit a weak one) can be made in support of this approach: TEM showed that there was a tremendous decrease in grain size during the first hour of ball-milling. Therefore, we might guess that most of the broadening in the Bragg peaks is a size effect and not a strain effect. In reality, the Warren-Averbach analysis was used primarily to check the results of the method of integral breadths.

Figure 3.15 shows the grain size as a function of milling time. The grain size drops exponentially during the first hours of milling before tailing off at longer times. It then remains relatively constant until phase decomposition sets in. The starting grain size of the material is one micron. After just one hour of milling, the grain size has been reduced to less than 50 nm. After 30 hours of milling, the grain size has only decreased to 10 nm. These numbers are consistent with what was seen by TEM. The exponential decrease in grain size is characteristic of ball-milled powders.[15] Mean-square strain as a function of milling time is not shown because the results obtained by the two methods of analysis were not consistent. The values gotten were highly suspect because it was very difficult to define where a particular Bragg peak ended and where the high background began. The background for the milled samples was extremely high owing to the diffuse scattering typical of defective samples. The diffuse background arises from a number of effects, including short-range ordering, atomic size effects, Compton scattering, thermal diffuse scattering and Huang scattering. The reader is referred to Warren's book for a detailed explanation.[16]

The only consistency in strain determination between the Warren-Averbach method and the method of integral breadths was that the magnitude of the strain was extremely small (all values were less than 0.05%). The conclusion that can be drawn is that the brittle material can accomodate very little strain energy. Rather, the material fractures and shears, reducing its grain size until phase decomposition sets in.

# Grain Size versus Milling Time
## $YBa_2Cu_3O_{6+\delta}$ Powder
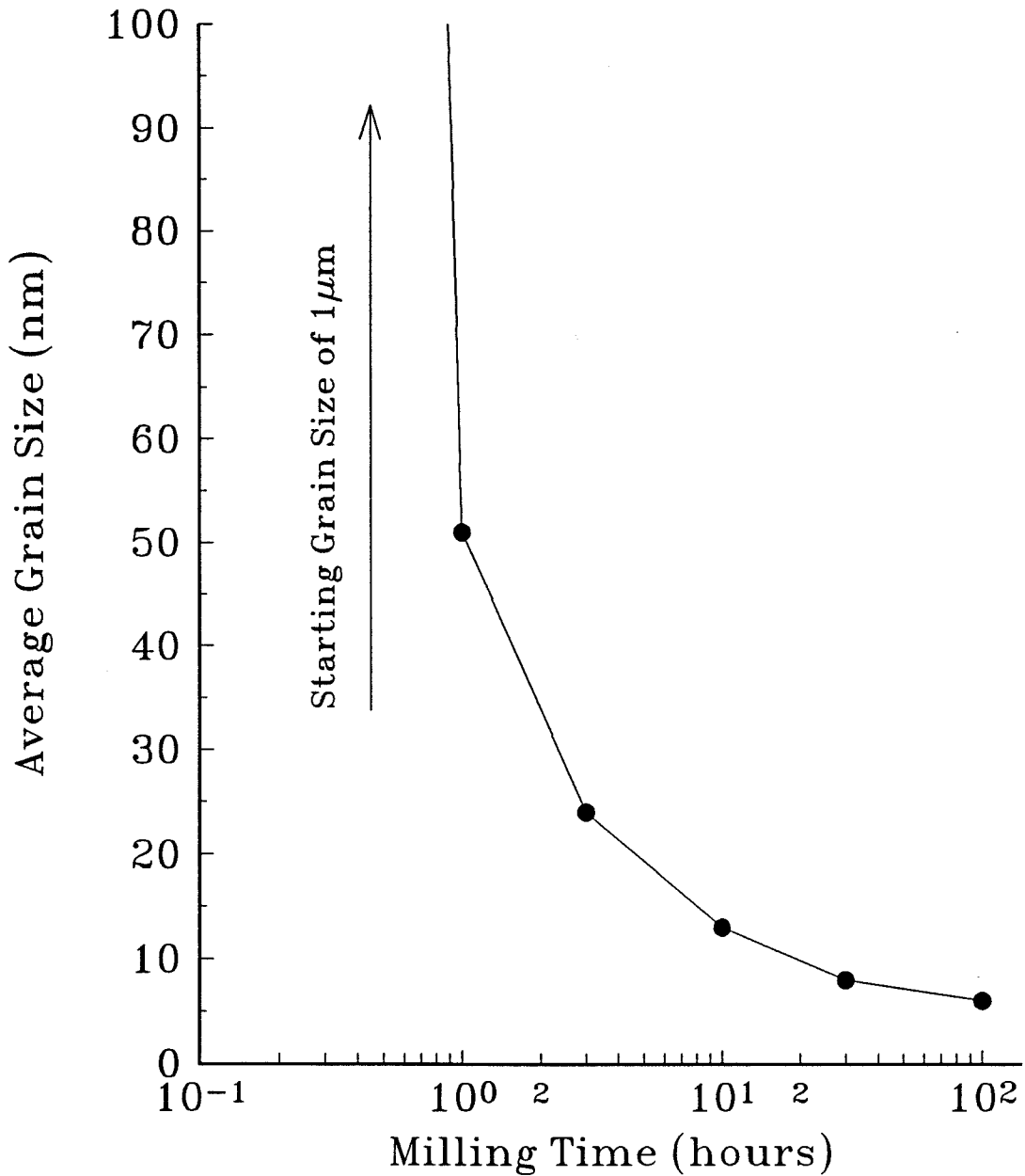


Figure 3.15– Grain size as a function of milling time for $(Y_{1/3}Ba_{2/3})CuO_{2+\delta}$.

### III.C   Formation and Stability of the $(Y_{1/3}Ba_{2/3})CuO_{2+\delta}$ Phase

The repeated high energy impacts associated with the milling process produce large amounts of structural defects in the $YBa_2Cu_3O_{6+\delta}$ powder. Defects such as grain boundaries, dislocations and vacancies are introduced on the oxygen sublattice and cationic sites. As a result of this, atomic diffusion proceeds until a completely random state is attained; the oxygen sublattice is disordered with little or no loss of oxygen and the cationic sites display no ordering of yttrium and barium atoms. After just one hour of milling, the powder Bragg peaks are broadened sufficiently to make discrimination of orthorhombic splitting impossible by x-ray diffraction. However, based on the studies done in chapter 2, one can assume that the disordering on the oxygen sublattice occurs before the disordering on the cationic sites. The second disordering process produces a metastable cubic phase with the formula $(Y_{1/3}Ba_{2/3})CuO_{2+\delta}$. It takes more than ten hours to achieve this randomized state. Even after 100 hours of ball milling, the compound does not amorphize. Rather, after thirty hours of ball milling, phase decomposition of the metastable cubic $(Y_{1/3}Ba_{2/3})CuO_{2+\delta}$ begins to occur. Ultimately, the compound decomposes into a mixture of $Y_2O_3$ and nanocrystalline $BaCuO_2$.

Further annealing of the metastable $(Y_{1/3}Ba_{2/3})CuO_{2+\delta}$ phase has an interesting effect on the structure. A sample of cubic $(Y_{1/3}Ba_{2/3})CuO_{2+\delta}$ was annealed *in situ* in the high temperature x-ray diffractometer at 420°C and 133 mbar of oxygen. The impetus for such an annealing treatment was twofold: first, to see if the cubic phase would change its lattice parameter by either incorporating or evolving oxygen (recall that at this pressure and temperature, tetragonal $YBa_2Cu_3O_{6+\delta}$ would take on oxygen to become orthorhombic), and second, to see if the Bragg peaks associated with the cubic phase would sharpen from either grain growth or strain relief. Unexpectedly, a new phase (or possibly two new phases) were formed. This phase, which is not yet identified, was found to exist only when the annealing treatment used temperatures in the range of

~400°C–600°C and pressures greater than ~100mbar of oxygen. Higher temperatures and/or lower pressures of oxygen produced the expected phase separation into $Y_2O_3$ and $BaCuO_2$.

The diffraction pattern from this phase (or, "these phases") is shown in figure 3.16. Notice that the peaks are extremely sharp, indicating significant growth of crystallite/grain size and strain-relief. Of the eight major peaks seen, seven of them can be indexed successfully to a cubic unit cell with a lattice parameter of a= 5.469Å. The other peak does not index correctly to this scheme. The remaining peak may correspond to one of the peaks in $Y_2O_3$, $BaCuO_2$, $Y_2Cu_2O_5$, $BaO$, $Cu_2O$ or $CuO$. A strong indication that the unindexed peak is not of the same phase is the fact that when the temperature and/or partial pressure of oxygen is varied, the intensity of the peaks varies much more radically than the seven peaks of the cubic phase. Interestingly, the lattice constant of this new, secondary cubic phase is almost exactly $\sqrt{2} \cdot 3.86\text{Å} = 5.46\text{Å}$, which is the face diagonal of the first cubic phase. It is possible that this phase is a further rearrangement of the first cubic phase. At this relatively low temperature, it is not likely that the cations moved significantly. Recall that x-ray diffraction of cubic $(Y_{1/3}Ba_{2/3})CuO_{2+\delta}$ before and after its exothermic DSC peak showed no signs of cationic ordering. However, for this new phase to be a newly ordered cubic phase with its lattice based on the face diagonal of the $(Y_{1/3}Ba_{2/3})CuO_{2+\delta}$ phase, a stretching along one axis would have to occur; if this did not happen, the second cubic phase would be tetragonal, with a c-axis shorter than the a-axis. Initial attempts to index these peaks to a tetragonal unit cell were not successful. Finally, it was found that this second cubic phase decomposes when exposed to air. As a result, it was not possible to perform thermoanalytic measurements on the phase (measurements such as DSC or TGA, for example). Work continues on the identification and characterization of this phase.

# Second Cubic Phase
## 160 mbar $O_2$, 410° C
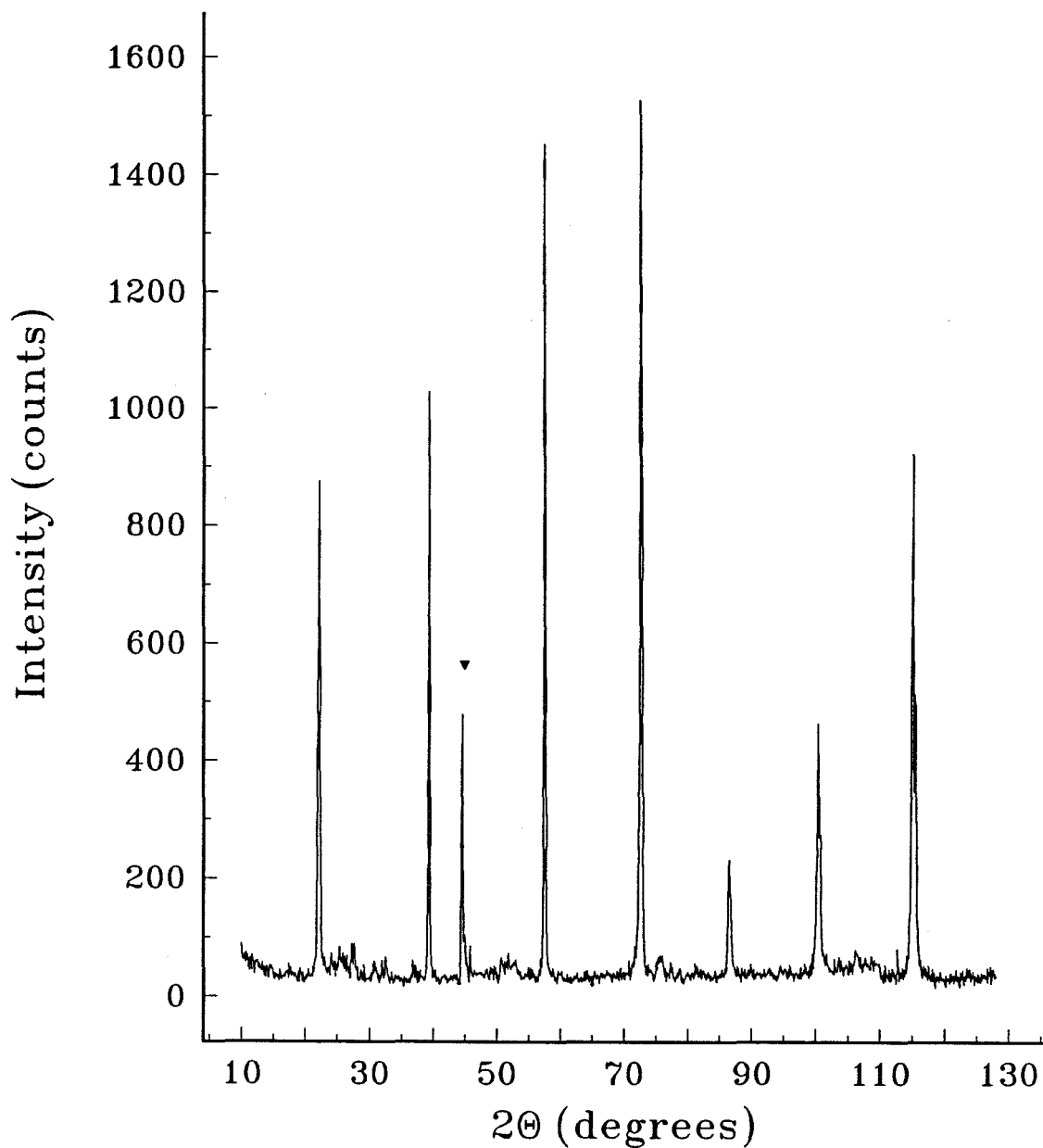


Figure 3.16– A secondary cubic phase that results from further annealing of the cubic $(Y_{1/3}Ba_{2/3})CuO_{2+\delta}$ phase. The marked peak does not index properly to the proposed cubic phase.

# REFERENCES FOR CHAPTER 3

[1] see section II.A for a more detailed discussion of this phase transition.

[2] B. P. Bardes, ed., *Metals Handbook, 9th edition, vol. 1* (American Society for Metals, 1983), p. 512.

[3] R. F. Cook, T. M. Shaw and P. R. Duncombe, Adv. Cer. Mat. **2(3B)** (1987), p. 606.

[4] ibid.

[5] Tarascon, Barboux, Micelli, Greene, Hull, Eibschutz and Sunshine, Phys. Rev. B **37** (1988), p. 7458.

[6] see II.D.1 for details.

[7] private communication, H. Ouyang.

[8] Z. Q. Gao and B. T. Fultz, Technical Note #1, Keck Laboratory for Engineering Materials (1991).

[9] R. Schulz, private communication.

[10] It is the slight deviations from this theoretical peak width that is studied using an x-ray diffraction technique known as "x-ray rocking curve analysis," where an infinite crystal (i.e., macroscopically large) is rocked around a particular k-space orientation. Scattering intensities in different directions are then indicative of particular types of the lattice defects present and their orientation in the crystal.

[11] Warren and Averbach, J. Appl. Phys. **21** (1950), p. 595.

[12] A far better and more thorough explanation is offered in the following reference: Klug and Alexander, X-ray Diffraction Procedures, John Wiley & Sons (New York : 1974). See chapter 9.

[13] ibid., Klug and Alexander, p. 662.

[14]ibid., Klug and Alexander, p. 664.

[15]J. S. Benjamin and T. E. Volin, Met. Trans. A **5** (1974), p. 1929.

[16]B. E. Warren, X-Ray Diffraction, Dover Publications (New York : 1990), p. 151-245.

# IV.  Summary of Findings

## IV.A   Summary of Findings on the Orthorhombic–Tetragonal Transition

We have studied the order–disorder transition that occurs on the oxygen sublattice in $YBa_2Cu_3O_{6+\delta}$ with several different techniques to measure various thermodynamic quantities associated with the transition.  We began by measuring pressure-concentration isotherms for the material, where we found no evidence for a misciblility gap in the range of 450°C to 750°C in temperature and 1 mbar to 1013 bar partial pressure of oxygen.  It is still possible that a miscibility gap exists below this temperature range, where the kinetics of oxygen uptake and evolution are so slow as to make the experimental measurement of pressure-concentration isotherms unreasonably time-consuming.

The pressure-concentration isotherms were then converted to a chemical potential in the solid by assuming that the gaseous oxygen was allowed to come to equilibrium with the solid.  An expression for the chemical potential in the solid was then written in such a way as to emphasize its deviation from a random solid solution.  As oxygen is incorporated into the solid, the atoms selectively occupy one of two available sites in the basal CuO plane.  Because of this, it is not surprising that the excess entropy associated with the transition is always less than the entropy of ideal mixing and is particularly so in the orthorhombic phase.  Excess enthalpy and chemical potential were also calculated.  It is postulated that the order–disorder transition is of the λ–type, although this was not directly observable by the techniques used, which necessarily averaged quantities over temperature for a given oxygen content.  However, Gerdanian, Picard and Marucco[1] were able to measure excess enthalpies and entropies as a function of oxygen content at fixed temperatures using a thermobalance in conjunction with a microcalorimeter.  They have

shown that the transition is of the λ–type. A comparison shows that our data is not inconsistent with this interpretation.

X-ray diffraction using a high-resolution, high temperature diffractometer capable of high vacuum allowed us to examine *in situ* various points on the pressure-concentration isotherms; this allowed determination of the orthorhombic–tetragonal phase line (again, no miscibility gap was found). An experiment in which constant stoichiometry cooling of $YBa_2Cu_3O_{6+\delta}$ powders was executed in the diffractometer was done to determine the room temperature lattice parameters as a function of oxygen content. It was found that there were three distinct regimes: a tetragonal regime for $\delta \leq 0.35$, an orthorhombic regime in which $a<b<c/3$ for $0.35 \leq \delta \leq 0.8$, and an orthorhombic regime in which $a<b=c/3$ for $\delta \geq 0.8$. It is postulated that the intermediate orthorhombic regime is the Ortho II phase as seen by TEM and predicted by computer simulations. Finally, the high temperature x-ray diffraction unit was used to determine the thermal expansion of the tetragonal phase. This was found the be linear with:

$$\frac{\Delta a}{a} = 1.1 \times 10^{-5} \ /^{\circ}C$$

$$\frac{\Delta c}{c} = 1.6 \times 10^{-4} \ /^{\circ}C.$$

Differential scanning calorimetry was done in inert and oxygen atmospheres to determine the enthalpies and activation energies associated with the transition. It was found that a Kissinger analysis holds for the endothermic peak observed; however, it was concluded that the peak was most likely due to the evolution of oxygen from the sample, rather than the disordering of oxygen atoms on their sublattice. Attempts to seal the DSC sample pan, and thus keep the chemical potential of oxygen in the solid constant were unsuccessful; when a small enough amount of sample was used to prevent the mechanical failure of the pan, no signal was observable. Nonetheless, the enthalpy associated with the

evolution of oxygen from the sample coupled with any small contribution from the disordering of oxygen atoms on their sublattice was found to be 5.2 kJ/mol in Argon, 2.0 kJ/mol in a 16% oxygen mixture and 1.7 kJ/mol in pure oxygen. The activation energy assiciated with oxygen evolution was found to be 1.2 eV/atom in Argon, 1.8 eV/atom in 16% oxygen and 2.9 eV/atom in pure oxygen.

## IV.B    Summary of Findings on the Mechanical Milling of $YBa_2Cu_3O_{6+\delta}$

Ball milling of $YBa_2Cu_3O_{6+\delta}$ powders produces a metastable cubic phase identified as $(Y_{1/3}Ba_{2/3})CuO_{2+\delta}$. The unit cell of the metastable cubic phase is a perovskite structure with the yttrium and barium atoms occupying the body-centered position in a statistical ratio of 1:2. Copper atoms occupy the vertices and oxygens are placed at the edge bisectors (approximately). Within the first hour, the grain size decreases exponentially and then holds constant at 10Å. It is likely that a disordering of the oxygens on their sublattice occurs within this first hour of milling. A second disordering of the cations occurs after ten hours of milling. This disorder gives rise to the cubic phase. After more than thirty hours of milling, the cubic phase begins to decompose into its constituent oxides. After 100 hours of milling, most of the material has separated into $Y_2O_3$ and $BaCuO_2$. Further annealing of the $(Y_{1/3}Ba_{2/3})CuO_{2+\delta}$ phase in low oxygen pressures (~100 mbar) and moderate temperatures (400–600°C) produces a mixture of two phases, the more substantial of which indexes to a different cubic cell with lattice constant a= 5.47Å.

# REFERENCE FOR CHAPTER 4

[1]op. cit., Gerdanian, Picard and Marucco.

# Appendix A:      Diffraction Analysis Algorithms and Programs

This appendix contains the various x-ray diffraction analysis programs that were written. Included are a modified Rachinger-type $K\alpha_2$ stripping routine, an FFT transformation routine and a cubic spline interpolation scheme that increased the number of points to the nearest power of two larger than the original number of data points. This was done to allow the use of a Cooley-Tukey type butterfly FFT algorithm. Also included is a method of integral breadth routine for calculating the size/strain directly from peak widths. Details of the inner workings of the programs are included in the program comments.

## K-alpha2 Stripping Document

This document removes the K-alpha2 portion from an x-ray scan. The algorithm is a Rachinger-type correction with an automatic calculation of the variable "lag." "Lag" is the number of steps between the k-alpha1 and k-alpha2 peaks. The variable is calculated to be the nearest integer such that the spacing between the peaks in two theta divided by the lag is most nearly the step size of the scan:
i.e., (del2theta/lag) ~ stepsize. This minimizes the high angle noise in the calculation.

Written by **David S. Lee**, April, 1992.

$ORIGIN \equiv 1$

fin     fout

$xrdat := READPRN(fin)$

$npts := rows(xrdat)$

Zero the various matrix elements for the upcoming calculation.

$j := 1 .. npts$

$Intens_{j,2} := 0$

$Intens^{<1>} := xrdat^{<1>}$    <<======= Make the first column of "Intens" equal to the angle. "Intens" holds the K-alpha1 intensities after the calculation.

Input the K-alpha1 and K-alpha2 wavelengths for the radiation used (in Angstroms).

$alpha1 := 1.788965$       $alpha2 := 1.792850$

Input the step size used for the scan.

$$stepsize := \frac{\left(xrdat_{npts,1} - xrdat_{1,1}\right)}{npts - 1}$$      $stepsize := 0.029$

Calculate the fractional wavelength shift in degrees.

$$\text{lambfrac} := \frac{(\text{alpha2} - \text{alpha1})}{\text{alpha1}} \cdot \frac{360}{\pi}$$

$$i := 1 .. \text{npts}$$

$$\text{del2theta}_i := \text{lambfrac} \cdot \tan\left(\frac{\pi}{360} \cdot \text{xrdat}_{i,1}\right)$$

$$y_i := \frac{\text{del2theta}_i}{\text{stepsize}}$$

$$\text{lag}_i := \text{if}\left(\text{mod}\left(y_i, 1\right) < \frac{1}{2}, \text{floor}\left(y_i\right), \text{ceil}\left(y_i\right)\right)$$

$$\text{Intens}_{i,2} := \text{if}\left[\text{lag}_i - i \geq 0, \text{xrdat}_{i,2}, \text{xrdat}_{i,2} - \left[0.5 \cdot \text{Intens}_{\left(i - \text{lag}_i\right),2}\right]\right]$$

$$\text{WRITEPRN}(\text{fout}) := \text{Intens} \qquad \text{rows}(\text{Intens}) =$$
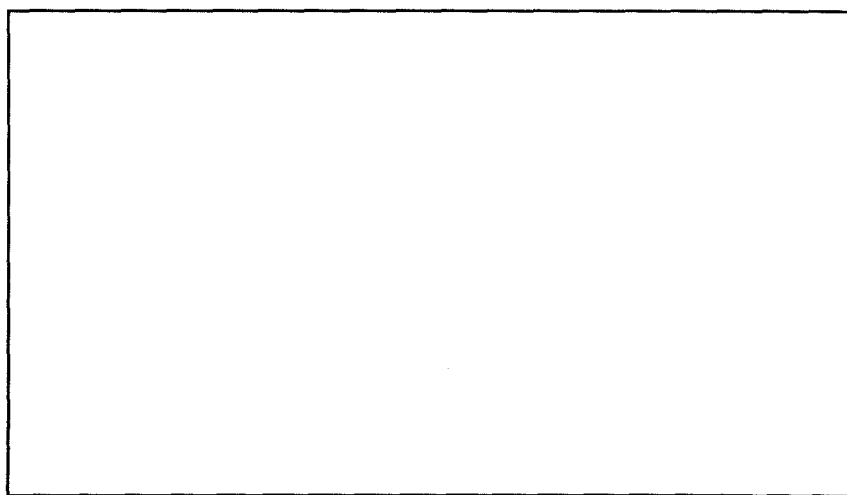
$$\text{cols}(\text{Intens}) =$$

The data is written to a file containing two columns - the first column is angle in degrees and the second column is stripped intensity. The columns are in the same units as the original data file (usually two theta and counts). A graph of the original scan (dotted line) and the stripped scan follows on the next page of this document.

stepsize =

## Spline Interpolation & Frequency Analysis Document - David S. Lee, 4/92.

This program will spline interpolate to make the total number of data points to be transformed equal to the first power of two that is greater than the number of data points. For example, if you have 379 points in the data file, the program will interpolate and extra 133 points to bring the total to 512. This allows MathCAD to use a much faster Cooley-Tookey type butterfly FFT in other documents that deconvolute instrument functions, calculate grain size and strain, etc. The spline interpolation assumes that the slope at both ends of the peak goes to zero.

$$\text{ORIGIN} \equiv 1$$

$$\text{xrstrip} := \text{READPRN}(\text{fin})$$

$$\text{xrangle} := \text{xrstrip}^{<2>} \qquad\qquad \text{xrint} := \text{xrstrip}^{<3>}$$

Remove the Lorentz-Polarization factor from the spectrum.

$$\text{xrcount} := \frac{\overrightarrow{\dfrac{\text{xrint}}{1 + \left(\cos\left(\text{xrangle}\cdot\dfrac{\pi}{180}\right)\right)^2}}}{\sin\left(\text{xrangle}\cdot\dfrac{\pi}{360}\right)^2 \cdot \cos\left(\text{xrangle}\cdot\dfrac{\pi}{360}\right)}$$

Figure out the limits for the graph...

$$\text{top} := \max(\text{xrcount}) \qquad\qquad \text{graftop} := 1.05\cdot\text{top}$$

$$\text{bottom} := \text{if}(\min(\text{xrcount})<0, 1.05\cdot\min(\text{xrcount}), 0)$$

Figure out the number of points in the splined data vectors.

$$\text{npts} := \text{rows}(\text{xrstrip})$$

$$\text{log2npts} := \frac{\ln(\text{npts})}{\ln(2)}$$

$$\text{power} := \text{if}(\text{mod}(\text{log2npts}, 1)=0, (\text{log2npts} + 1), \text{ceil}(\text{log2npts}))$$

$$\text{Qpts} := 2^{\text{power}}$$

Below is a declaration/initialization of the data vectors and transformation arrays. The data vectors are then filled with the spline interpolation. Also declared are two temporary arrays used for the spline interpolation, "temp" and "tempang."

$i := 1 .. Qpts$

$Q_{i,2} := 0$ $\qquad$ $xr2count_i := 0$ $\qquad$ $xr2angle_i := 0$

$temp_i := 0$ $\qquad$ $tempang_i := 0$

The vector "vs" is a vector containing the second derivative information for the cubic spline interpolation. It is used by the function "cspline" for later interpolation.

$vs := cspline(xrangle, xrcount)$

Calculate the step size for the splined data.

$$step := \frac{\left(xrangle_{npts} - xrangle_1\right)}{Qpts}$$

Begin the calculations - The total number of points is the first power of two greater than the original number of data points - i.e., Qpts.

$j := 1 .. Qpts$

$xr2angle_j := xrangle_1 + step \cdot (j - 1)$

$\overrightarrow{xr2count := interp(vs, xrangle, xrcount, xr2angle)}$

Create an output array of the appropriate size and write this array to the file associated with "foutname."

$j := 1 .. Qpts$

$xr2spline_{j,3} := xr2count_j$

$xr2spline_{j,2} := xr2angle_j$

$WRITEPRN(f1) := xr2spline_0$

$i := 1 .. npts$
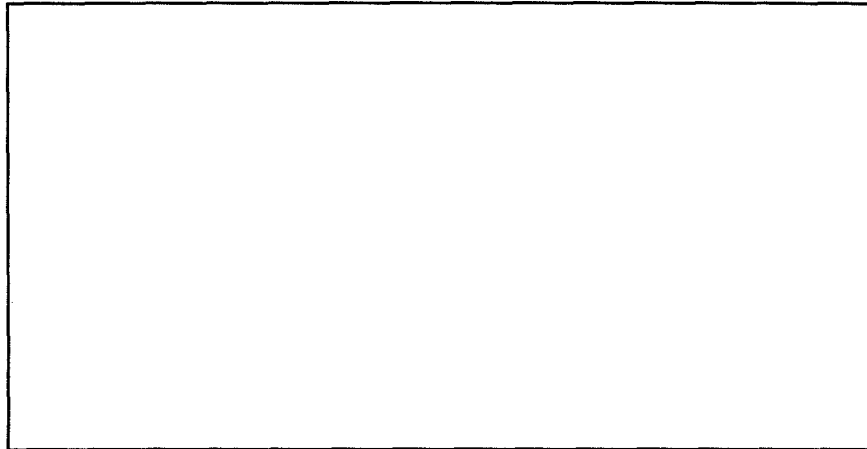


$$xr2angle_j , xrangle_i$$

Now that we have calculated a splined interpolation for the stripped data, we have "Qpts" data points, where "Qpts" is a power of two. This was done to allow the use of the fft() and ifft() functions in MCAD, as opposed to the cfft() and icfft() functions which do not require a power of two but are much slower.

## Calculation of the Frequency Spectrum of an Instrument Function-

This part of the document takes the Fourier Transform of an x-ray diffraction spectrum and calculates its frequency dependence. In particular, this allows the calculation of the coefficients of the Fourier series for the instrument function, which in turn allows it to be deconvolved from the experimentally measured profile, thus leaving only the line profile of the material

$\lambda := 1.540562$

$xrstrip := xr2spline$

$xrangle := xrstrip^{<2>}$ $\qquad$ $xrcount := xrstrip^{<3>}$

Define the scattering vector, **q**.

$$q := \overrightarrow{\left[ 2 \cdot \frac{\left( \sin\left( \frac{xr2angle}{2} \cdot \frac{\pi}{180} \right) \right)}{\lambda} \right]}$$

Take the Fast Fourier Transform of the data.

$T := fft(xrcount)$

$i := 1 .. rows(T)$

The frequency is defined as the inverse of the q-vector step size. Note that this is an approximation that is valid only if sin(deltatheta)~deltatheta, which is fine for small deltatheta. In other words, this is okay as long as your peaks are not too wide.

$$f_i := \frac{i}{q_i}$$

$$Tmag_i := \frac{T_i \cdot \exp\left[ \pi \cdot (i-1) \cdot \sqrt{-1} \cdot \frac{Qpts-1}{Qpts} \right]}{T_1}$$

$$\max(f) = \qquad f_1 =$$



$\mathrm{Tmag_i}$
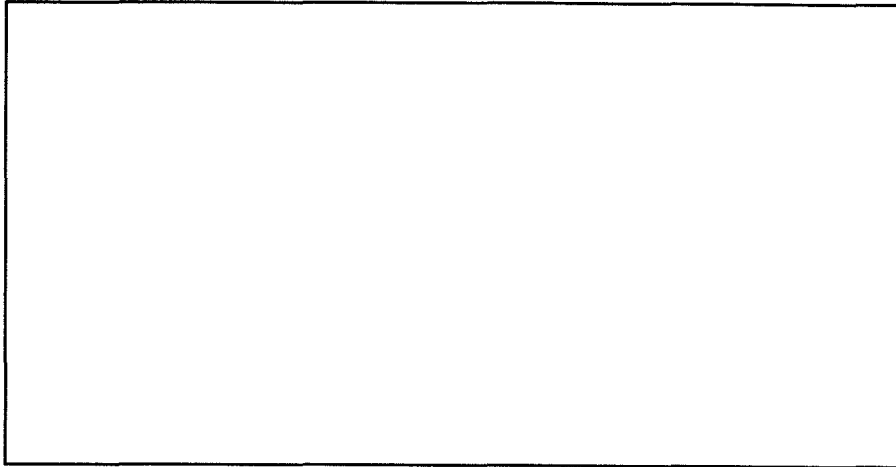
$$f_i$$

Write the transformed spectrum to a file.

$$\mathrm{xrFT}_{i,1} := f_i$$

$$\mathrm{xrFT}_{i,2} := \mathrm{Tmag_i}$$

$$\mathrm{WRITEPRN}(f2) := \mathrm{xrFT}$$

$$\mathrm{FTxr}_1 := \mathrm{xrFT}_{1,1}$$
$$j := 2..10$$

$$\mathrm{FTxr}_j := \mathrm{xrFT}_{j-1,2}$$

$$\mathrm{APPENDPRN}(f3) := \mathrm{FTxr}^T$$

$$\mathrm{FTxr}^T =$$

# Calculation of Crystallite Size and Strain from X-ray Peak Broadening

reference: Klug and Alexander, *X-ray Diffraction Procedures,* chp. 9, pp. 661-665.
Written by David S. Lee, April 1991.
Input peak positions and peak widths in degrees two theta.
You must know the instrument's profile for the angles to be analyzed.
Program has been written to use FWHM rather than integral breadths.
Accuracy is about 10%.

$\text{ORIGIN} \equiv 1$

$N := 3$

$\lambda := 1.540598$

$i := 1 .. N$

$\theta 2_i :=$

| 32.8 |
| 40.3 |
| 58.4 |

$\delta\theta 2_i :=$

| .375 |
| .375 |
| .375 |

$\text{inst}_i :=$

| 0.08 |
| 0.08 |
| 0.10 |

$$\text{FWHM}_i := \sqrt{\left(\delta\theta 2_i\right)^2 - \left(\text{inst}_i\right)^2}$$

$\text{inst} =$                    $\text{FWHM} =$

Convert units to radians and switch to s-space (related to k-space by a constant).

$$\theta_i := \frac{\pi}{360} \cdot \theta 2_i \qquad\qquad Btot_i := \frac{\pi}{180} \cdot FWHM_i$$

$$s_i := 2 \cdot \frac{\sin(\theta_i)}{\lambda} \qquad\qquad \delta s_i := \frac{\cos(\theta_i)}{\lambda} \cdot Btot_i$$

$$s = \qquad\qquad \delta s =$$



$\delta s_i$

$s_i$
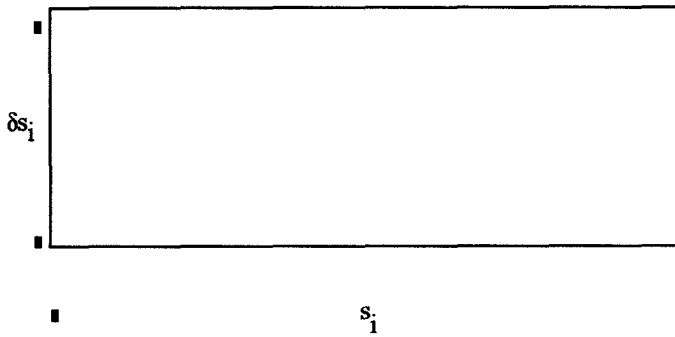
*Cauchy size broadening w/ Cauchy strain broadening:*

$$y_i := \delta s_i$$

$$j := 1 .. N$$

$$A_{1,1} := \sum_j \left(s_j\right)^2 \qquad\qquad A_{1,2} := \sum_j \left(s_j\right)$$

$$A_{2,1} := A_{1,2} \qquad\qquad A_{2,2} := N$$

$$B_1 := \sum_j s_j \cdot y_j \qquad\qquad B_2 := \sum_j y_j$$

$$C := A^{-1} \cdot B \qquad\qquad C =$$

$$\text{strainmax} := \frac{C_1}{2} \qquad\qquad L := \frac{1}{C_2}$$

$$f(x) := C_1 \cdot x + C_2$$

$$f\left(s_i\right)$$

$$\delta s_i$$

$$s_i$$
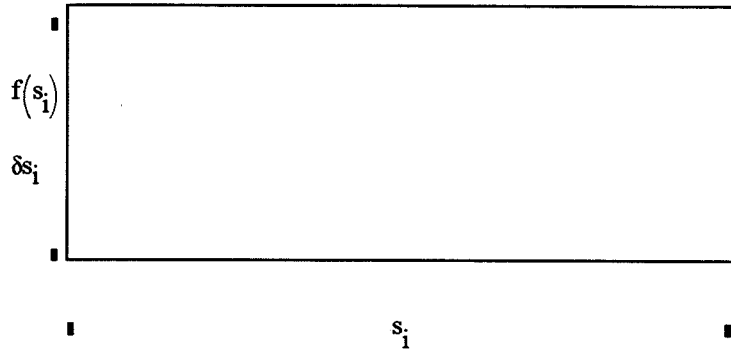
$$SS := \left(\frac{1}{N-2}\right) \cdot \sum_j \left[y_j - \left(C_1 \cdot s_j\right) - C_2\right]^2$$

$$SDc1 := SS \cdot \left(A^{-1}\right)_{1,1} \qquad SDc2 := SS \cdot \left(A^{-1}\right)_{2,2}$$

$$errorstrain := \frac{\sqrt{SDc1}}{2} \qquad errorL := L^2 \cdot \sqrt{SDc2}$$

$$CCL := L \qquad CCerrorL := errorL$$

$$CCstrain := strainmax \qquad CCerrorstrain := errorstrain$$

$$L = \qquad errorL =$$

$$strainmax = \qquad errorstrain =$$

*Gaussian size broadening w/ Gaussian strain broadening:*

$$y_i := \left(\delta s_i\right)^2$$

$$j := 1 .. N$$

$$A_{1,1} := \sum_j \left(s_j\right)^4 \qquad\qquad A_{1,2} := \sum_j \left(s_j\right)^2$$

$$A_{2,1} := A_{1,2} \qquad\qquad A_{2,2} := N$$

$$B_1 := \sum_j \left(s_j\right)^2 \cdot y_j \qquad\qquad B_2 := \sum_j y_j$$

$$C := A^{-1} \cdot B \qquad\qquad C =$$

$$\text{strainmax} := \frac{\sqrt{C_1}}{2} \qquad\qquad L := \frac{1}{\sqrt{C_2}}$$

$$f(x) := C_1 \cdot x + C_2$$

$$f\left[\left(s_i\right)^2\right]$$

$$\left(\delta s_i\right)^2$$

$$\left(s_i\right)^2$$
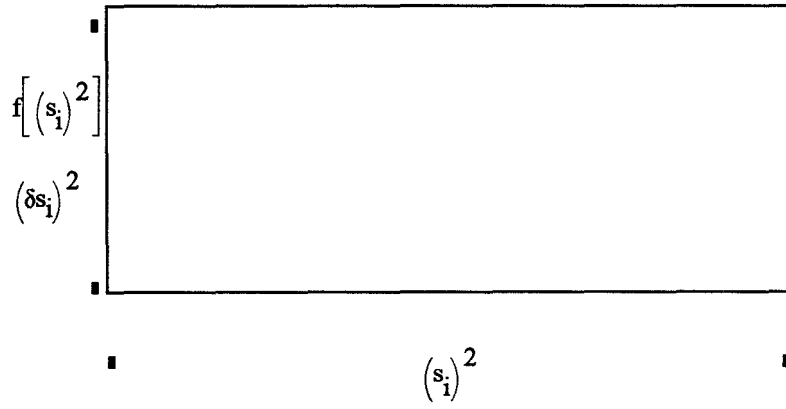
$$SS := \left(\frac{1}{N-2}\right) \cdot \sum_j \left[ y_j - \left[ C_1 \cdot (s_j)^2 \right] - C_2 \right]^2$$

$$SDc1 := SS \cdot \left(A^{-1}\right)_{1,1} \qquad SDc2 := SS \cdot \left(A^{-1}\right)_{2,2}$$

$$errorstrain := \frac{\sqrt{SDc1}}{8 \cdot strainmax} \qquad errorL := \frac{L^3}{2} \cdot \sqrt{SDc2}$$

$$GGL := L \qquad GGerrorL := errorL$$

$$GGstrain := strainmax \qquad GGerrorstrain := errorstrain$$

$$L = \qquad errorL =$$

$$strainmax = \qquad errorstrain =$$

*Cauchy size broadening w/ Gaussian strain broadening:*

$$y_i := \left(\frac{\delta s_i}{s_i}\right)^2$$

$$j := 1 .. N$$

$$A_{1,1} := \sum_j \left[\frac{\delta s_j}{\left(s_j\right)^2}\right]^2 \qquad\qquad A_{1,2} := \sum_j \left[\frac{\delta s_j}{\left(s_j\right)^2}\right]$$

$$A_{2,1} := A_{1,2} \qquad\qquad A_{2,2} := N$$

$$B_1 := \sum_j \frac{\delta s_j}{\left(s_j\right)^2} \cdot y_j \qquad\qquad B_2 := \sum_j y_j$$
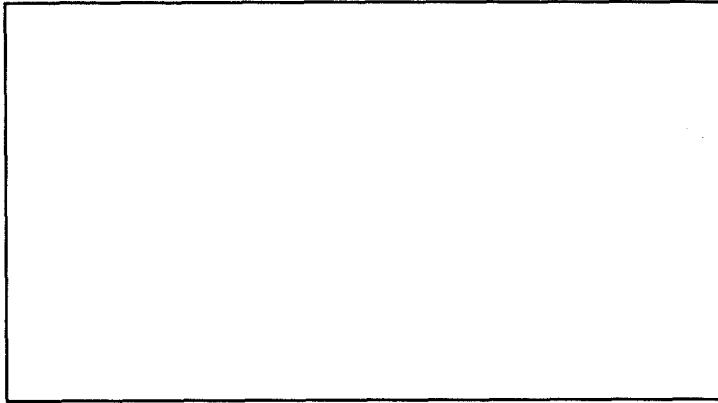
$$C := A^{-1} \cdot B \qquad\qquad C =$$

$$\text{strainmax} := \frac{\sqrt{C_2}}{2} \qquad\qquad L := \frac{1}{C_1}$$

$$f(x) := C_1 \cdot x + C_2$$

$$f\left[\frac{\delta s_i}{\left(s_i\right)^2}\right]$$

$$\left(\frac{\delta s_i}{s_i}\right)^2$$

$$\frac{\delta s_i}{\left(s_i\right)^2}$$

$$SS := \left(\frac{1}{N-2}\right) \cdot \sum_j \left[ y_j - \left[ C_1 \cdot \frac{\delta s_j}{\left(s_j\right)^2} \right] - C_2 \right]^2$$

$$SDc1 := SS \cdot \left(A^{-1}\right)_{1,1} \qquad SDc2 := SS \cdot \left(A^{-1}\right)_{2,2}$$

$$errorstrain := \frac{\sqrt{SDc1}}{2} \cdot L^2 \qquad errorL := \frac{\sqrt{SDc2}}{8 \cdot strainmax}$$

$$CGL := L \qquad CGerrorL := errorL$$

$$CGstrain := strainmax \qquad CGerrorstrain := errorstrain$$

$$L = \qquad errorL =$$

$$strainmax = \qquad errorstrain =$$

Choose whichever combination fits the data the best.

# Appendix B:        Techniques For Measuring Superconductivity

The superconducting properties of the materials were checked by either a standard four-point AC resistivity probe or a Meissner coil AC susceptibility measurement or both. These measurements made use of an RMC Cryosystems closed-cycle helium refrigerator which is capable of reaching temperatures below 10K. The heat pumping characteristics of the refrigerator are ¼W at 10K and 2½W at 20K. The coldhead, which was designed here and later marketed by RMC Cryosystems, features a sample chamber that is cooled via conduction through two OFHC copper wicks that are attached from near the bottom and middle of the sample chamber to the first and second stages of the expander. The expander itself sits in a separate high vacuum chamber. This design allows the use of an exchange gas in the sample chamber and obviates the need for careful thermal anchoring of lead wires down the length of the probe (the exchange gas develops a gradient in temperature down the length of the chamber: near room temperature at the top of the chamber and about 10K by the connection to the second stage of the expander). This also helps to ensure temperature uniformity in the measurement area. The top of the sample chamber has a "loadlock" area to allow for the pumping out of air after insertion of the sample probe. A TMP50 Leybold-Heraeus turbomolecular pump evacuates the sample chamber and the coldhead chamber. Base pressures of the system are in the $10^{-6}$ torr range.

Temperature is controlled by a RMC Cryosystems Model 4000 three-term controller and Lakeshore DT470 Si diodes which are situated on the tip of the second stage of the expander and adjacent to the sample on the same phenol (G10) sample holder. Because the measurements are typically done in an atmosphere of Helium exchange gas,. there can be no difference between the measured temperature and the actual temperature of the sample. Heating is accomplished by passing a DC current through a non-inductively

wound heater coil wrapped around the second stage of the expander in the coldhead chamber, which in turn heats the sample chamber by conduction through the copper wick.

The AC resistivity measurements are usually done at 91Hz (the choice of frequency was made to ensure that no line harmonics would make it past the lock-in amplifier's high-Q bandpass filter). Four 50$\Omega$ microcoaxial cables run the length of the sample probe to four Copper–4%Beryllium spring clips which contact the sample either directly by pressure or through small dots of silver paint. The signals are generated by a Fordham model AG-260 audio generator and run through a 1:1 bootstrapping follower to electronically isolate the input signal from the measurement apparatus. A LM110 low-noise, high slew rate precision op amp is used in the voltage follower circuit. Bootstrapping was necessary because the bias path can compromise the high input impedance one would normally get with an op amp, particularly with AC-coupled inputs, where a resistor to ground is mandatory. The circuit is shown in figure B.1. The 2$\mu$F capacitor makes the upper 100K$\Omega$ resistor look like a high-impedance current source to the input signals. The low frequency rolloff for this circuit will begin at about 20Hz, and the response will drop at 12dB per octave for frequencies somewhat below this, where both capacitors contribute to the rolloff.

The measured signal is brought out of the probe to a Stanford Research Systems Model SR 530 two channel lock-in amplifier. Temperature measurement is done with a Keithley Model 196 System DMM. The ultimate sensitivity of the system is noise limited to $\leq$30 nV/$\sqrt{Hz}$. The silicon diodes in the system are Lakeshore Cryogenics Model DT470 series calibrated to provide accuracy to 0.02K.

The Meissner coil susceptibility measurement uses two identical counterwound secondary coils situated within an outer primary coil which is driven by an Adcom GFA535 audio amplifier at a maximum field of about 0.75T in the center of the coil. As the sample undergoes a superconducting transition, the Meissner effect expels all flux lines from within the interior of the sample, thus altering the inductance of the coil in

which it sits; the two secondary coils then become unbalanced. This imbalance is picked up by the lock-in amplifier.

The susceptibility measurements were useful for checking the existence of a transition but were not capable of quantitative measurements (for instance, of superconducting volume fraction). Probe geometry and fringing field effects complicated any attempts to quantify the signals measured.

All connections to the coldhead and on down to the sample area are impedance matched. All instruments are connected via standard IEEE-488 connections to an IBM AT-compatible computer. Programs to automate the entire process after sample insertion were written in Microsoft QuickBasic™. An extensive help manual and user's guide is located next to the equipment. Furthermore, the programs are currently being updated to run under Microsoft Visual Basic for DOS™, a menu-driven object-oriented programming language that will make the equipment substantially easier to use. Code written for QuickBasic™ is (alleged) to be entirely compatible with the Visual Basic for DOS™ compiler. The conversion to the new programming language will also make on-line, context-sensitive help available to the user.

Liquid helium dewars were also used to measure resistivity of the samples on occasion and prior to the delivery of the coldhead system. These glass dewars were double vacuum-jacketed dewars which were pre-cooled with liquid nitrogen before the transfer of helium was begun. Four-point resistivity probes were built for insertion into these dewars. Temperature was measured either by gold-iron thermocouples (which have an NBS-defined 12th order polynomial fit at low temperatures for interpolation) or GaAs red LED diodes that had been calibrated against either a DT-470 series Si diode or a Ge diode. These were industry standard (approximately 5¢ apiece) LED's purchased at Radio Shack. The plastic was first clipped away as much as possible then dissolved with an organic solvent to expose the GaAs chip. These diodes had a reproducibility better than 0.05K. A modified version of the resistivity program written for the closed-cycle helium

refrigerator was later written to control the measurement process for the liquid helium dewar.

In general, the characterization of superconducting properties of the materials were done as the inserted sample probe was cooling down to cold temperatures. This method was chosen to shorten the time necessary to obtain data about the superconducting properties of the material. However, the careful, quantitative measurements of resistivity were always double-checked by first inserting the sample and measuring properties as the sample cooled to the cryostat's internal temperature (about 15K for the closed-cycle He refrigerator and 4.2K for the liquid He dewar) and then repeating the measurements on heating with the non-inductively wound heating element back up to room temperature. This allowed the use of three-term temperature control (proportional, integral and derivative control) and thus minimized overshoot and oscillation effects. The whole temperature profile can be programmed and executed by the computer.

Schematic drawings of the closed-cycle helium refrigerator, the resistivity probe and the Meissner coil probe are shown in figures B.2 through B.4.
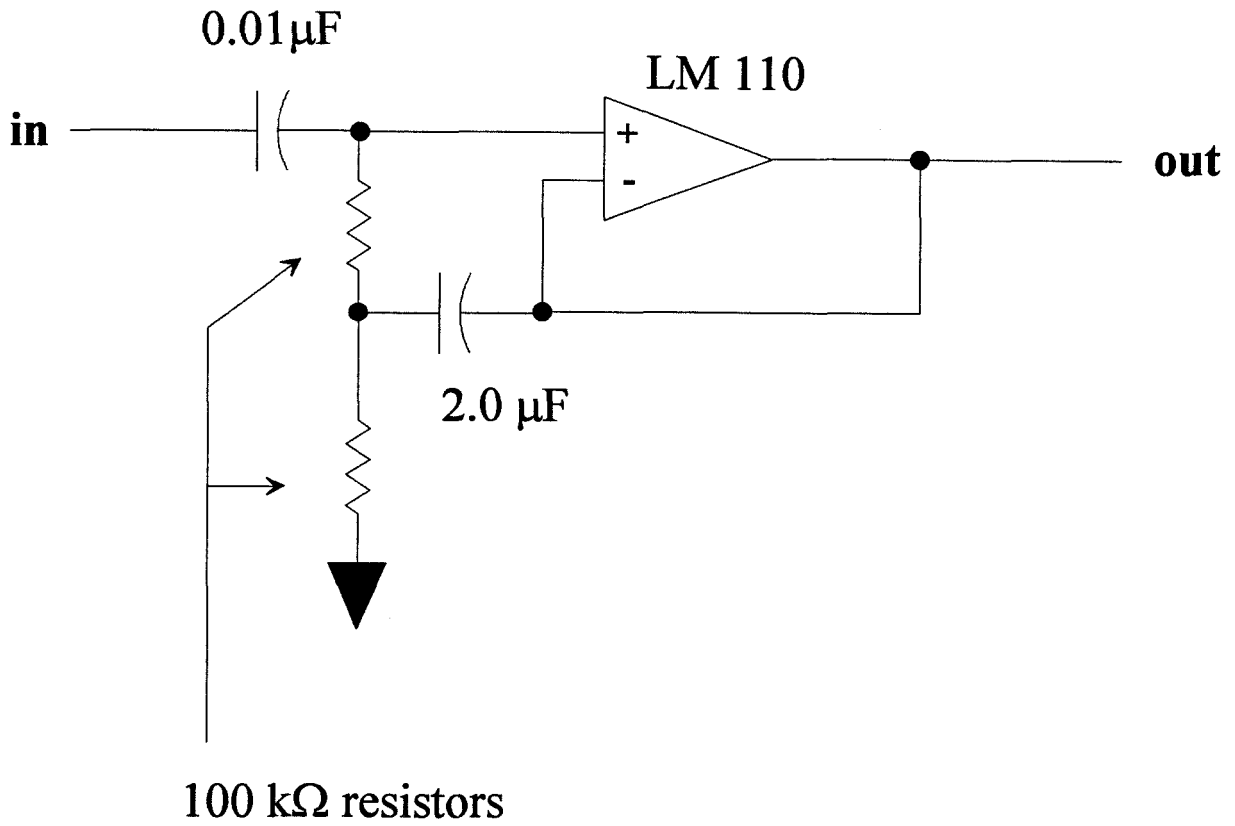
Figure B.1– Bootstrapping voltage-follower circuit used in the AC resistivity measurements.
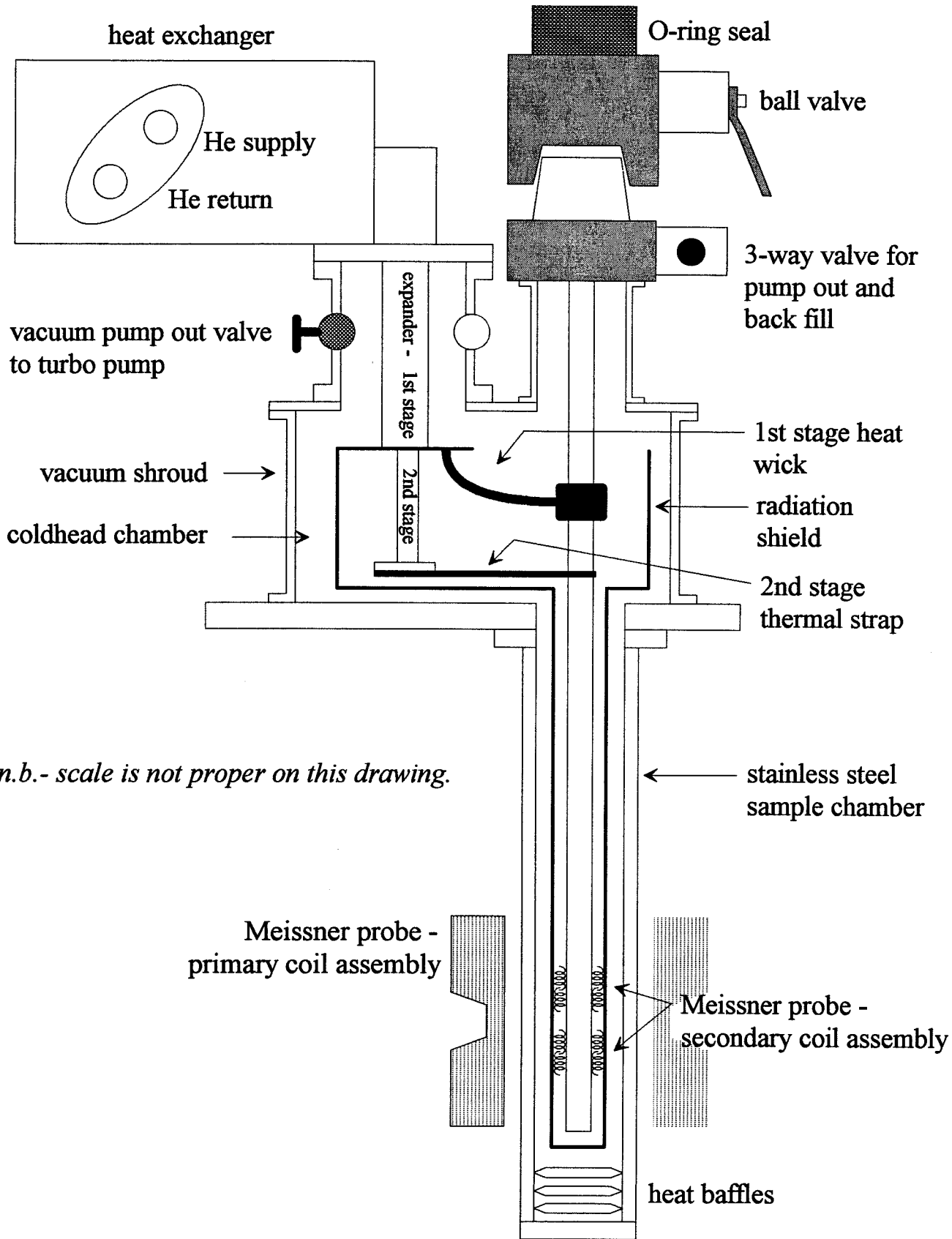
heat exchanger

He supply

He return

O-ring seal

ball valve

3-way valve for
pump out and
back fill

vacuum pump out valve
to turbo pump

expander - 1st stage

2nd stage

vacuum shroud →

coldhead chamber →

1st stage heat
wick

radiation
shield

2nd stage
thermal strap

n.b.- scale is not proper on this drawing.

stainless steel
sample chamber

Meissner probe -
primary coil assembly

Meissner probe -
secondary coil assembly

heat baffles

Figure B.2– Schematic of the closed-cycle Helium refrigerator.

10-pin Burnaby Mil-Spec 3126 connector

4 BNC connections for current and voltage leads

*n.b.- drawing is not to scale.*

Lakeshore DT470 Si diode

current and voltage leads (two sets)
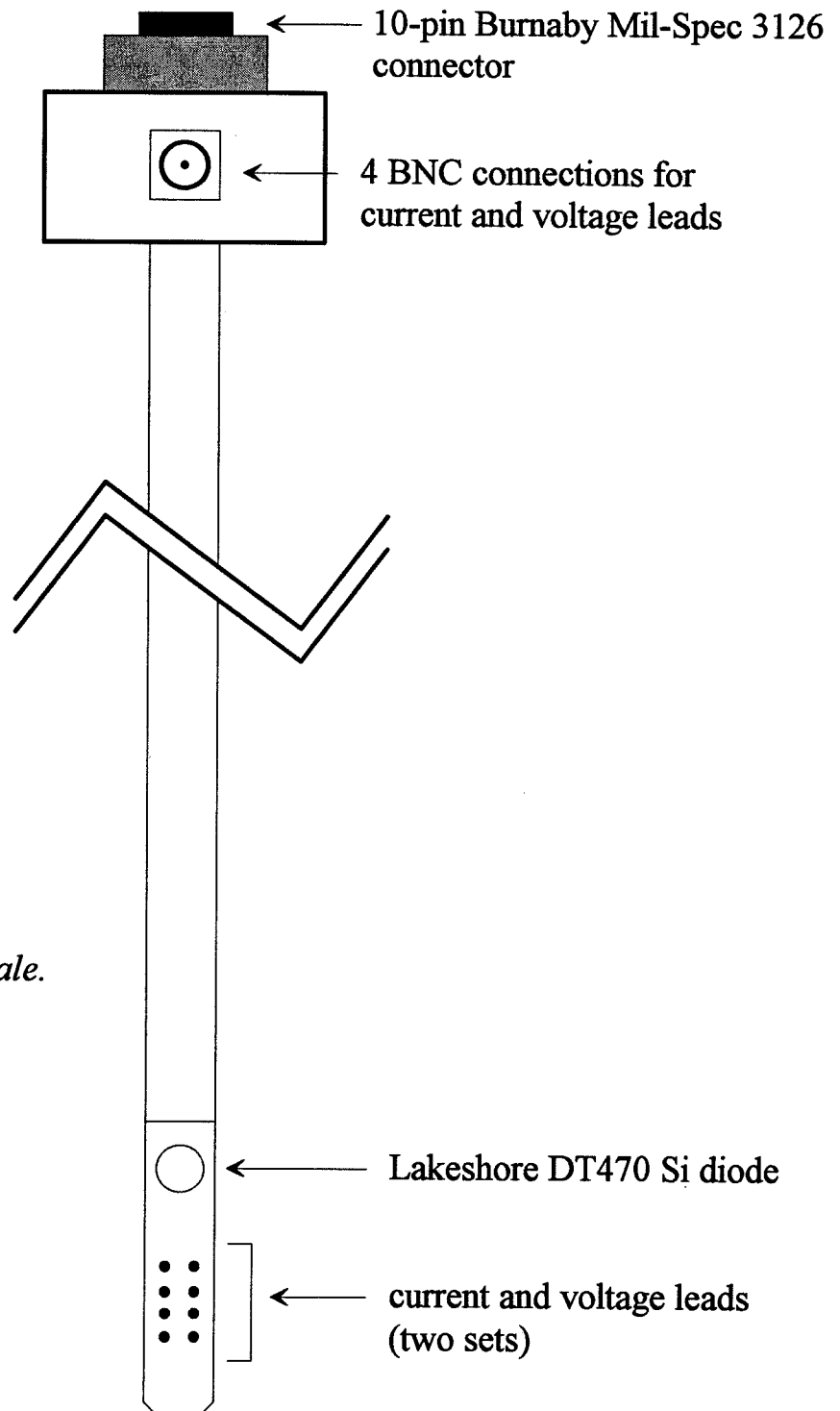
Figure B.3– Schematic of the resistivity probe.

10-pin Burnaby Mil-Spec 3126 connector

*n.b.- drawing is not to scale.*

Lakeshore DT470 Si diode

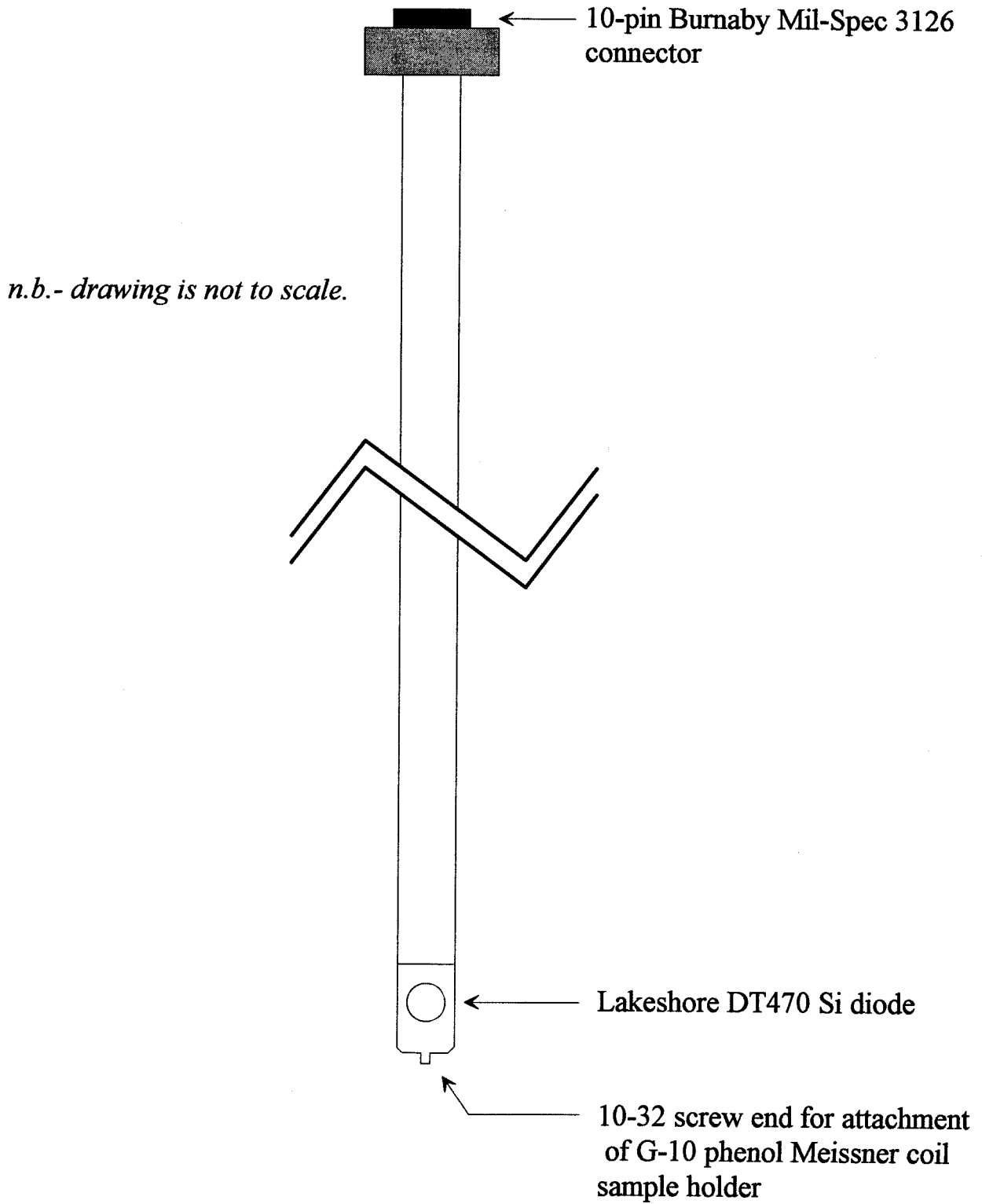10-32 screw end for attachment of G-10 phenol Meissner coil sample holder

Figure B.4– Schematic of the susceptibility probe.